FORSCHUNGSZENTRUM JÜLICH GmbH

Institut für Kernphysik

High resolution K X-Ray Spectra of Heavy Elements Excited during the Bombardment with Energetic Ions

D.F. Anagnostopoulos

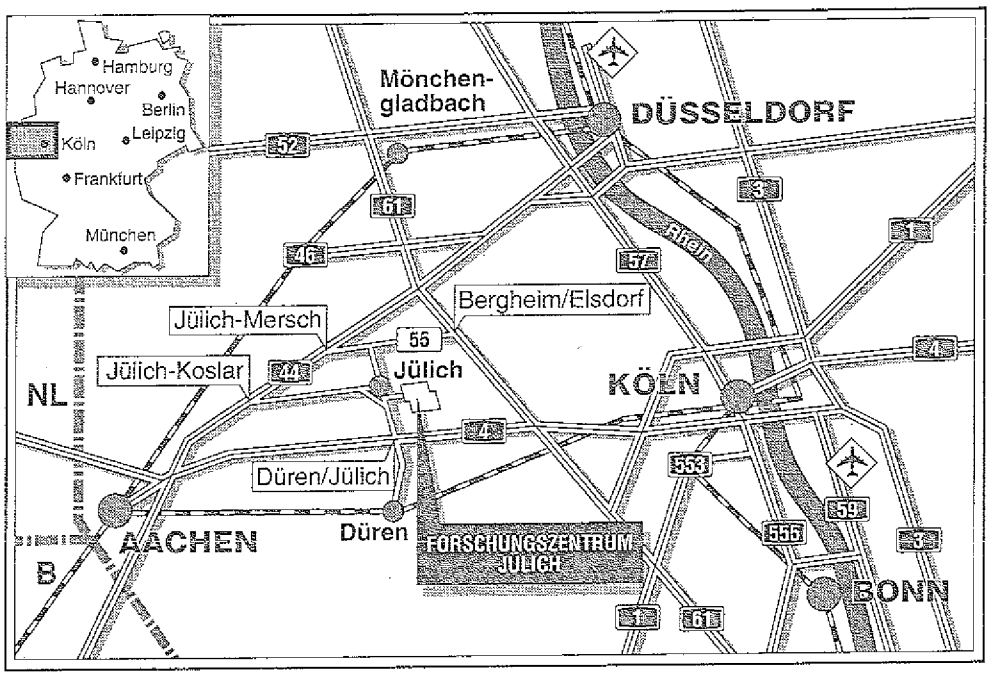

Berichte des Forschungszentrums Jülich ; 2667
ISSN 0366-0885
Institut für Kernphysik Jül-2667

Zu beziehen durch: Forschungszentrum Jülich GmbH · Zentralbibliothek
Postfach 1913 · D-5170 Jülich · Bundesrepublik Deutschland
Telefon: 02461/61-6102 · Telefax: 02461/61-6103 · Telex: 833556-70 kfa d

High resolution K X-Ray Spectra of Heavy Elements Excited during the Bombardment with Energetic Ions

D.F. Anagnostopoulos

Contents

List of Figures

List of Tables

1. Introduction

X-ray emission was observed in 1895 by Röntgen and was so named because of its mysterious nature at that time. The X-rays have now long been identified as electromagnetic radiation of atomic origin but there are still open questions in connection with a detailed understanding of their spectra.

The study of **atomic inner-shell ionization** dates back to that time when the mysterious radiation has been produced by high-energy electrons. In the last two decades the use of particle accelerators in atomic collision studies has yielded a great deal of experimental information not previously predicted and so a vast field of interesting problems came up.

Basic studies of the ionization processes supply important information for the development of more reliable theoretical models to describe the fundamental processes of interaction of ions with matter.

As for applied physics the ionization processes are important in many fields, like for trace element analysis, ion implantation, astrophysics, solid state physics, atmospheric physics, X-ray lasers, and nuclear physics.

One of the most challenging problems for the interpretation of the X-ray emission spectra is that associated with satellite processes. The X-ray satellites are transitions in atoms with multiply ionized inner shells. The highly excited states can be created either directly in the collision process or after Auger, Coster-Kronig transitions, shake-up and shake-off processes. A major problem in the analysis of the emission spectra is the difficulty in identification of these satellite lines and the explanation of the involved processes.

In the present work, we investigate with high resolution the K X-ray satellite structure, of lanthanum, tantalum and uranium, during the bombardment with 403 and 350 MeV nitrogen, and 500 MeV neon beams, respectively.

During the ion-atom collision the ejection of a K electron may be accompanied to a high degree by simultaneous creation of vacancies in L,M and outer shells. The main processes which are responsible for the creation of the inner-shell vacancies are the direct ionization, in which bound electrons of the target atom are ejected into the continuum, and the capture of target electrons into the bound states of the projectile.

A **high resolution measurement** of such K X- ray satellite spectra permits a crucial test of atomic structure models and provides information about the mechanisms and the properties of the ionization processes.

One of the most direct information supplied by high resolution spectroscopy concerns the transition energies of the emitted X-rays. The comparison of experimental and theoretical transition energies in (multi)ionized atoms is quite

interesting. The *ab initio* evaluation of the X-ray transition energies is one of the most attractive problems of theoretical atomic physics, because it is a many-electron problem which has to be solved in the framework of relativistic quantum mechanics.

Concerning the ion-atom interaction, from the analysis of the intensity distribution of K X-ray satellites, information is exctracted mainly for the L (sub)shell ionization probabilities for very small impact parameters, relative to the L scale.

In general, the relative intensities of X- ray satellites in a high resolution spectrum do not directly reflect the primary vacancy production. The conversion of measured to initial distribution, however, requires a detailed knowledge of the transition lifetimes for multiply-ionized atoms, the degree of multiple ionization in the M and higher shells, the rearrangement of L-shell vacancies due to Coster-Kronig transitions in multiply-ionized states formed in heavy-ion collisions, the L-shell vacancy refilling from higher shells prior to decay of the K vacancy, the fluorescence yields for the individual configurations and the multiplet splittings which can be as large as the splittings of other configurations. The correction for all these processes requires detailed and lengthly analysis.

The above mentioned corrections can be more easily estimated and their uncertainties can be reduced by using **heavy Z target elements.**

The study of the atomic **L - shell** of heavy elements provides a suitable environment for a detailed test of theories to describe the inner-shell ionization induced by collisions, because it involves the minimum number of subshells with different binding energies, angular momenta, spatial symmetries and degree of relativistic electron motion.

Impact parameter measurements (differential measurements) are important for our general understanding of inner-shell ionization since they provide a more detailed test of the theoretical descriptions than is obtained from measurements of the total cross section.

In the case of **asymmetric** ($Z_{proj} \ll Z_{targ}$) and **'fast' collisions** (projectile's velocity in the order of the L target electrons) the influence of the projectile motion on L target electrons is weak, due to the small strength of the projectile-target interaction and due to the short interaction times. The ionization mainly of L and M electrons is due to processes acting direct to the target atomic states. So asymmetric and fast collisions can be used as tool for studying different atomic potential and wave function models.

2. Inner-shell ionization mechanisms

When a fast ion passes through a target atom, the Coulomb interaction causes a production of inner-shell vacancies with high probability. This process is mainly attributed to three distinct mechanisms :

- I) The direct Coulomb interaction between the projectile and the target atom electrons. In this process the transient Coulomb field of the passing projectile causes a perturbation that leads to a promotion of the target electrons.

- II) The quasimolecular excitations. When the transition time of the projectile is large compared to the electronic orbital times, electrons may be promoted to higher levels by a dynamic interaction that can be described by molecular orbitals.

- III) The electron capture of target inner-shell electrons into empty orbitals of the projectile or charge exchange.

For a convenient discussion of the mechanisms (I) and (II) we define (see [Ma75, Vol.I, p2.], [Mo78]), an asymmetry parameter (Z_1/Z_2) and an adiabaticity parameter ($n = (u_1/u_2)^2$), where Z_1 and Z_2 are the atomic numbers of projectile and target atom, respectively, u_1 denotes the initial projectile velocity and u_2 the orbital velocity of the active target electron.

With the help of these parameters the colliding systems can be divided into two regions. In Fig. 2.1 the dashed area denotes the region where the direct Coulomb mechanism is dominant ($Z_1/Z_2 \ll 1$ and/or $n \gg 1$), and corresponds to the situation where the perturbating influence of the nuclear motion on electrons is very weak due to a very small strength of the projectile-target interaction or due to a very short interaction time. In this case electron transitions are described in terms of processes acting direct on target or projectile states and are essentialy determined by the structure of the target electron wave functions.

On the other hand, the cross-hatched area in Fig. 2.1 denotes the region of the molecular-orbital excitation, ($Z_1/Z_2 \sim 1$ and $n < 1$). There the strong interaction between electrons and colliding nuclei leads to the formation of a transient diatomic complex (quasimolecule). In this case the electrons adjust their wave functions on the perturbation caused by the collision partner and essentially the electronic structure of the united atom is approached (MO model).
There are no detailed experimental results available which clarify the limits of the different regions.

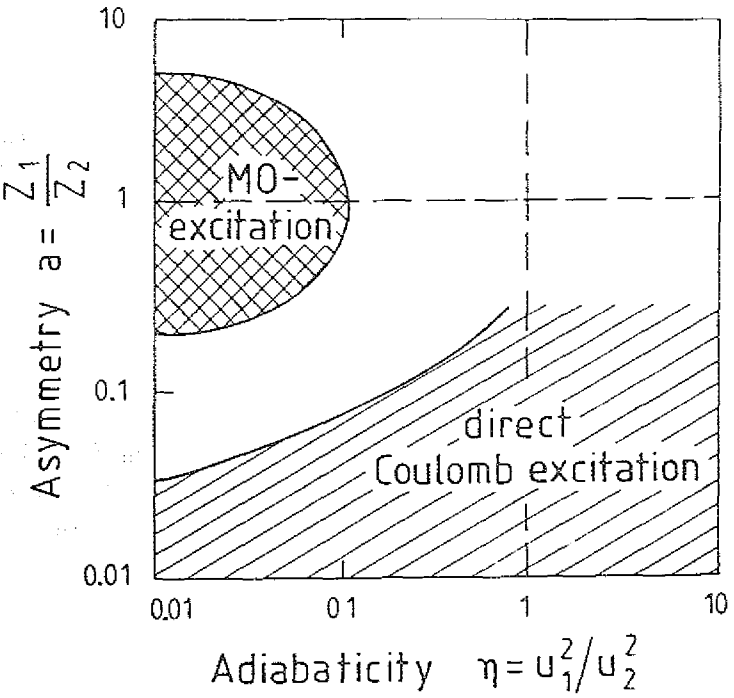

Figure 2.1: *The domains for the excitation processes, direct ionization and quasi-molecular electron-promotion (MO), as a function of the adiabaticity parameter* $n = (u_1/u_2)^2$ *and the asymmetry parameter* Z_1/Z_2 *(see [Ma75], [Mo78]).*

2.1 Direct Coulomb ionization

The theoretical description of the direct Coulomb excitation or ionization of an initially bound target electron to a higher unoccupied, bound or continuum level, is usually based on a reference frame fixed to the target atom, which interacts with the transient field of the passing projectile. Evidently, this mode of description is most appropriate for heavy targets with high nuclear charge (Z_2) causing a tight atomic binding of the electrons, and for a fast projectile with low charge (Z_1). The Coulomb interaction between the projectile and the atomic electron is then adequately treated as a time-dependent perturbation of the target atom. The perturbation theory assumes that the Coulomb interaction directly couples the initially tight bound inner-shell electron states to the unoccupied discrete and unbound continuum electron states.

For the description of the Coulomb ionization three mainly theoretical approximations are used : the Plane Wave Born Approximation (PWBA) [Me58] which is a first-order Born treatment with the incident projectiles represented mainly by a plane wave, the Binary-Encounter-Approximation (BEA) [Ga73] is based upon the classical energy transfer process wherein a projectile interacts with an inner-shell electron having a velocity distribution representative of its binding

energy, and finally the Semi-Classical Approximation (SCA) [Ba59] which is a first-order time-dependent perturbation theory with the projectile moving along classical trajectories with well-defined impact parameter.

In order to use a classical treatment for the impinging particle, one may describe its motion by a wave packet small compared with the distance of closest approach to the target nucleus. The necessary and sufficient condition for describing a well-defined path of the projectile during the scattering in the target Coulomb field is given by [Bo48] :

$$k = \frac{4\pi d}{\lambda} = \frac{2 \cdot Z_1 \cdot Z_2 \cdot e^2}{\hbar \cdot u_1} \gg 1 \tag{2.1}$$

where $2 \cdot d = 2 \cdot Z_1 \cdot Z_2 \cdot e^2/(M_1 \cdot u_1^2)$ is the distance of the closest approach in a head-on collision (radius of Coulomb barrier), u_1 is the initial velocity of the projectile, M_1 is its mass and λ the de Broglie wave length of the projectile. It must be noted that the above relation is a necessary condition for the definition of an impact parameter from the scattering angle. The semiclassical treatment of the ionization, is valid under much less restrictive conditions [An82].

For our colliding systems the classical treatment for the impinging projectile is justified, as the Eq. (1.1) is fulfilled, and moreover the SCA is used as it has a simple conceptual basis and is primary useful for impact dependent calculations.

2.1.1 Semi-Classical Approximation (SCA)

The treatment of the atomic Coulomb excitation in the SCA formulation as we have mentioned is based on first-order time-dependent perturbation theory in impact parameter form and the use of unperturbated electron wavefunctions. The Coulomb interaction between the bound inner shell electron and the bare projectile nucleus is used as the perturbating potential :

$$V_P(\vec{r}, \vec{R}) = -\frac{Z_1 \cdot e^2}{|\vec{R}(t) - \vec{r}|} \tag{2.2}$$

with $\vec{R}(t)$ denoting the time dependent position vector of the impinging particle and $\vec{r}$ the position vector of the electron (Fig. 2.2). This potential represents a small perturbation, if the charge of the naked projectile is much smaller than that of the target nucleus, i.e. $Z_1 \ll Z_2$.

Except the projectile perturbation V_P, the transition is also mediated by the recoil field V_R of the target nucleus. The perturbation due to recoil of the target atom can be neglected in the cases where the projectile's path can be approximated as a straight trajectory.

In first order time-dependent perturbation theory, the single electron ionization probability it p(b) as a function of the impact parameter b, for excitation from an unperturbed atomic state $|i>$ to an excited final state $|f>$ due to the time-dependent Coulomb perturbation interaction, is given by:

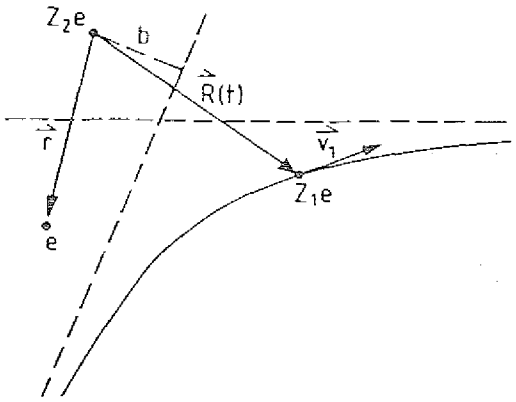

Figure 2.2: *Classical picture of the impact process, showing the projectile* Z_1 *with impact parameter* b *passing near target nucleus* Z_2 *on a Kepler orbit. The projectile time dependent position is defined by* $\vec{R}(t)$. *The atomic electron is at position* $\vec{r}$.

$$p(b) = \int_0^\infty dE_f \sum_f |a_{fi}|^2 \tag{2.3}$$

where

$$a_{fi} = -\imath \int_{-\infty}^{\infty} dt \, \exp[\imath(E_f - E_i)t] < \Psi_f | V_P + V_R | \Psi_i > \tag{2.4}$$

with E_f and Ψ_f being the energy and the wave function of the target electron continuum state $|f>$ and E_i, Ψ_i is the energy and the wave function of the initial bound state $|i>$. It must be mentioned, that in the framework of the independent – particle approximation, the one–electron equations can be used as a starting point, instead of considering totally antisymmetriced wave functions for the states of the many–electron atom [Re73].

The single electron ionization cross section σ is given as the integral over the impact parameter dependent electron ionization probability $p(b)$:

$$\sigma = 2\pi \int_0^\infty p(b)\, b\, db \tag{2.5}$$

Straight line trajectory version of SCA

In the simplest SCA model the projectile is described as moving along a straight–line trajectory with constant velocity u_1. This approximation is justified if there are no contributions to the ionization with small impact parameters , so that no elastic Rutherford scattering from the nucleus occurs.

This condition requires the distance of the closest approach in a head–on collision to be small compared to the radius of an inner–shell orbit. It is equivalent

to the condition $\Delta E \ll E_1$, where ΔE is the energy which is transferred from the projectile's energy E_1 to the target atom. In the case that the atom is ionized, $\Delta E = E_B + E_f$, where E_B is the binding energy of the Coulomb ejected electron in its initial state and E_f the kinetic energy of the ejected electron. This condition is obviously satisfied if, as in our case, the projectile energy is much greater than the relevant atomic ionization potential.

In the case of a straight−line trajectory the SCA theory expressed in terms of special variables (X_A and B_A), yields approximate scaling relations for different target atoms and projectiles [Ha75].

In the case of a proton projectile, with kinetic energy E_1 the following results have been obtained for the ionization probability $p(b)$ and the total Coulomb ionization cross section [Ha75]:
For a given subshell A, characterized by hydrogenic quantum numbers n_A, l_A the ionization probability $p(b)$ can be expressed with the help of a generalized ionization probability function $D_{n_A,l_A}(X_A, B_A)$ as

$$p(b) = \frac{2j_A + 1}{2l_A + 1} \cdot \frac{1}{Z_A^2 \cdot \theta_A} D_{n_A,l_A}(X_A, B_A) \tag{2.6}$$

In this formula Z_A is the screened atomic number of the target atom with nuclear charge Z_2 and screening parameter Z_A^S. Thus

$$Z_A = Z_2 - Z_A^S \tag{2.7}$$

The screening parameter Z_A^S is equal to 0.3 for the case that the ejected electron belongs to the K shell, 4.15 for L shell electrons, 11.25 for M_I, M_{II}, M_{III} subshells electrons, and 21.15 for M_{IV} and M_V [see Ha75]. θ_A is the ratio of experimental and theoretical hydrogenic binding energies :

$$\theta_A = \frac{E_B(A) \cdot n_A^2}{13.6\, Z_A^2} \tag{2.8}$$

In Eq.(2.8), the target electron binding energy $E_B(A)$ is given in eV units. The factor $(2j_A + 1)/(2l_A + 1)$in Eq. (2.6) is a simple statistical factor. The arguments X_A and B_A, of the generalized ionization probability function $D_{n_A,l_A}(X_A, B_A)$ in Eq. (2.6), have been chosen as the dimensionless quantities

$$X_A = \frac{\theta_A \cdot Z_A}{n_A \cdot \sqrt{E_1}} \tag{2.9}$$

and

$$B_A = b \frac{Z_A}{n_A \cdot a_0} \tag{2.10}$$

with a_0 denoting the Bohr radius, $a_0 = 5.29 \cdot 10^{-11}$m, and E_1 in MeV.
Using Eq. (2.5) for the total Coulomb ionization cross section and inserting Eq.

(2.6) for P(b), we obtain for the total cross section,

$$\sigma_A = \frac{2j_A+1}{2l_A+1}\frac{1}{Z_A^4\cdot\theta_A}F_{n_A,l_A}(X_A) \tag{2.11}$$

where

$$F_{n_A,l_A}(X_A) = 2\pi a_0^2 n_A^2 \int B_A\, dB_A\, D_{n_A,l_A}(X_A, B_A) \tag{2.12}$$

The values of the generalized ionization probability function $D_{n_A,l_A}(X_A, B_A)$ and the cross section functions $F_{n_A,l_A}(X_A)$ are listed in the paper of J.M.Hansteen at al. [Ha75].

In the case of heavier projectiles than proton, with charge $Z_1 \cdot e$, due to the formulation of the first order perturbation theories, the scaling law for the Coulomb ionization probabilities, from protons to other bare projectiles with charge Z_1 and the same velocity u_1, is given by:

$$p(b, Z_1, u_1) = Z_1^2 \cdot p(b, 1, u_1) \tag{2.13}$$

As this formula has been derived using first-order perturbation theory an extension to high values of Z_1 requires special care[Be84]. In the next chapter corrections to the first order theory are discussed.

2.1.2 Coupled-channels collision theory

First order theories yield good agreement for the K- shell ionization probabilities [Mo78 p. 221 and references thererin], but large deviations have been observed for L shell electrons [De86]. This behaviour can be understood as the transition matrix elements in the higher order terms of the Borns series between the initial and intermediate states yield small value because of the K shell it is rather isolated from the higher shells. In the case of the L shell, however, we are dealing with three subshells with wave functions close to each other both in space and energy, and the transition matrix elements between them can have large values.

The subshell coupling mechanism is described in such a way that the electron is excited into an unoccupied final state from a 'mixed' L state rather than from a 'pure' atomic state. The mixed state evolves in time from an initial L substate as a result of dynamical couplings with the other L substates [Sa90]. The time evolution is governed by the following eight coupled equations (in atomic units):

$$\frac{da_{n_L}}{dt} \approx -i\sum_{n'_L} V_{n_L n'_L} a_{n'_L} \tag{2.14}$$

with the initial condition

$$a_{n_L}(t=-\infty) = \delta_{n_L i} \tag{2.15}$$

The excitation from the mixed state is described by

$$\frac{da_f^{(c)}}{dt} = -\imath \sum_{n_L} V_{fn_L} a_{n_L} \tag{2.16}$$

The superscript 'c' in $a_f^{(c)}$ indicates that this amplitude is obtained solving the coupled Eq. (2.14). In Eq. (2.14-16) n_L represents a set of quantum numbers l,j, and m_j of the L substates. The matrix elements $V_{mk}(t)$ for the projectile and target−electron interaction are defined as :

$$\begin{aligned} V_{mk}(t) &= \Upsilon_{mk}(t)\, \exp(\imath\, \omega_{mk}\, t) \\ \Upsilon_{mk}(t) &= \int d\vec{r}\ \Psi_m^*(\vec{r})\, \frac{-Z_1}{\mid \vec{R}(t,b) - \vec{r}\mid}\, \Psi_k(\vec{r}) \\ \omega_{mk} &= E_m - E_k \end{aligned} \tag{2.17}$$

where Z_1 is the atomic number of the projectile, $\vec{R}$ is the internuclear vector, and $\Psi_j(\vec{r})$ and E_j are the one−electron energy eigenstates and eigenvalues of the unperturbated target atom.

In the first−order approximation it is assumed that the initial state remains unperturbated. This means that the L substate occupation amplitudes in Eq. (2.16) can be well approximated by $a_{n_L}(t) = \delta_{n_L i}$. The substitution leads to the well known first−order expression

$$a_f^{(1)}(+\infty) = -\imath \int_0^{\infty} dt\, V_{fi}(t) \tag{2.18}$$

Now we solve these truncated equations for a_f (Eq.2.16) to second order by solving the coupled equations (Eq.2.14) to first order in the following way. As a zeroth order solution we assume that

$$a_{n_L}^{(0)} = 0, \quad if \quad n_L \neq i \tag{2.19}$$

Inserting these amplitudes into the right hand side of Eq. (2.14) we get equations for the first order amplitudes

$$\frac{da_{n_L}^{(1)}}{dt} = -\imath\, V_{n_L i}\, a_i^{(1)} \tag{2.20}$$

$$\frac{da_i^{(1)}}{dt} = -\imath\, V_{ii}\, a_i^{(1)} \tag{2.21}$$

From Eq. (2.21) we get the solution for the initial state amplitude

$$a_i^{(1)}(t) = \exp\Big(-\imath \int_{-\infty}^{t} dt' V_{ii}\Big) \tag{2.22}$$

Inserting Eq. (2.22) into Eq. (2.20) the following first order solutions are obtained for the L-substate amplitudes

$$a_{n_L}^{(1)}(t) = -\imath \int_{-\infty}^{t} dt' \, V_{n_L i} \exp\Big(-\imath \int_{-\infty}^{t'} dt'' \, V_{ii}\Big), \quad n_L \neq i \tag{2.23}$$

The solutions (2.22) and (2.23) satisfy the initial condition (2.15).
Substituting Eqs. (2.22) and (2.23) into Eq. (2.16) we arrive at the second order solution

$$\begin{aligned} a_f^{(2)}(+\infty) \;=\; & -\imath \int_{-\infty}^{+\infty} dt \Big\{ V_{fi} \, exp\Big(-\imath \int_{-\infty}^{t} dt' \, V_{ii}\Big) + \\ & \sum_{n_L(\neq i)} V_{f n_L} (-\imath) \int_{-\infty}^{t} dt' \, V_{n_L i} \times exp\Big(-\imath \int_{-\infty}^{t'} dt'' \, V_{ii}\Big) \Big\} \end{aligned} \tag{2.24}$$

Here the first term corresponds to the direct ionization. The second term gives the contribution from the two-step process: The transition from the initial state |i > leads to the final state |f > through an intermediate state which is another L substate. We notice that the physical meaning of the exponential function in Eq. (2.24) is related to the concept of the so-called 'increased binding energy', because the V_{ii} diagonal matrix elements of the perturbing potential in first order give the change of the binding energies of the atomic electrons [Ba73].

2.2 Electron Capture

The Coulomb interaction of the projectile with the target electrons may not only induce transitions of the electrons to the contimuum or to the other bound states of the target atom. Target electrons can also be captured into empty orbitals of the projectile. This process, especially for heavy ions of high charge state, contributes significantly to the vacancy production of the target atom.

A simple calculation of the electron capture can be made in the first Born approximation (PWBA), which for hydrogenic wavefunctions gives the Brinkmann-Kramers cross section :

$$\sigma^{Capt} = \frac{8.53 \cdot 10^{-16} \, q^2 \, E_i^{5/2} \, E_f^{3/2} \, E_K^4}{[E_K^2 + 2\,E_K\,(E_i + E_f) + (E_i - E_f)^2]^5} \quad cm^2 \tag{2.25}$$

where q is the effective (screened) charge of the projectile, E_K denotes the kinetic energy of an electron traveling with projectile velocity u, E_i and E_f stand for the binding energy of the transferred electron before and after capture, respectively, and all energies (E_K, E_i and E_f) are to be inserted in KeV units. The initial and final principal shells are assumed to be singly occupied and empty, respectively. The results of the above Eq. (2.25) is systematically higher than experimental

values, typically by a factor 3 to 10 (For detailed discussion about capture see Be80, p.73-148).

For the capture cross sections, and even more for the impact dependent cross sections there is no easy way to obtain the results without elaborate calculations.

2.3 Multiple Coulomb Ionization

Up to this point, Coulomb ionization of atoms has been described in terms of simple perturbation theory as a one electron transition using an independent-electron model of the atom. The experimental evidence of X-ray satellite spectra in the collision of fast heavy ions with complex atoms is a clear indication that more than one electron is excited in such collisions. While the simultaneous ejection of two K-shell electrons occurs with low probability (Hypersatellites), the chance of the simultaneous ejection of less tightly bound electrons increases rapidly with increasing main quantum number.[1].

K-shell vacancy production by ion-impact occurs predominantly in close collisions, where the interaction between the projectile and the target electrons becomes very strong (Fig. 2.3). In contrast, the L-shell vacancy production occurs predominately in collisions with relatively large impact parameters b (several times the L-shell radius), for which the interaction is relatively weak. The close collisions can be identified experimentally by detecting the decay of a K-vacancy via emission of a K X-ray or a K Auger electron. The observed multiple K- and L-shell vacancies originate from impact parameters deep inside the L electron shell. Because of the strong Coulomb interaction in close collisions, the production of one or more L-holes in addition to the K-hole is quite probable. The configurations with one or more L- shell vacancies show up as satellites of the X-ray or Auger K diagram lines. A theoretical description of the process of producing L vacancies and a K vacancy in the same collision has been developped and has proved to be a useful basis for comparing various collision systems. A major assumption in the theory is that the ionization of a particular electron is not correlated with excitations of other electrons within the same atom.

According to this independent electron model, the probability $P_{mK,nL}(b)$ that a collision with impact parameter b produces m vacancies in the K-shell and n vacancies in the L-shell vacancy is given by the joint binomial distribution:

$$P_{mK,nL}(b) = \binom{2}{m}\binom{8}{n}\Big(p_K(b)\Big)^m\Big(1-p_K(b)\Big)^{2-m}\Big(p_L(b)\Big)^n\Big(1-p_L(b)\Big)^{8-n} \quad (2.26)$$

[1]At the moment, as the concepts are better understood if we confine ourselves to simultaneous K- and L- shell ionizations, we assume that the excitations of the M and higher shells have a negligible effect on the K shell and that it is not necessary to distinguish the separate contributions of the three L subshells to $P_L(b)$.

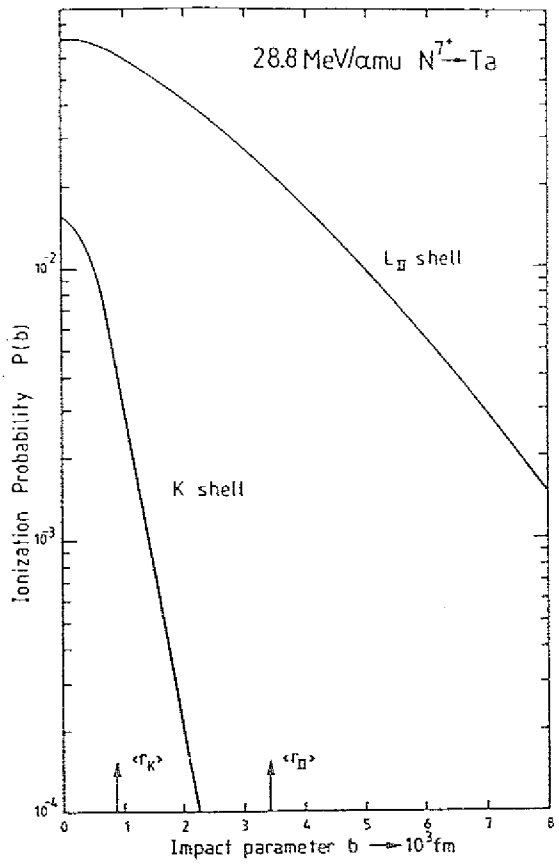

Figure 2.3: *Impact parameter dependence of the K− and* L_{II}*−shell ionization probabilities for 28.8 MeV/amu* $N^{7+} \rightarrow Ta$ *[Am90].*

where $p_K(b)$ and $p_L(b)$ are the probabilities for the one electron ionization of the K and L shell, respectively, defined by Eq.(2.13).

The corresponding cross section is obtained by integration over the impact parameter:

$$\sigma_{mK,nL} = 2\pi \int_0^\infty b\,db\,P_{mK,nL}(b) \tag{2.27}$$

Since, even at high impact velocities, $p_L(b)$ is slowly varying in the region near the nucleus where $p_K(b)$ differs from zero (see Fig. 2.3), we find that

$$\begin{aligned} \sigma_{1K,0L} &= 2\pi \int P_{1K,0L}(b)\,b\,db \\ &\approx 4\pi\,[1-p_L(0)]^8 \int_0^\infty p_K(b)\,[1-p_K(b)]\,b\,db \end{aligned} \tag{2.28}$$

and similarly,

$$\sigma_{1K,1L} \approx 32\pi\, p_L(0)\,[1-p_L(0)]^7 \int_0^\infty p_K(b)[1-p_K(b)]\, b\, db \tag{2.29}$$

The relative probability R for the creation of a state with one K and one L hole relative to the state with K hole only, is given by:

$$R = \frac{\sigma_{1K,1L}}{\sigma_{1K,0L}} = 8\,\frac{p_L(0)}{[1-p_L(0)]} \tag{2.30}$$

Consequently, the satellite structure of the K−series diagram lines provide information on $p_L(0)$, the zero− impact parameter probability for producing a vacancy in the L shell. According to Eq.(2.13), for ionization probabilities which fulfill the condition $p_L(0) << 1$ the relative probability R is proportional to Z_1^2, where Z_1 is the nuclear charge of the projectile.

Until now we have not distinguished the individual contributions of the three L subshells to $p_L(b)$ and we have assumed that excitations of the M and higher shells have a negligible effect on the K shell. To improve these approximations the formalism can be generalized in the framework of the independent electron model as follows:

We consider one particular (sub)shell i, containing n electrons with $p_i(b)$ the calculated ionization probability per electron. The probability $P_{mi}(b)$, at a certain impact parameter b, for producing m vacancies in this atomic (sub)shell, is given by [Ha72]:

$$P_{mi}(b) = \binom{n}{m}\Big(p_i(b)\Big)^m\Big(1-p_i(b)\Big)^{n-m} \tag{2.31}$$

The cross section of a certain configuration j for simultaneous ionization of electrons from different (sub)shells can be calculated as [Ha72,McG77]:

$$\sigma_j = 2\pi \int_0^\infty b\, db \prod_i \binom{n_i}{m_i}\Big(p_i(b)\Big)^{m_i}\Big(1-p_i(b)\Big)^{n_i-m_i} \tag{2.32}$$

where i denotes the (sub)shells. The meaning of the parameters n_i, m_i, p_i is the same as in Eq.(2.31), for the particular shell i.

It is not so obvious to relate the cross sections for production of more than one vacancy in the L shell to the one−electron transition probabilities previously derived. As a successive number of electrons is taken out of an atomic shell, the screening effect of the remaining electrons will be appreciably altered, and no simple connection to the one− electron transition probabilities can be expected . A more complete understanding of multiple excitation must await the development of non−perturbative methods for calculating the fundamental transition probabilities.

3. Atomic properties of inner – shell ionized atoms

One missing electron in an inner shell represents an excited, highly unstable atomic state, that will rapidly de – excite by radiative and/or radiationless transitions (Fig. 3.1a).

In the **radiative process** an electron from one of the upper levels fills the vacancy and a photon with a characteristic energy is emitted (Fig. 3.1b). The energy of the emitted photon is given by the energy difference between the final and initial state of the atomic system.

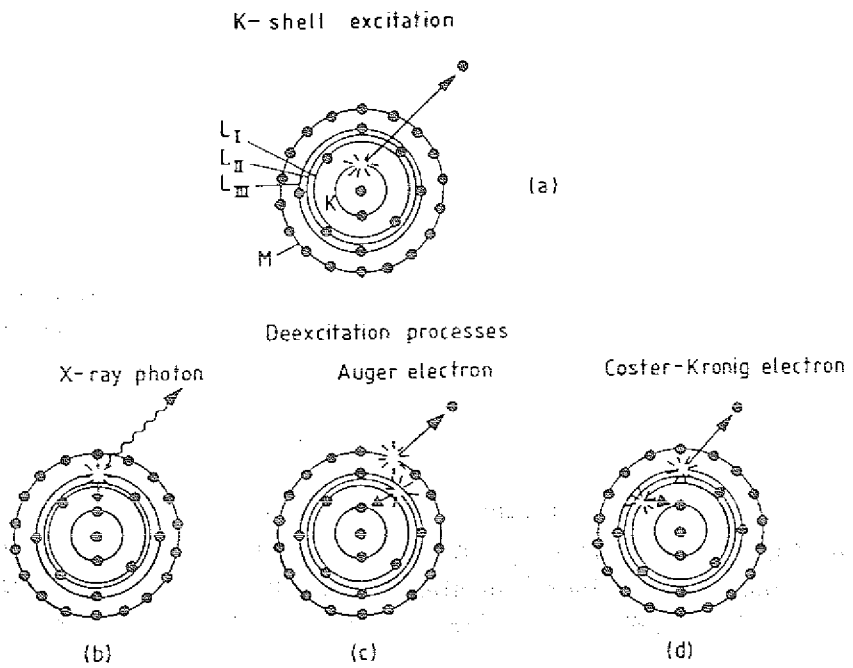

Figure 3.1: *a) A K shell electron is ejected from the atom and a vacancy is created, b) the K shell vacancy is filled by an L shell electron through a radiative transition, and the difference in binding energies is given off as a characteristic X – ray photon, c) the K shell vacancy is filled by an L_I sub – shell electron through a radiationless Auger transition, as the difference in binding energies is taken up to eject a second electron from M shell, d) the K shell vacancy is filled by an L_I subshell electron through a radiationless Coster – Kronig transition, as the difference in binding energies is taken up to eject a second electron from the same shell, but the L_{III} subshell.*

In the **radiationless process** the energy difference transfered during the electronic transition from the less bound initial state to the more bound final state, is used to eject a second electron, so that the atom is doubly ionized (Fig. 3.1c,d). Thus when the excited atom goes to lower energy state through a radiationless transition, an electron is emitted rather than a photon.

In the following chapters are discussed the atomic binding energies and the X-ray transitions energies (3.1), the approximations to calculate them in the framework of single particle problem (3.1.1) and in the more rigorous way of a many body problem (3.1.2). The origin of the X-rays satellite lines is discussed in part 3.2. In the part 3.3 a brief description of the radiationless process and their consequences in the X-ray spectra is given. Finaly in part 3.4 the lifetimes and the transition yields for the various process are discussed in the case of singly ionized atoms.

3.1 X-ray transition energies

As we have mentioned, the energy of a X-ray transition is given by the energy difference between the final and initial state of the atomic system:

$$E_{X-ray} = E_f - E_i \tag{3.1}$$

where E_f and E_i are the total energies of the atomic system in the final and initial state, respectively.

The *ab initio* evaluation of the X-ray transitions therefore entails the determination of the total energy of the atomic system in two electronic states. In principle the total energy E of an atom can be calculated by solving the quantum mechanical equation:

$$H\ \Psi = E\ \Psi \tag{3.2}$$

where H is the generalized Hamiltonian operator and Ψ is the many-particle wave function that describes the electronic state under consideration. An exact solution of Eq.(3.2) has not been found for atoms with more than a single electron; even for helium-like atoms only approximate solutions of the Schrödinger equation have been achieved through quite complicated methods. Many-electron atoms are even more complex, and less exact methods must be exploited.

3.1.1 Hole binding energies in singly ionized atoms

In an approximation, the complex many body problem can be reduced to the more handsome single particle problem. Pauli has shown that the treatment of a shell with n vacancies and m electrons is completely equivalent to the case with m vacancies and n electrons [Pa25]. Consequently, the X-ray characteristic spectrum, which in first approximation originates from the lack of one electron is equivalent to the spectrum of an atom in which one hole is present in an inner

shell. The discussion of characteristic X-ray spectra can be based on the theory of the spectra of 'hole hydrogenlike' atoms. In this atom the hole is moving in the Coulomb field of the atomic nucleus and of the electrons.

Therefore, the energies of the corresponding states (one hole in the field of the nucleus and of the electrons) can be calculated by the theory for the energy levels in electronic hydrogenlike atoms [1] provided that the following modifications are made [Ag79]:

i) The bound electron in an atom has negative energy. Therefore the energy of a hole state is taken to be positive.

ii) The nuclear charge Z is replaced by an effective charge Z_{eff}= Z-S(n,l,j), where S(n, l, j) is the screening factor. The screening factor modifies the actual nuclear Coulomb potential as the nuclear charge Z is screened to some extent by the presence of the electrons.

A qualitative representation of the relevant atomic levels is shown in Fig. 3.2. Although one-electron symbols are retained, each level denotes the energy of the entire system when one electron is missing from the particular electronic shell. During the hole transition from a higher level to a lower level in this energy diagram, the surplus of energy is released frequently by emission of a photon. The energy of the emitted X-ray is given by the energy difference of the initial and final atomic state.

Lines that arise from an electron (or one hole) transition in a singly ionized states atom, with the inactive electrons retaining their original quantum numbers, are known as **diagram** lines.

---

[1] In a hydrogenic atom the atomic nucleus of charge Ze and the electron of charge -e interact via the Coulomb potential:

$$V(\vec{r}) = -\frac{Z \cdot e^2}{r} \tag{3.3}$$

where r is the distance between the two particles. Solving the one particle time-independent Schrödinger equation

$$[\frac{\vec{p}^2}{2m} + V(\vec{r})]\,\Psi(\vec{r}) = E\,\Psi(\vec{r}) \tag{3.4}$$

the energy eigenvalues E_n are given by:

$$E_n = -\,m\,a^2\,c^2\,\frac{Z^2}{2\,n^2} \tag{3.5}$$

where n is the principal quantum number (n=1,2,...), a=1/137 is the fine structure constant, m the electron mass and c the light velocity.

The exact solution for hydrogenic atoms has to use the Dirac equation, which satisfies the requirements of special relativity as well as those of quantum mechanics. Solving the Dirac equation for an electron in the central field V(r) of the nucleus, the binding energies are given as :

$$E_{nj}^{Dirac} = mc^2\left\{\left[1+\left(\frac{Za}{n-j-1/2+\sqrt{(j+1/2)^2-Z^2a^2}}\right)^2\right]^{-1/2}-1\right\} \tag{3.6}$$

where j is the total angular momentum quantum number. As compared to nonrelativistic energies E_n which are $2n^2$ times degenerate, the Dirac theory removes this degeneracy partly. The corresponding splitting is called fine structure splitting, the n levels with j=1/2, 3/2,..., n-1/2 form a **fine structure multiplet.**

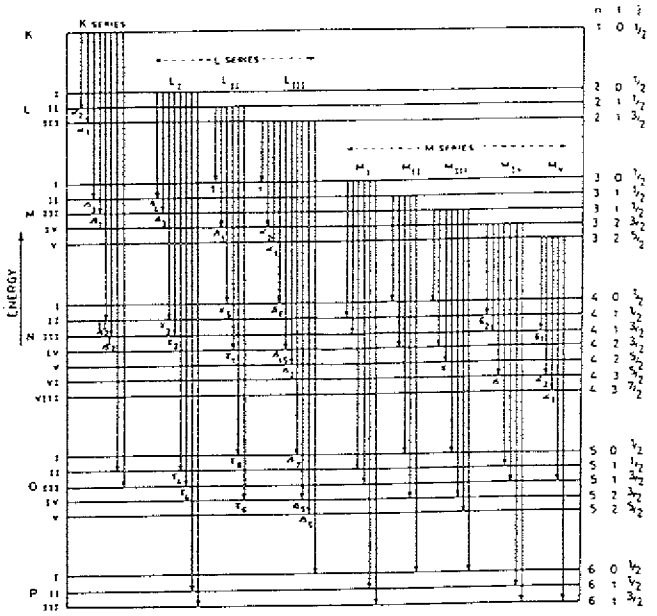

Figure 3.2: *Qualitative X-ray atomic energy level diagram. Some of the allowed electric-dipole transitions are shown by arrows. The electric-dipole selection rules are* $\Delta n \neq 0$, $\Delta l = \pm 1$, $\Delta j = 0, \pm 1$. *(the j-j transition* $0 \rightarrow 0$ *is forbidden) [from Ag79].*

3.1.2 Electron binding energies as a many-body problem

Whereas many features of X-ray spectra can be explained by the one-hole model using hydrogenlike wave functions, an adequate description of X-ray process like atomic binding energies, X-ray transition energies, and X- ray transition rates should take into account the manner in which the rest electrons are affected by the change of the potential due to the creation of the initial hole or its decay. To do this, we need the many-electron wave functions of the initial and final states. To find the many-electron wave functions the Hartree-Fock or **self-consistent field method** approximation is used. The starting point of this approach is the independent particle model, according to which each electron moves in an effective potential which takes into account the attraction of the nucleus and the average effect of the repulsive interactions with the other electrons. Each electron in a multielectron system is then described by its own wave function. In the Hartree approximation the total wave function for the atom (ion) is not antisymmetric in the electron coordinates. The generalization of the Hartree method which takes into account this antisymmetry requirement - imposed by the Pauli exclusion principle - is known as the self- consistent-field Hartree-Fock approach (SCF-HF) and its relativistic version, the Dirac-Hartree-Fock (SCF-DF) method [see for example Br 83,p. 320].

As the effect of relativity on inner-shell binding energies depends very strongly on the atomic number Z (see Eq. 3.6) the most useful appproach which can be

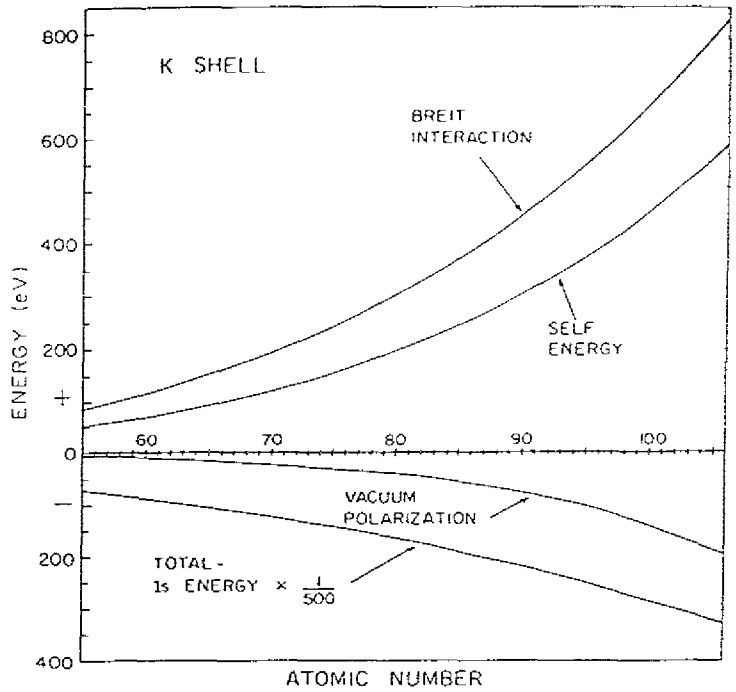

Figure 3.3: *Shifts produced in the 1s-level energy of heavy atoms by the Breit interaction, self energy, and vacuum polarization [from Ch81].*

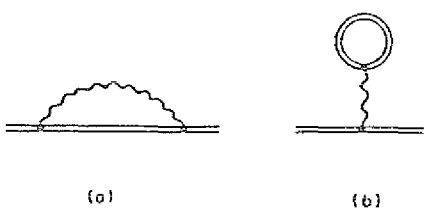

Figure 3.4: *Feynman diagrams for the lowest order a) self energy and b) vacuum polarization in one-electron atoms. The double line represents the electron bound to the nucleus, and the wavy line represents the virtual photon.*

Feynman diagram in Fig. 3.4a, in which the double line represents the electron bound to the nucleus, and the wave line represents the virtual photon. The effect reduces the magnitude of the binding energy [Fig. 3.3]; it is more pronounced for inner than for outer levels, and greater for s states than for p states [Ch85].

The second important radiative shift of energy levels is the vacuum polarization correction which arises because the effective potential seen by an electron is modified by the polarized vacuum charge distribution, due to virtual electron-positron pairs. The photons exchanged between the electron and the nucleus, that transmit the attractive force between the particles, can create virtual electron-positron pairs in the exchange process. This possibility, represented by the Feynman diagram in Fig. 3.4b, modifies the interaction between the electron and the nucleus. This effect is important for penetrating orbitals which can bring electrons

close to the nucleus. The effect of vacuum polarization reduces the self-energy shift slightly (or increaces the binding energy) (Fig. 3.3).

3.2 X-ray satellite lines

Until now we have supposed that the transitions take place in singly ionized atoms. On the other hand if the transitions occur in atoms multiply ionized in inner shells the level energies are changed due to the modification in screening. That means that the corresponding X-ray transition has an energy which can be somewhat different from that of the diagram line. These transitions are close to the diagram lines and they are called **satellites** because of their vicinity to the (usually strong) parent line, or **nondiagram** lines, as they cannot be understood as simple transitions in the usual X-ray energy level diagram of a singly ionized atom. A satellite line is produced when a transition of the type AY $\rightarrow$ BY occurs among the doubly ionized states. The satellite lines usually occur on the high-energy side of the diagram line A $\rightarrow$ B. The additional hole Y acts as a spectator.

As an example, we discuss the transition energies in the case of a diagram K_α transition (hole transition from K $\rightarrow$ L), and the case of K_α transition with a L spectator hole (KL $\rightarrow$ LL), using the following crude model. For the diagram transition the energy of the emitted photon is given by :

$$E_{Diag} = E_K - E_L,$$

where E_K and E_L are the energies of the atomic levels when the hole is in the initial K shell and in the final L respectively, as they are given from the hydrogenic model. For the satellite line the energy of the emitted photon is given by :

$$E_{Sat} = E_{KL} - E_{LL}$$

where now in the initial and final state there are two holes. In first approximation, the energies of the double ionized atomic levels can be estimated supposing a helium-like system as

$$E_{KL} = E_K + E_{L'} \qquad and \qquad E_{LL} = E_L + E_{L''}$$

As the nuclear charge is now somewhat less screened when the L spectator hole is in the final state (LL state) as compared to the initial state (KL), $E_{L'}$ is larger than $E_{L''}$ and consequently

$$E_{Sat} - E_{Diagr} = (E_{L'} - E_{L''}) > 0,$$

Thus, as the presence of an L spectator hole increases the distance between L and K levels, the energy of the emitted photon is higher than that in a singly ionized system. This leads to the appearance of satellite lines on the high energy side of the diagram line.

3.3 Radiationless Processes

The main radiationless processes are the Auger and the Coster-Kronig process. During the Auger process an inner-shell vacancy is transferred from one shell of the atom to another, less tightly bound. In the Coster-Kronig process an inner-shell vacancy is transferred from one subshell of an atom to another less tightly bound subshell, of the same shell (see Fig. 3.1).

Coster-Kronig transitions have certain special characteristics, like high transition rate and low transition energies. The Coster-Kronig transitions tend to provide the dominant channel, if they are energetically possible. Many Coster-Kronig transitions are only possible in discrete regions of the periodic table. The reason for this is that the kinetic energy E_{kin} of the electron which ejected in the continuum during the radiationless transition $i \rightarrow (f, y)$ is given by

$$E_{kin} = E_i - E_f - E_y \tag{3.11}$$

where E_i and E_f are absolute values of neutral-atom binding energies, while E_y is the binding energy of the y electron in the presence of a vacancy in state f. In Coster-Kronig transitions, $E_i - E_f$ is the difference between the binding energies of two subshells in the same level, which is relative small. In many cases this subshell binding-energy difference is smaller than E_y with the result that the transition is energetically not possible.

The radiationless transitions have three important consequences to the X-ray spectra:

i) They compete with the radiative transitions in the de-excitation process. Therefore they influence the width of the emitted X-ray lines.

ii) They transfer vacancies from one shell to another, and influence the intensity of the X-ray emission lines in this way.

iii) They create double ionized atomic states, and therefore provide conditions for the appearance of satellite lines in X-ray spectra.

3.4 Transition rates - Natural widths

Let ω_{fi} be the transition probability per unit time, of the transition $|i> \rightarrow |f>$. The total transition rate S_i (total probability per unit time), that the atom will leave the initial state $|i>$ in some way and make a transition to some other final state $|f>$, is given by:

$$S_i = \sum_f \omega_{fi} \tag{3.12}$$

where the summation is over all the possible final states $|f>$. The lifetime T of a single hole state is the inverse of the total transition rate S, $T = 1/S$. The natural width Γ of that level is related to the lifetime time T and to the transition rate S by the uncertainty principle:

$$\Gamma = \frac{\hbar}{T} = S\hbar \tag{3.13}$$

Assuming that the different decay modes are independent, the total transition rate S will be given by the sum of the partial rates :

$$S = S_R + S_A + S_C \tag{3.14}$$

and the total level width (natural width) by :

$$\Gamma = \Gamma_R + \Gamma_A + \Gamma_C \tag{3.15}$$

where the subscripts denote the radiative, Auger, and Coster-Kronig processes, respectively.
The yields for the various processes are defined as follows:

$$\text{Radiative or fluorescence yield} \quad \omega = \frac{\Gamma_R}{\Gamma} \tag{3.16}$$

$$\text{Auger yield} \quad a = \frac{\Gamma_A}{\Gamma} \tag{3.17}$$

$$\text{Coster-Kronig yield} \quad f = \frac{\Gamma_C}{\Gamma} \tag{3.18}$$

The sum of radiative yield ω and radiationless yields a and f is unity:

$$\omega + a + f = 1 \tag{3.19}$$

In Fig. 3.5a the total theoretical atomic level widths for K and L subshells are displayed to visualize the trend of level widths as a function of the atomic number Z [Kr79b]. The width of a X-ray transition is given by

$$\Gamma(X \rightarrow Y) = \Gamma(X) + \Gamma(Y) \tag{3.20}$$

where X and Y are the levels involved in the transition. In Fig. 3.5b the natural widths of the $K\alpha_1$ line are shown, as function of Z [Kr79b].

Analogously, the width of an Auger or Coster-Kronig transition is given by :

$$\Gamma(X \rightarrow YZ) = \Gamma(X) + \Gamma(YZ) \tag{3.21}$$

where YZ is a double-hole configuration.

Figure 3.5: *a)Natural widths of K and L levels as a function of the atomic number Z and b)Natural widths of* $K\alpha_1$ *X-ray lines [from Krause M.O. and Oliver J.H., J. Phys. Chem. Ref. Data 8, 329 (1979)].*

4. Experimental set – up

The study of K X – rays satellites requires that at least the K X – ray transitions in the presence of L spectator hole can be resolved from the X – ray transitions in the region of the K diagram line. Therefore a high resolution detector is required. For photons in the energy region of 1 KeV to some hundreds of KeV the best energy resolution can be obtained with crystal spectrometers.

4.1 The principle of crystal spectrometers

According to Bragg's law a photon beam, hitting a crystal is reflected if an integer multiple n of the wavelength λ and the incidence angle θ_B fulfill the relation :

$$n\,\lambda = 2\,d\,\sin(\theta_B) \tag{4.1}$$

where d is the lattice constant.

The photon's wavelength λ and energy E are connected according to :

$$\lambda = \frac{h\,c}{E} \tag{4.2}$$

where h is the Planck's constant h and c the light velocity. The value of the constant hc is 12398.4244 Å·eV [Pa88].

The incident radiation is reflected within a small angle $\Delta\omega$, as it is shown in the Fig. 4.1. The reflectance for a ray incident at a glancing angle θ_i is determinated by a function $W(\theta_i - \theta_B)$, which is called the crystal rocking curve. The rocking curve is characteristic for the specific crystal, the wavelength λ and the order of reflection n, and it determines the resolution of the corresponding flat single crystal spectometer. As for a small source the Bragg condition is fulfilled only for a narrow region of the crystal such a device has low efficiency.

A considerable increase of efficiency is obtained using focussing crystal spectrometers with curved crystals. If the radius of curvature R equals the diameter of the Rowland circle, radiation from a point source S meets (to first order) the Bragg condition for the entire crystal simultaneously. Consequently the angle of acceptance is no longer the small $\Delta\omega$ but the aperture according to Fig. 4.2, and thus the efficiency can be increased by 2 to 3 orders of magnitude. The monochromatic radiation from a point source at a point S is now focussed into an image in D.

For photon energies smaller than 20 KeV the reflection (Bragg) geometry (Fig. 4.2, left side) is usually applied, as the transmission geometry suffers from the photon beam attenuation due to absorption. With an extended source and a

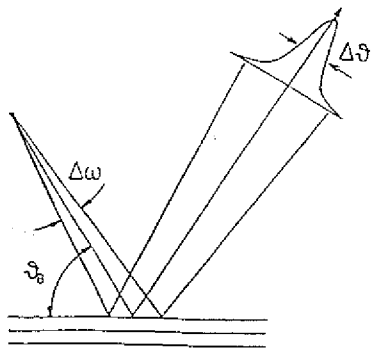

Figure 4.1: *Bragg reflection at a flat single crystal. The radiation from a source S is reflected from the crystal planes C at a reflection angle θ_i. Only within the angular range $\sim \Delta\omega$ radiation is reflected. The line shape of the reflection determines the rocking curve.*

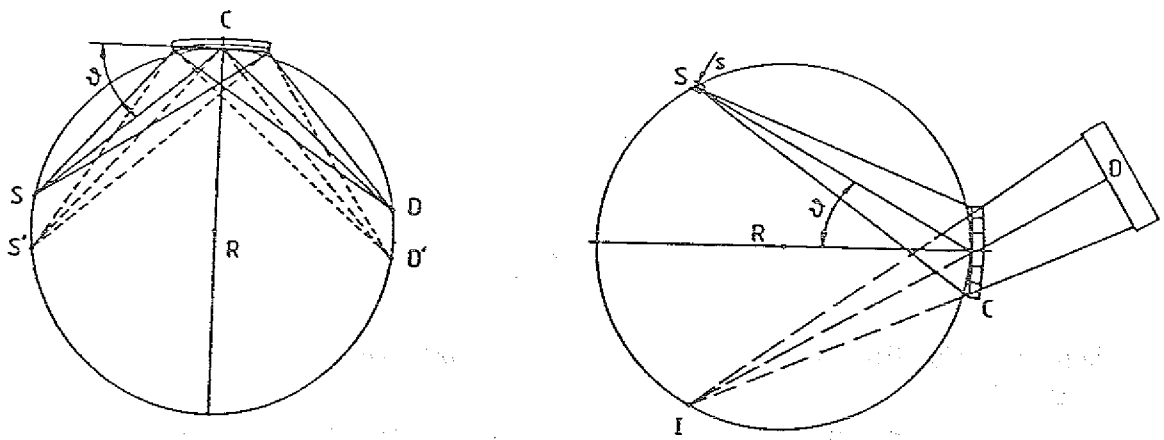

Figure 4.2: *Focussing crystal arrangements. The left side shows the reflection geometry. The radiation from a point source S is focussed to a point image D. Radiation with a lower energy at S' is focussed to a point D'. On the right side the transmission geometry is displayed. Using a small source in S the radiation is reflected from the crystal C to the large detector in D as if it were coming from the virtual image I. This is the DuMond arrangement. Using an extended source at D the radiation passes the crystal in reverse direction and is focussed to the point at S. This is the Cauchois spectrometer.*

position sensitive detector this spectrometer type allows a spectrograph mode of operation.

For energies higher than 20 keV the transmission (Laue) geometry is commonly used, and two different types of operation are possible. In the DuMond arrangement a small source S is placed on the Rowland circle and the diverging beam is diffracted into an extended detector D (Fig. 4.2, right side). Interchanging the source and the detector leads to Cauchois geometry.

The angular dispersion of the crystal spectometer is given by :

$$D = \frac{d\theta}{d\lambda} = \frac{n}{2d\cos(\theta_B)} = \frac{\tan(\theta_B)}{\lambda} \tag{4.3}$$

and it measures the change of the diffracted wavelength $d\lambda$ per change of the spectrometer angle θ_B.

With the smallest detectable wave length separation $\Delta\lambda$, the resolving power for the crystal spectrometer is defined as:

$$R = \frac{\lambda}{\Delta\lambda} = \frac{E}{\Delta E} = \tan(\theta_B)\,\Delta\theta \tag{4.4}$$

where $\Delta\theta$ is the FWHM of the recorded spectrum of a monoenergetic line. The angular uncertainty $\Delta\theta$ depends on the structure of the crystal and on the experimental parameters.

The energy resolution ΔE as a function of the energy E is given by :

$$\Delta E = \frac{2d}{nhc} E^2 \sqrt{1 - \left(\frac{n\,h\,c}{2d\,E}\right)^2}\,\Delta\theta \tag{4.5}$$

In the case that the reflection takes part within small Bragg angles ($\sin(\theta_B) \rightarrow 0 \Rightarrow nhc/2dE \ll 1$), Eq. (4.5) can be approximated as :

$$\Delta E = \frac{2d}{nhc} E^2\,\Delta\theta \tag{4.6}$$

Consequently for high energy photons the resolution decreases drastically. In the region above 1 MeV it usually becomes comparable to that of solid state detectors.

For a DuMond type spectrometer the experimental resolution is essentially determined through the crystal width, imperfectness of the crystal curvature and through the geometrical source width.

4.2 The experimental set – up

Due to the demands of high resolution the X – ray measurements have been performed with a DuMond – type curved crystal spectrometer, which was installed close to the beamline of the cyclotron JULIC (Fig. 4.3).

The existing accelerator facility consists of two ECR ion sources ISIS, the external injection system, the isochronous cyclotron JULIC, and external beamlines. The big superconducting 14 GHz ECR (Electron Cyclotron Resonance) source produces heavy ions, and the other one (5 GHz ECR with normal coils) produces the proton beam [Beu87]. The cyclotron can accelerate heavy ion beams up to mass A=40 with energies between 22.5 and 45 MeV per nucleon.

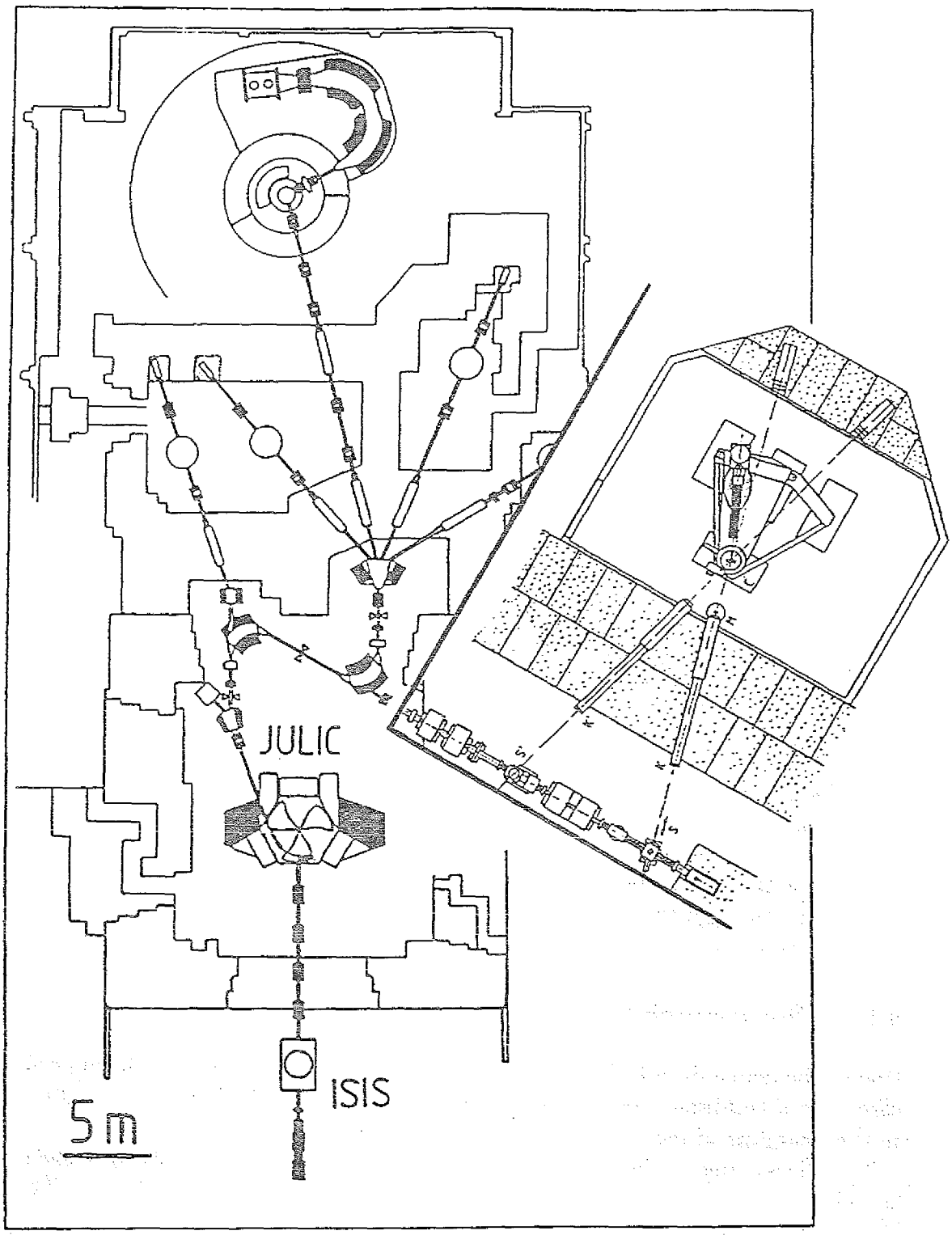

Figure 4.3: *Overview of the accelerator facility with the curved crystal spectrometer installed at a beam - line.*

Only ions with a charge to mass ratio Q/A > 1/3 could be accelerated by the cyclotron JULIC [Beu88].

The principal arrangement of the focussing DuMond type diffraction spectrometer is shown in Fig. 4.4. The main components are a thin source on the focal circle, the crystal, the detector system, the data acquisition system, the device for very precise angle measurements and the electronic control system.

4.2.1 The X-ray source

For on-line experiments at the cyclotron the target (X-ray source) is placed in a cubic reaction chamber. The targets, foils with a width of $\sim$ 2-3 mm, a height $\sim$ 25 mm and a thickness of few hundred μm, are mounted in a U-profile cooled support fabricated out of a thin graphite frame to minimize the background production. This support keeps the target flat whereas the cooling system minimize the distortions due to the thermal expansion of the foil. The target can be rotated around the vertical axis to achieve minimum target width as seen from the spectrometer. Provisions were made to tilt the target around the axis source-crystal so that the line source can be oriented parallel to the diffraction planes of the curved crystal.

4.2.2 The crystal

It consists of a quartz (SiO_2) plate, which is cut and oriented in such a way that the reflection occurs from the (110) plane (2d=4.91 Å). The crystal is bent by imprisonment between two steel blocks to a focal length of 464 cm. The dimensions of the crystal is $100\times100\times4\,mm^3$, while the useful part of the crystal is defined by a 5 cm diameter window in the steel blocks. The opening angle of the spectrometer is about 0.35 msr and the geometrical efficiency due to the crystal effective size is in the order of $\sim 3.10^{-5}$.

Due to mechanical reasons the maximum Bragg angle of the experimental set-up is 10°. In order to measure reflections at positive and negative Bragg angles the range is chosen as ±5°. With this crystal and taking into account that $\theta_B^{max} = 5°$, the minimum photon energy which is possible to measure is about 29 keV.

4.2.3 The photon detection system

Radiation of γ- or X-rays from the target at the source position S reach the curved crystal C after passing through a collimator K that contains lead diaphragms in order to suppress background radiation. The direction of detected photons is at 110° with respect to the beam axis.

After reflection from the (110) crystal planes the divergent photon beam passes a slit collimator which focusses on the virtual source. The collimator is 1 m long and consists of 1.00 mm thick lead plates which are separated by tapered steel

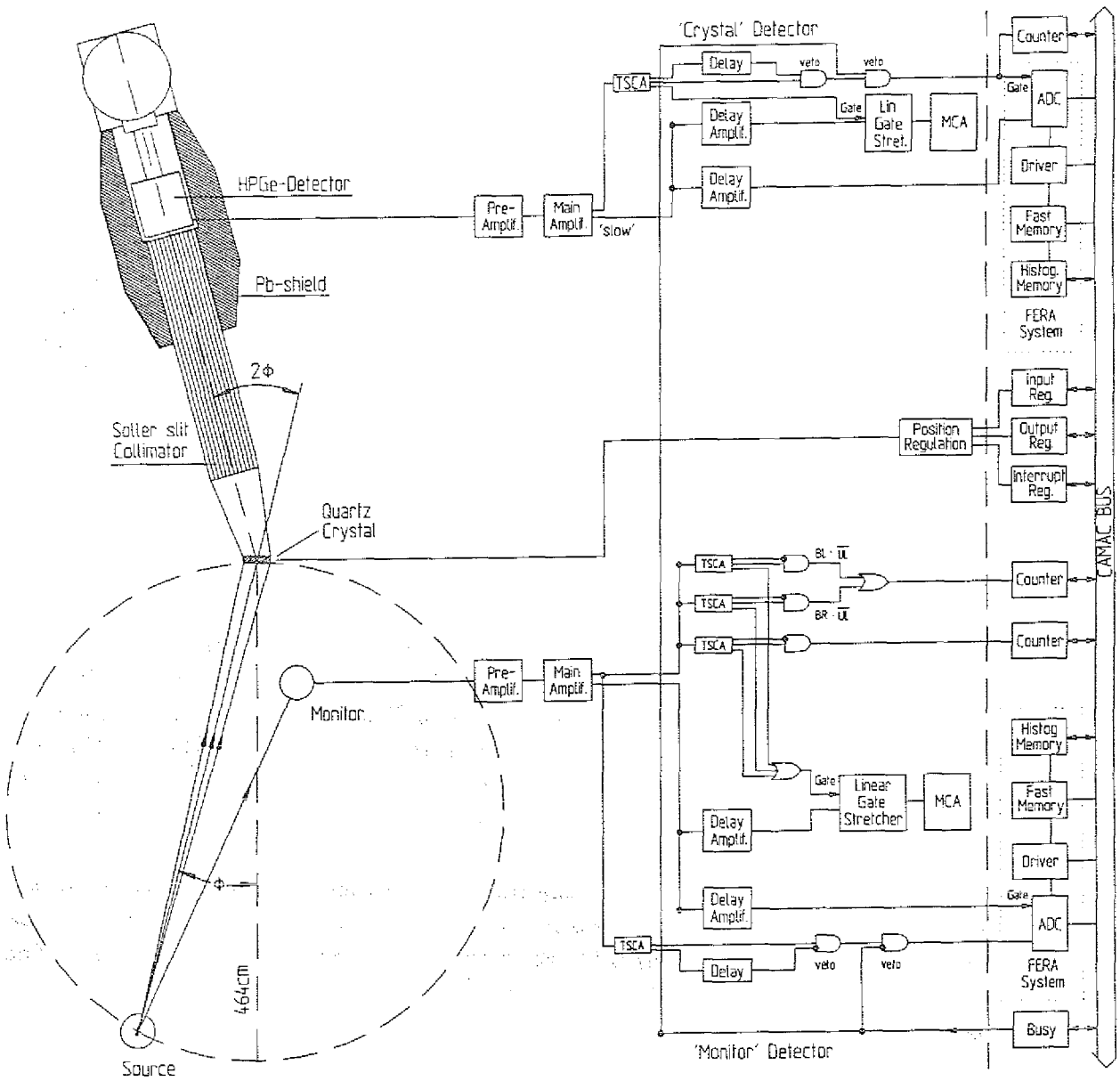

Figure 4.4: *Principal arrangement of the focussing DuMond crystal spectrometer with the main components. The block diagram of the electronic components of the photon measuring system is shown.*

spacers 1.4 mm wide at the collimator entrance. The maximum transimission is $\sim$ 60% within an angular range a of ± 15", around the ideal setting of the collimator. For optimal operation the collimator should follow the angular movement of the crystal so that $\mid a \mid = \mid \theta_{\text{collimator}} - 2\,\theta_{\text{B}} \mid < 10$".

This is accomplished by an optical system consisting of a flat mirror rigidly connected to the collimator, another flat mirror mounted on the quartz-crystal holder, a laser as light source and a differential photocell. The image of the laser beam is detected by a differential photo cell, which produces a correction signal for $a \neq 0$. This signal activates the motor which moves the detector and collimator so that $\mid a \mid$ decreases. The accuracy of this regulation is better than ± 5" [Bo86].

The photons which have passed the collimator are detected by a HP-Ge-detector sitting within a lead shield with a wall thickness of 10 cm for background suppression. The detector diameter is about 60 mm and its thickness is 12 mm, having a resolution of about 2.7 keV in the energy region of 60 keV.

The collimator and the shield rest on several steel balls which allow an easy movement of the detection system on a flat steel plate. The rotation around the spectrometer axis is guaranteed by a steel arm which rigidly connects the detection system with a bearing centred on the spectrometer axis.

In order to correct for instabilities of the cyclotron beam intensity, a monitor detector records the X- radiation emitted from the target, in a direction close to the main photon beam. For this reason a Ge(Li) detector is located at position M in Fig. 4.4, closely below the beam from S to C. A gap in the collimator diaphragms permits the transmission of photons from S to M.

4.2.4 Data acquisition system

The block diagram of the electronic components of the pulse measuring system is shown in Fig. 4.4.

The photons reaching the HP Ge detector produce signals that are fed, after preamplification, into two branches: a slow and a fast one. The slow branch is used for discrimination and determination of the photon energy ('energy' branch) and the fast branch for timing coincidences ('time' branch).

In the 'energy' branch the detector pulses are amplified and fed in an analog-to-digital converter (ADC) and to a multichannel analyzer for further analysis. In this way, the radiation reflected from the crystal at each spectrometer position is again energetically analyzed by the Ge detector. Consequently, different reflection orders as well as background radiation can be distinguished.

The signal in the 'time' branch is fed to a timing single channel analyzers (TSCA). In the case of high- energy pulse, which saturates the amplifier, an anti-coincidence signal is generated which blocks the system for 15 microsec. Otherwise the output signal from the TSCA is used as gate for the 'crystal' ADC, and also is fed to a counter which displays the number of counted photons by the 'crystal' detector.

While the ADC data are stored for the off – line analysis the use of the counters permits the on – line control and checking.

The pulses from the monitor detector are amplified and fed, as in the case of the crystal detector, into a slow ('energy') branch and into a fast ('time') branch.

The pulses in the fast branch are fed into three timing single channel analyzers (TSCAs) with equal window widths. The windows are set on the line of a prompt X – ray transition ('peak') and on the background left and right of this line ('background'), respectively. This permits the reduction of background caused by activation of the target atoms. The TSCA output pulses are fed into two counters ('peak' , 'background') the contents of which is thus proportional to the actual reaction rate in the target. A fourth TSCA is used, to provide the gate for the 'monitor' ADC and to generate an anti – coincidence signal in the case of high – energy pulses.

The pulses in the slow ('energy') branch are amplified and fed to the 'monitor' ADC.

The outputs from the detector and monitor ADCs (12 – bit resolution) are stored in two 16 – bit buffers with 16 Kwords. During the ADCs conversion time a busy signal prevents an interference with further events. The contents of the buffers are transfered via the Camac bus to a PDP 11/24 computer and stored together with the actual spectrometer position. After a selected measuring time the spectrometer is moved to a new position by means of a motor in conjuction with a piezoelectric fine regulation and the data taking is restarted.

4.2.5 The angle measuring system

The Bragg angles are measured with high angular accuracy using an interferometric angle measuring system. In principle, it consists of a Michelson interferometer with an additional unit which transforms a rotation into a change of the optical path length [Bo86].

Since the orientation of the spectrometer is constant relative to the source, it is possible to determine the Bragg angle through the measurement of the orientation of the crystal relative to the spectrometer. This is accomplished with the interferometer by counting the number of the interference fringes and observing the direction in which they move during the rotation of the spectrometer crystal.

The purpose of the electronic system (Fig. 4.4) is therefore, to stabilize the interferometer at discrete angular positions, to negate any external disturbance of this position and to change the position when external command is given. The system allows to move with angular steps of about 0.25", at an accuracy in the order of 0.01".

4.3 Calibration

The spectrometer was tested and calibrated with the help of $\gamma-$ and X$-$rays. Due to their negligible natural widths the use of $\gamma-$rays permits the measurement of the spectrometer response function and with a proper adjustment of the geometrical factors, the determination of the crystal diffraction width.

4.3.1 ^{170}Tm radiactive source

The spectrometer has been calibrated and optimized using a radiactive ^{170}Tm source. The Tm foil, less than 0.1 mm thick, has been irradiated in the KFA reactor. The activity was about 1.2 Ci. The source could be adjusted through a rotation around its vertical axis, a translation in the direction of the radiation beam and a rotation around the source$-$crystal axis. Through these operations the source has been positioned on the focal circle with its narrow edge facing the collimator, and adjusted parallel to the (110) planes of the quartz crystal so that the reflection width is minimized.

The 84.262 KeV $\gamma-$line following the β^- decay of ^{170}Tm (Z=69) to ^{170}Yb (Z=70) has been measured in several orders. The relevant part of the decay scheme is given in Fig. 4.5 [Le78]. The $\gamma-$line profile measured in the first order reflection is shown in Fig. 4.6a. The full curve represents the least square fit of a Gaussian profile to the measured spectra. The FWHM of the measured $\gamma-$line is equal to 61.5 eV which correspond to width of 4.5". The accompanying Kα X$-$ray spectrum of ^{170}Yb has been observed (Fig. 4.6b).

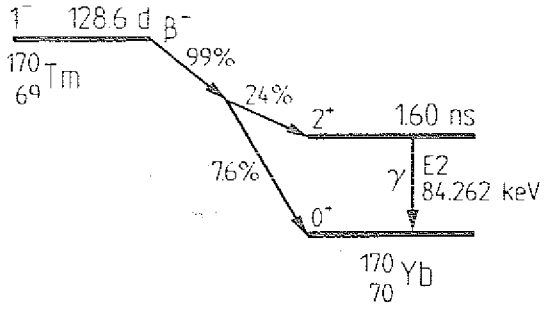

Figure 4.5: *The decay scheme of ^{170}Tm.*

4.3.2 K X$-$ray spectra of lanthanum and tantalum targets bombarded with 25 MeV protons

The induced K X$-$ray spectra from lanthanum and tantalum atoms, during the bombardement with 25 MeV proton beam, have been measured. The proton beam has been used, as there is no observed satellite structure in the induced K X$-$ ray spectra.

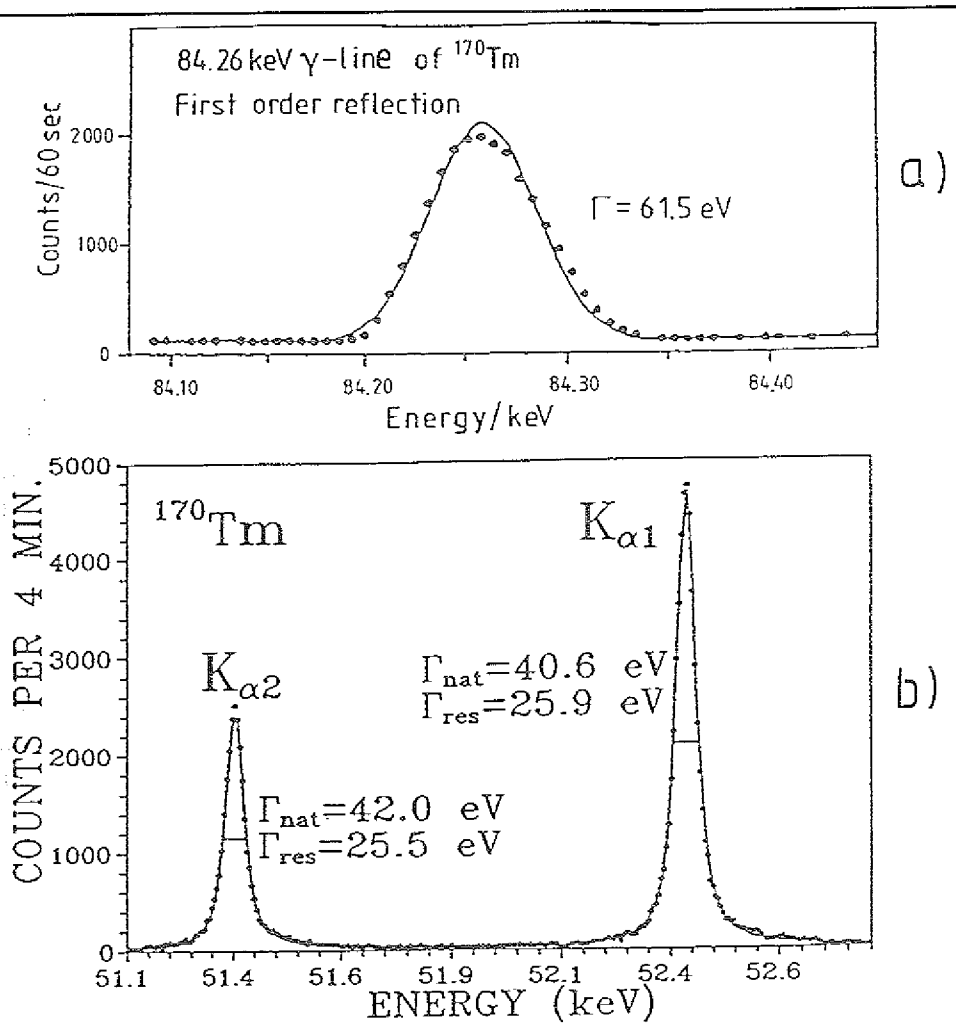

Figure 4.6: *a) The 84.262 KeV γ-line profile in first order reflection. b) First order spectrum of Kα X-rays of* ^{170}Yb.

We have calculated the transition energies and the spontaneous electric dipole rates of the K X-rays diagram lines of the elements under study using the MCDF code of [De75]. The results are given in Tables 4.1 (also the above values for uranium are given). The transition energies are compared to the experimental ones by Bearden [Be67] and the transition rates are compared to the calculations of Scofield [Sc74].

Lanthanum

In Fig. 4.7 are shown the $K\alpha_1$, $K\alpha_2$, $K\beta_{1,3}$, $K\beta_{2,4}$ and KO transitions of La during the bombardement with a 25 MeV proton beam. In the same figure the origin and the nomenclature for the K-series X-rays is given.

Table 4.1a

Transition	Transition Energies *in eV*		Transition Rates *in* sec^{-1}	
	[Be67]	[MCDF]	[Sc74]	[MCDF]
$K\alpha_2$	33034.1 ± 0.2	33030.5	$5.44 \cdot 10^{15}$	$5.57 \cdot 10^{15}$
$K\alpha_1$	33441.8 ± 0.2	33438.9	$9.98 \cdot 10^{15}$	$10.22 \cdot 10^{15}$
$K\beta_3$	37720.2 ± 0.5	37713.7	$0.96 \cdot 10^{15}$	$0.97 \cdot 10^{15}$
$K\beta_1$	37801.0 ± 0.3	37794.9	$1.86 \cdot 10^{15}$	$1.90 \cdot 10^{15}$
$K\beta_5^{II}$	$38074. \pm 2.$		$1.09 \cdot 10^{13}$	
$K\beta_5^{I}$	$38094. \pm 2.$		$1.47 \cdot 10^{13}$	
$K\beta_4$		38701.3	$2.04 \cdot 10^{14}$	$2.01 \cdot 10^{14}$
$K\beta_2$		38718.6	$3.97 \cdot 10^{14}$	$3.96 \cdot 10^{14}$
$K\beta_{2,4}$	38729.9 ± 0.8			
$KO(N_{II})$		38908.2		$3.15 \cdot 10^{13}$
$KO(N_{III})$		38910.9		$6.14 \cdot 10^{13}$
KO mean	$38909. \pm 2.$		$9.32 \cdot 10^{13}$	

Table 4.1b

Transition	Transition Energies *in eV*		Transition Rates *in* sec^{-1}	
	[Be67]	[MCDF]	[Sc74]	[MCDF]
$K\alpha_2$	56277.	56273.4	$1.56 \cdot 10^{16}$	
$K\alpha_1$	57532.	57529.1	$2.72 \cdot 10^{16}$	
$K\beta_3$	64949.	64938.0	$2.91 \cdot 10^{15}$	
$K\beta_1$	65223.	65212.1	$5.62 \cdot 10^{15}$	
$K\beta_5^{II}$	65626.		$6.09 \cdot 10^{13}$	
$K\beta_5^{I}$	65683.		$7.72 \cdot 10^{13}$	

Table 4.1c

Transition	Transition Energies *in eV*		Transition Rates *in* sec^{-1}	
	[Be67]	[MCDF]	[Sc74]	[MCDF]
$K\alpha_2$	94665.	94648.2	$4.17 \cdot 10^{16}$	
$K\alpha_1$	98439.	98430.7	$6.66 \cdot 10^{16}$	
$K\beta_3$	110406.	110407.8	$7.68 \cdot 10^{15}$	
$K\beta_1$	111300.	111288.6	$1.50 \cdot 10^{16}$	
$K\beta_5$	112010.		$5.76 \cdot 10^{14}$	

Table 4.1: *Transitions energies and spontaneous electric dipole rates for the K X-rays diagram lines of lanthanum (Table 1a), tantalum (Table 1b) and uranium (Table 1c) (see text).*

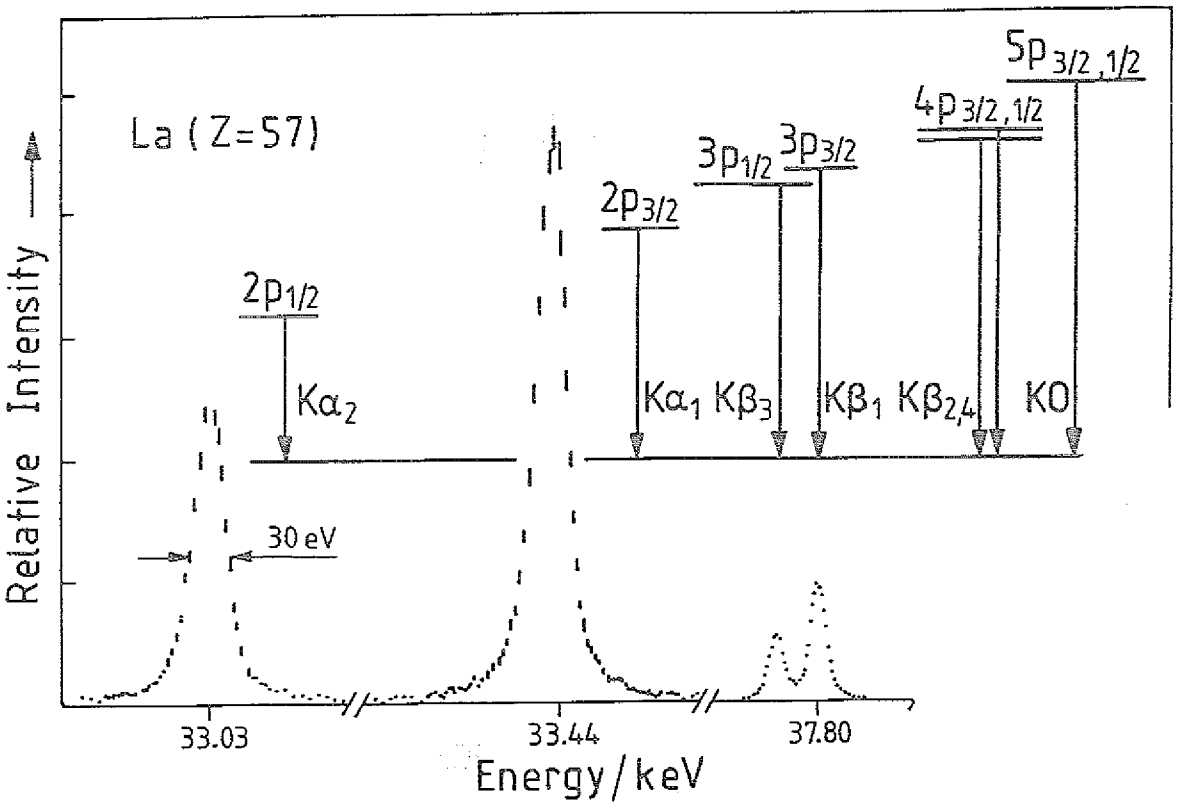

Figure 4.7: *Lanthanum K X-ray induced spectrum as emitted during the bombardment with 25 MeV proton beam. The relative intensities are in scale, but the energy axis is not. The total reflection width of* $K\alpha_1$ *is* $\sim$ *30 eV. The origin and nomenclature for the K-series X- rays is given.*

As can be seen the contribution of L and M satellites is negligible in the La K X-rays induced by the 25 MeV protons; therefore these spectra can be used for a check of the line profile and energy resolution. The line shapes have been fitted by Voigt functions, as a folding of the natural line shape (Lorentzian) and the spectrometer response which is supposed to be a Gaussian. In all the cases the experimental spectra are well described by the Voigt functions, with a reduced $\chi^2 \sim 1$ (Fig. 4.8). The free parameters are the natural widths (Lorentzian FWHM) and the experimental width (Gaussian FWHM). In the cases of doublets the intensity ratio is fixed as given from the literature (see Tables 4.1, [Sc74], [Sa74]) but the energy splitting is a free parameter.

The spectrometer response has been found to be (10±1)", both at positive and negative Bragg angles. The contribution from the crystal diffraction width is expected to be 5". The rest is attributed to the angular width of the source and the defocusing width. Of course the X-ray spectra are influenced by the Doppler effect, but we have calculated the contribution of the recoiling target atoms to the line shape by means of a Monte Carlo simulation. It could be demonstrated

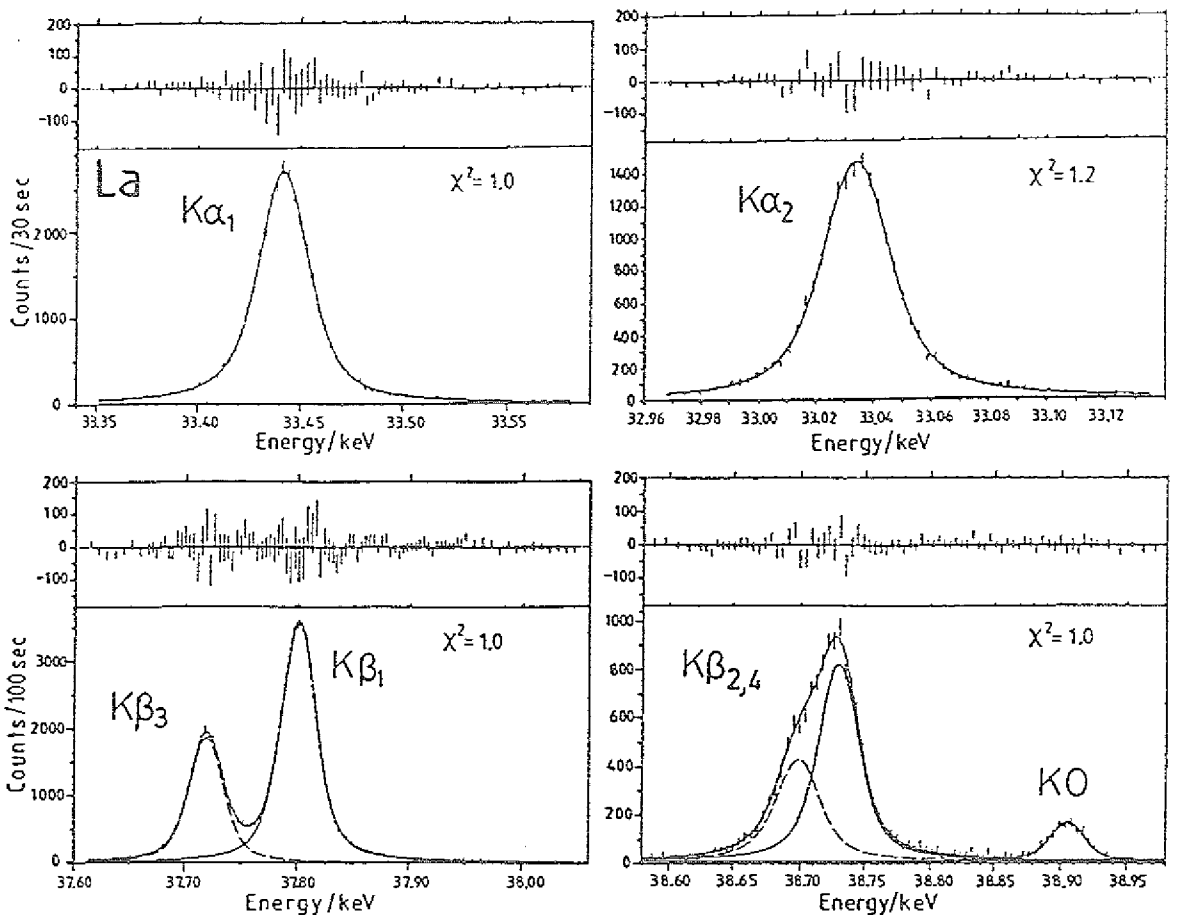

Figure 4.8: *K X - rays reflections measured in first order during the bombardement of La with 25 MeV protons are fitted by Voigt functions. The solid line represents the fit. The differences between fit and experiment data are displayed in the upper part of the figure. Spectrometer response, natural widths and energy differences are extracted (see Tables 2,3). The total reflection width (F.W.H.M.) for the* $K\alpha_1$ *is* $\Delta E_{tot} \sim 30eV$. *[a)* $K\alpha_1$, *b)* $K\alpha_2$, *c)* $K\beta_{1,3}$ *and d)* $K\beta_{2,4}$ *and KO (for these transitions see text)].*

that the contribution of the Doppler effect can be neglected. A detailed discussion about the Doppler effect is given in Appendix A.

The extracted Lorentzian widths, which correspond to the natural linewidths, are given in the Table 4.2. In the same table we quote the values of Salem and Lee [Sa76] and Krause [Kr79b].

Within the estimated errors good agreement has been obtained. The difference of about 2 eV between $K\beta_1$ and $K\beta_3$ is attributed to different level widths of M_{III} and M_{II} subshells. These results do not support the theoretical predictions by [McG72].

Transition	[Sa76]	[Kr79b]	This experiment
$K\alpha_1$	17.6	17.6	18.7±0.7
$K\alpha_2$	18.2	17.8	17.7±1.0
$K\beta_1$	19.3		19.5±0.7
$K\beta_3$	17.2		17.6±0.7

Table 4.2: *Natural widths of lanthanum K X-rays diagram transitions, in eV.*

As a check of the energy calibration of the spectrometer we determined the energy differences between diagram lines and compared them with the data from Tables 4.1. The results are listed in the Table 4.3.

	[Be67]	[MCDF]	This experiment
$\Delta(E_{K\alpha_1} - E_{K\alpha_2})$	407.7±0.3	408.4	406.5±0.5
$\Delta(E_{K\beta_1} - E_{K\beta_3})$	80.8±0.5	81.1	81.6±0.6
$\Delta(E_{KO} - E_{K\beta_{2,4}})$	180.0±1.0	197.3	187.0±1.0
$\Delta(E_{K\beta_2} - E_{K\beta_4})$		17.3	30.7±1.1

Table 4.3: *Energy differences between the lanthanum K diagram transitions, in eV.*

There is very good agreement between the calculated and the experimental values from us as well from [Be67] for the energy differences $(E_{K\alpha_1} - E_{K\alpha_2})$ and $(E_{K\beta_1} - E_{K\beta_3})$.

For the energy difference between transitions from the N and the O shell deviations become visible. If we compare the difference between the weighted mean of the $K\beta_{2,4}$ and the KO lines there is a discrepancy between MCDF theoretical prediction and [Be67] of about 17 eV; for our result the difference amounts 10 eV. A fit of the $K\beta_{2,4}$ complex yields an energy difference between $K\beta_2$ and $K\beta_4$ of 30.7 eV, which deviates significantly from the theoretical predictions. The origin of these discrepancies must be attributed to many-body effects in the 4p state. The 4p XPS spectra do not consist of the expected $4p_{1/2,3/2}$ doublet, but of a sharp peak with an unusual shape and a weaker broad distribution of intensity with some structure [Ko75]. Consequently the fitting of the $K\beta_{2,4}$ doublet with a Lorentzian function is incorrect.

Tantalum

The Ta K X-rays produced by bombarding tantalum with 25 MeV protons have been measured in the second order reflection, both at positive and negative Bragg angles. The line shapes of the induced X-rays spectra have been fitted by Voigt functions (Fig. 4.9). The spectrometer responce, for second order reflection, has been found equal (10 ± 2) ".

The extracted Lorentzian widths, which corresponds to the natural line-widths widths are given in Table 4.4. In the same table are listed for comparison the values given by [Sa76] and [Kr79b]. The total reflection widths (F.W.H.M) for the $K\alpha_1$ and $K\beta$'s have been found to be 60 eV. Within the estimated errors the

Transition	[Sa76]	[Kr79b]	This experiment
$K\alpha_1$	46.5	42.6	46.0±2.0
$K\beta_1$	49.0		48.7±2.4
$K\beta_3$	49.0		52.8±2.6

Table 4.4: *Natural widths of tantalum K X-rays diagram transitions, in eV.*

results agree with the values predicted by [Sa76].

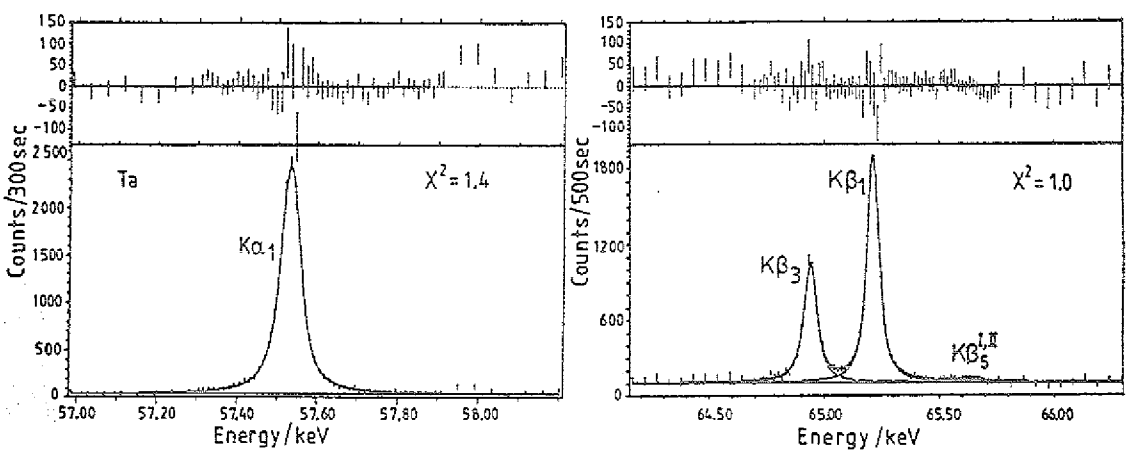

Figure 4.9: *K X-rays reflections measured in second order during the bombardement of Ta with 25 MeV protons are fitted by Voigt functions. The solid line represents the fit. Spectrometer response, natural widths and energy differences are extracted. (a)* $K\alpha_1$, *b)* $K\beta_{1,3}$ *).*

The energy difference between the Kβ_1 and Kβ_3 diagram transitions has been found to be $273. \pm 1.$ eV which is in very good agreement with the difference of $274. \pm 1.$ eV given by [Be67] and the calculated value of 274.1 eV which we found using the MCDF Desclaux code (see Table 4.1b).

5. Analysis of the K X-ray spectra

The K X-ray spectra of lanthanum, tantalum and uranium during the bombardement with energetic heavy ions have been measured. The following colliding systems have been studied :

(200 nA)	403 MeV	$^{14}N^{6+}$	$\rightarrow$	La	(99.91% ^{139}La)
(200 nA)	350 MeV	$^{14}N^{6+}$	$\rightarrow$	Ta	(99.99% ^{181}Ta)
(1 μA)	500 MeV	$^{20}Ne^{8+}$	$\rightarrow$	U	(99.28% ^{238}U)

It is well known that as soon as the projectiles impinge on the targets with high impact velocities, they can be considered as complete ionized [Ma68].

In Fig. 5.1 the lanthanum K X-ray spectra induced during the bombardement with 403 MeV nitrogen beam are shown and they are compared with the the lanthanum K X-ray spectra induced during the bombardement with 25 MeV protons. The lanthanum K X-rays induced by the nitrogen beam, show a complex structure on the high energy side of the corresponding diagram lines.

The tantalum $K\alpha_1$, $K\alpha_2$ and $K\beta_{1,3}$ X-ray spectra induced by 350 MeV $^{14}N^{7+}$ and 500 MeV $^{20}Ne^{10+}$ beam in comparison to the X-rays spectra induced by the proton beam are shown in Fig. 5.2. As in the case of 403 MeV $^{14}N^{7+} \rightarrow$ La, the resulting spectra exhibit a composite structure of 'principal' and 'satellite lines', due to the presence of spectator vacancies in the atom.

The description of the K X-ray satellite structure requires the knowledge of the number of L,M shell vacancies present during the K X-ray transition. This information in turn requires the knowledge of the direct ionization and the capture probabilities of target electrons into the projectile states and as a next step the multiple ionization cross-sections, the redistribution of the vacancies created in collision during the lifetime of the K hole through radiative, Auger and Coster-Kronig transitions and the energy position of the shifted K X-rays. The complexity of K X-ray spectra of multiply-ionized heavy atoms clearly prohibits their decomposition on the basis of the experimental data only, and the theoretical knowledge is necessary to perform this correctly.

5.1 Energy shifts of the satellite lines

As can be seen from Fig. 5.1 and 5.2, during the heavy ion bombardment the atoms are multiply-ionized and the induced K X-rays spectra reveal a satellite structure. The average energy shifts of the satellite lines, due to one spectator hole in L or M subshells (also for N subshell in the case of La), with respect to the $K\alpha_1$, $K\alpha_2$, $K\beta_1$ and $K\beta_3$ diagram lines have been calculated with the multiconfiguration Dirac-Fock program of [De75] and they are listed in Tables 5.1. The energies of

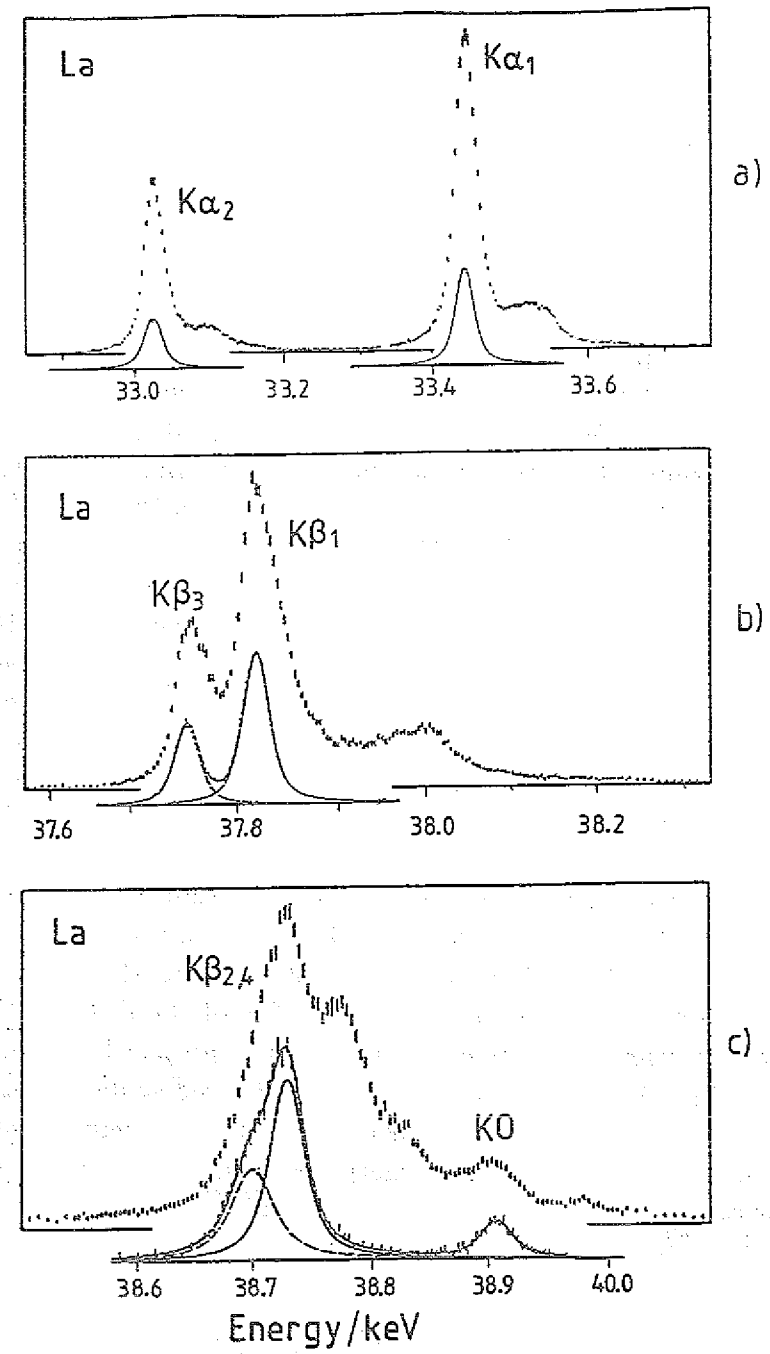

Figure 5.1: *Lanthanum K X-ray induced spectra as emitted during the bombardment with 403 MeV $^{14}N^{7+}$ beam (dotted points with error bars). The comparison with the lanthanum induced spectra during the bombardment with the 25 MeV protons (full lines) reveals the satellite structure in the case of nitrogen projectile. [a) $K\alpha_1, K\alpha_2$, b) $K\beta_{1,3}$ and c) $K\beta_{2,4}$ and KO].*

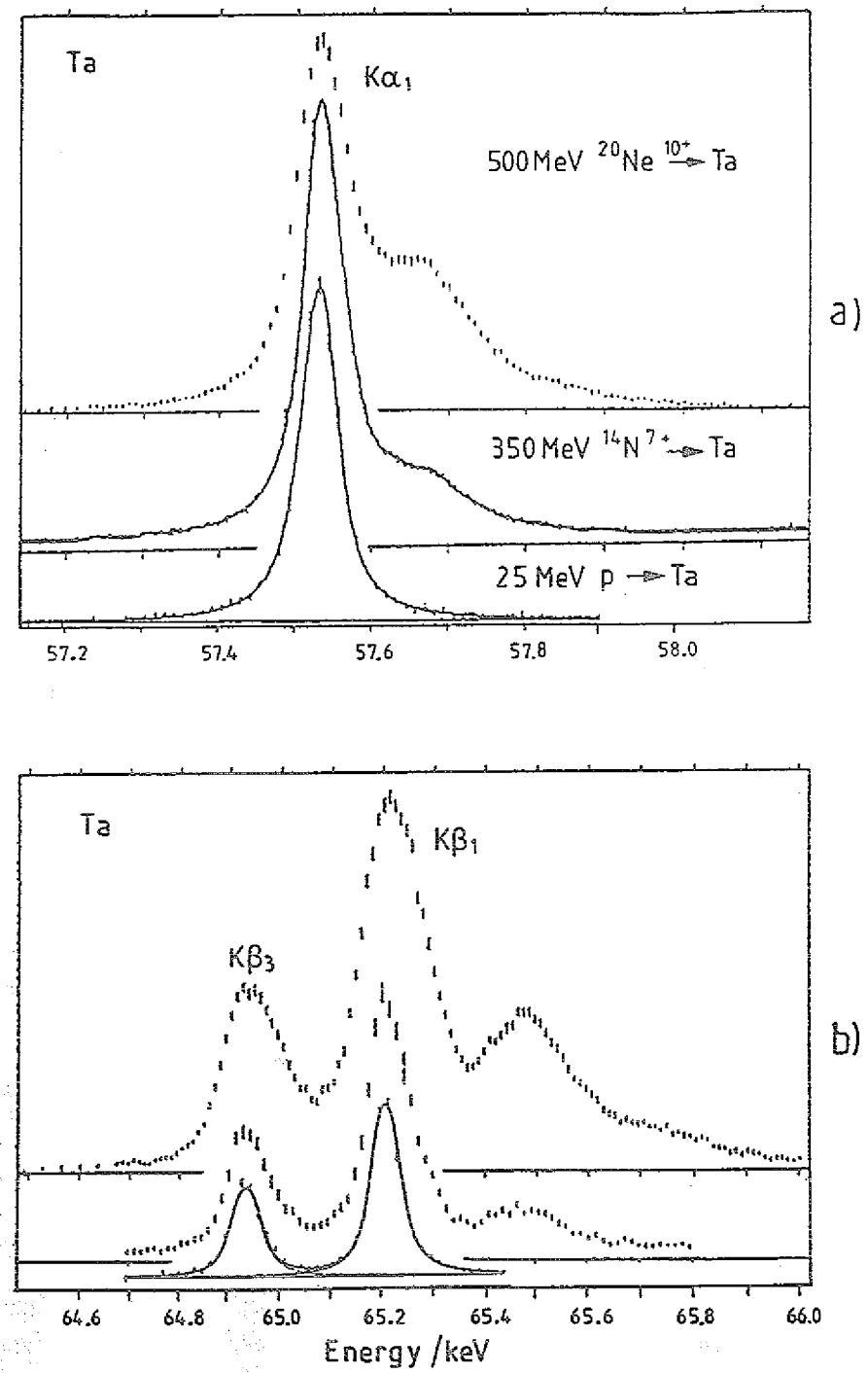

Figure 5.2: *Tantalum K X – ray induced spectra as emitted during the bombardment with 25 MeV/amu neon, nitrogen and proton beams. The satellite structure is more pronounced as the projectile's nuclear charge is increased [a) $K\alpha_1$ and b) $K\beta_{1,3}$].*

Table 5.1a

Spectator	Energy shifts *in eV*			
	$K\alpha_1$	$K\alpha_2$	$K\beta_1$	$K\beta_3$
	0.0	0.0	0.0	0.0
L_I	77.1	71.8	153.9	151.1
L_{II}	100.3	77.7	206.7	208.3
L_{III}	73.3	71.6	180.9	175.8
M_I	9.2	8.6	31.1	30.1
M_{II}	12.6	16.5	33.2	27.4
M_{III}	11.4	8.5	26.5	26.9
M_{IV}	-1.3	1.8	19.8	24.0
M_V	0.4	-2.0	21.4	16.6
N_I	0.64		2.67	2.53
N_{II}	2.40		3.46	4.62
N_{III}	2.13		3.21	2.45
N_{IV}	-0.40		0.16	0.22
N_V	-0.12		0.11	-0.15

Table 5.1b

Spectator	Energy shifts *in eV*			
	$K\alpha_1$	$K\alpha_2$	$K\beta_1$	$K\beta_3$
	0.0	0.0	0.0	0.0
L_I	119.7	105.8	228.0	221.0
L_{II}	163.6	121.2	312.9	312.4
L_{III}	102.5	94.0	248.6	238.5
M_I	18.2	16.2	52.4	49.8
M_{II}	25.7	30.0	59.0	49.6
M_{III}	19.7	14.4	43.2	42.8
M_{IV}	1.4	4.7	35.0	39.5
M_V	3.5	-0.5	35.5	27.8

Table 5.1c

Spectator	Energy shifts *in eV*			
	$K\alpha_i$	$K\alpha_2$	$K\beta_1$	$K\beta_3$
	0.0	0.0	0.0	0.0
L_I	194.0	157.2	345.8	327.5
L_{II}	286.4	196.4	494.4	485.6
L_{III}	139.2	114.4	332.1	310.6
M_I	32.4	26.8	83.4	76.8
M_{II}	49.2	52.2	100.4	83.3
M_{III}	29.2	19.6	62.1	58.9
M_{IV}	2.9	5.3	50.9	53.9
M_V	4.6	-1.1	48.2	34.9

Table 5.1: *Energy shifts in eV, relative to the diagram lines due to the presence of a spectator hole, for the lanthanum , tantalum, uranium atom.*

the initial and final atomic configurations were computed separately, to allow for complete relaxation.

The energy shifts of the $K\alpha_1$ satellite lines due to the presence of one L_I, L_{II}, L_{III}, or M_I spectator hole) relative to the $K\alpha_1$ diagram line, as a function of the target atomic number Z, are shown in Fig. 5.3a. In the same figure the natural widths of the $K\alpha_1$ transitions have been plotted. In a good approximation the width increases with charge Z, as $\sim Z^4$ [Ag79 p.215]. As can be seen from this plot the study of the K X-ray satellites has to face some inherent limitations.

Firstly the natural widths of the $K\alpha_1$ X-ray lines are larger than the energy differences of the M components, and even a measurement with the resolution of the natural line width cannot improve upon this point. The other limitation arises because the relative differences between satellites transitions due to spectator hole

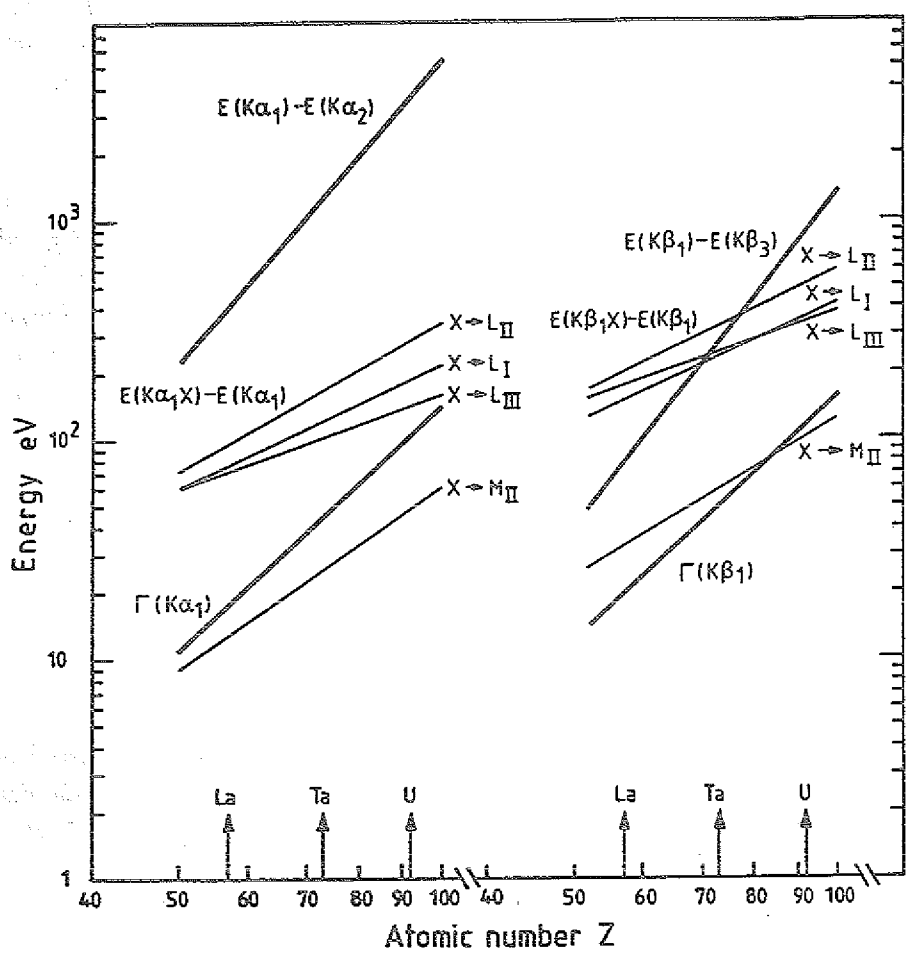

Figure 5.3: *a) Energy shift of the $K\alpha_1$ satellite lines due to the presence of one spectator hole in the X-subshell ($X = L_I$, L_{II}, L_{III}, or M_I) from the diagram line, as a function of the atomic number Z. Also the $K\alpha_1$ natural widths and the $K\alpha$s fine structure energy splitting ($E_{K\alpha_1} - E_{K\alpha_2}$) are shown. b) The same for the $K\beta_1$ transition.*

in different L subshells are comparable to the natural widths. In addition the spectrometer resolution tends to further smear out the spectra.

Consequently in order to study the satellite structure, due to the presence of a L spectator hole, high resolution is requested. The L satellite structure study is expected to be more clear in the lanthanum system, as the ratio of the energy shift of L satellite lines from the diagram line to the line natural width is the largest in comparison with the other two targets (see slopes of the lines $E(K\alpha_1X) - E(K\alpha_1)$ and $\Gamma(K\alpha_1)$ in Fig. 5.3a).

For the elements under investigation the $K\alpha$ fine structure energy splitting is larger than the energy shifts of $K\alpha_2$ satellite transitions in the presence of a L spectator hole, which are in the same order as the energy shifts of $K\alpha_1$ satellite transitions (see Fig. 5.3). This permits the study of $K\alpha_1$ complex satellite structure without the influence of the $K\alpha_2$ spectrum and vice versa (see Fig. 5.1a).

In Fig. 5.3b we show the satellite structure of the $K\beta_{1,3}$ lines. Here the satellites due to a L spectator hole are displaced from the diagram lines more than in the case of the $K\alpha$. Therefore, in principle, the study of the $K\beta_{1,3}$ satellite structure yields additional information about transitions in the presence of M spectator holes, at least for the lighter Z elements.

But the situation is somewhat obscured by another problem. The fine structure splitting of the $K\beta_{1,3}$ transitions ($E(K\beta_1) - E(K\beta_3)$) and the energy shifts of $K\beta_3$ satellites in the presence of L spectator hole, are of the same order (for Z=70.) In the case of Ta the L satellite structure of the $K\beta_3$ is in the same energy region as the $K\beta_1$ diagram transition, but in the case of La the L satellite structure of both $K\beta$s is to the right side of the their diagram transitions, and in U there is no overlap between the one L spectator $K\beta_3$ transitions and the $K\beta_1$ transitions (Fig. 5.3b).

Consequently the spectra of the $K\beta$s are expected to be more sensitive to the presence of L and M spectator holes, but due to the smaller fine structure energy splitting they are more complex.

5.2 Intensities of the satellite lines

For the interpretation of the experimental spectra, the measured X-ray intensities have to be converted and compared with the theoretical predicted hole configuration cross sections. The transformation can be expressed by the product :

$$I_j \propto \sigma_j^{eff} \cdot \omega_j^{tot} \cdot \omega_j^{partial} \tag{5.1}$$

where I_j is the intensity of the emitted X-rays from the j hole configuration atomic state, σ_j^{eff} is the actual hole configuration cross section which takes into account that the K X-ray satellite spectrum reflects the status of the electron shells at the time of the emission of the K photon, and not at the time of production (σ_j^{ini}), and ω_j^{tot} and $\omega_j^{partial}$ are the total and partial fluorescence yields, respectively. In

the following we discuss these contributions:

* The rearrangement of holes in the L and higher shells, which occurs during the lifetime of the K hole is caused by radiative, Auger and Coster – Kronig processes. The conversion from the initial configuration cross sections σ_j^{ini} to the actual configuration cross section σ_j^{eff} is given by:

$$\begin{pmatrix} \sigma_K^{eff} \\ \sigma_{L_I}^{eff} \\ \sigma_{L_{II}}^{eff} \\ \sigma_{L_{III}}^{eff} \end{pmatrix} = \begin{pmatrix} 1 & \frac{\Gamma_{L_I}}{\Gamma_{L_I}+\Gamma_K}(\omega_{L_I}+a_{L_I}) & \frac{\Gamma_{L_{II}}}{\Gamma_{L_{II}}+\Gamma_K}(\omega_{L_{II}}+a_{L_{II}}) & \frac{\Gamma_{L_{III}}}{\Gamma_{L_{III}}+\Gamma_K} \\ 0 & \frac{\Gamma_K}{\Gamma_{L_I}+\Gamma_K} & 0 & 0 \\ 0 & \frac{\Gamma_{L_I}}{\Gamma_{L_I}+\Gamma_K} f_{L_I \to L_{II} X} & \frac{\Gamma_{L_K}}{\Gamma_{L_{II}}+\Gamma_K} & 0 \\ 0 & \frac{\Gamma_{L_I}}{\Gamma_{L_I}+\Gamma_K} f_{L_I \to L_{III} X} & \frac{\Gamma_{L_{II}}}{\Gamma_{L_{II}}+\Gamma_K} f_{L_{II} \to L_{III} X} & \frac{\Gamma_{L_K}}{\Gamma_{L_{III}}+\Gamma_K} \end{pmatrix} \cdot \begin{pmatrix} \sigma_K^{ini} \\ \sigma_{L_I}^{ini} \\ \sigma_{L_{II}}^{ini} \\ \sigma_{L_{III}}^{ini} \end{pmatrix} \quad (5.2)$$

where Γ denotes the level widths of K and L subshells, and ω,a, and f are the L subshell fluorescence, Auger and Coster – Kronig yields, respectively (for Coster – Kronig transitions X denotes any allowed final state).

The diagonal elements of (5.2) give the probability that the K transition will take place before the corresponding initial configuration changes. The non – diagonal elements account for the change of the initial configuration, as it changes in the course of time to the final configuration. For the initial configurations with an L spectator hole we assume that, if the L hole decays through a radiative or Auger process prior to the K X – ray transition, this hole jumps to M or higher shells. These contributions are included in the diagram line, because the energy shifts attributed to M or higher shell spectator holes are less than the natural line width of the diagram line. For the same reason we have not taken into account the rearrangement of M or higher shell spectator holes. If there is a M hole in the initial configuration it may decay prior to the K X – ray transition or it may stay in the same shell through Coster – Kronig and Super Coster – Kronig transitions or it may escape to higher shells through radiative and Auger transitions. In any case, however, it cannot be distinguished experimentally from the diagram line. The de – excitation channels in the case of an L_I hole in the atom of lanthanum are shown in Fig. 5.4.

Using the values for the K and L level widths and the L deexcitation yields for singly ionized atoms as they given by [Kr79a,b] the above matrix equation in the case of lanthanum reads:

$$\begin{pmatrix} \sigma_K^{eff} \\ \sigma_{L_I}^{eff} \\ \sigma_{L_{II}}^{eff} \\ \sigma_{L_{III}}^{eff} \end{pmatrix} = \begin{pmatrix} 1.00 & 0.12 & 0.18 & 0.19 \\ 0.00 & 0.78 & 0.00 & 0.00 \\ 0.00 & 0.04 & 0.79 & 0.00 \\ 0.00 & 0.06 & 0.03 & 0.81 \end{pmatrix} \cdot \begin{pmatrix} \sigma_K^{ini} \\ \sigma_{L_I}^{ini} \\ \sigma_{L_{II}}^{ini} \\ \sigma_{L_{III}}^{ini} \end{pmatrix} \quad (5.3)$$

in the case of tantalum :

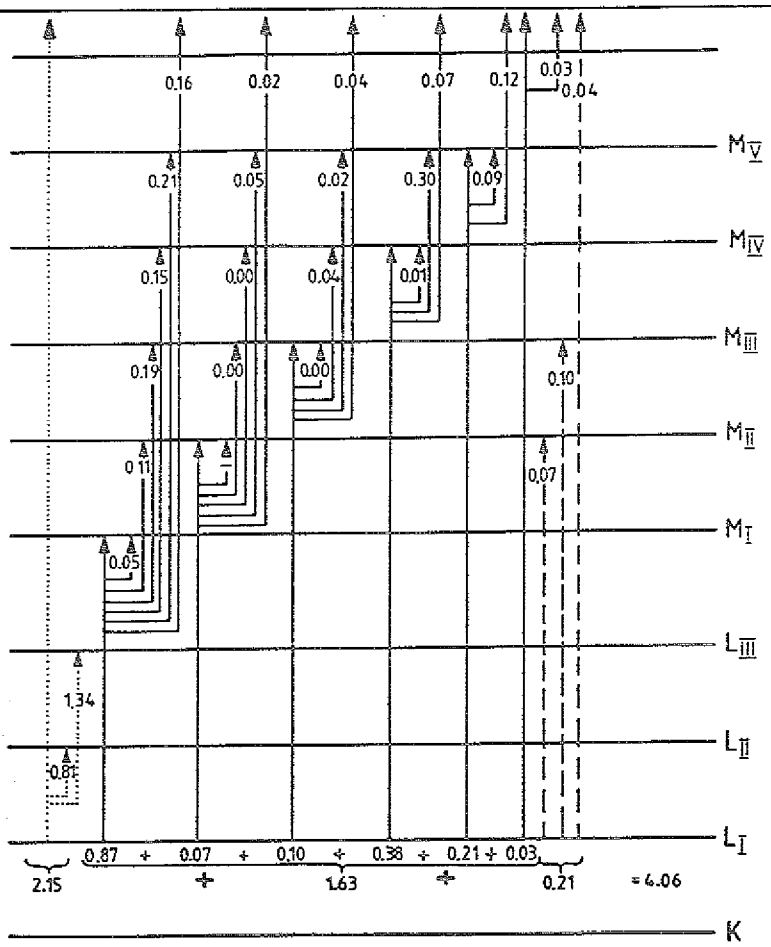

Figure 5.4: *Radiative (- - -), Auger(—), and Coster- Kronig(....) de-excitation channels for an* L_I *hole, in the atom of lanthanum. The corresponding partial widths are given in eV.*

$$\begin{pmatrix} \sigma_K^{eff} \\ \sigma_{L_I}^{eff} \\ \sigma_{L_{II}}^{eff} \\ \sigma_{L_{III}}^{eff} \end{pmatrix} = \begin{pmatrix} 1.00 & 0.07 & 0.10 & 0.11 \\ 0.00 & 0.87 & 0.00 & 0.00 \\ 0.00 & 0.02 & 0.88 & 0.00 \\ 0.00 & 0.04 & 0.02 & 0.89 \end{pmatrix} \cdot \begin{pmatrix} \sigma_K^{ini} \\ \sigma_{L_I}^{ini} \\ \sigma_{L_{II}}^{ini} \\ \sigma_{L_{III}}^{ini} \end{pmatrix} \tag{5.4}$$

and in the case of uranium :

$$\begin{pmatrix} \sigma_K^{eff} \\ \sigma_{L_I}^{eff} \\ \sigma_{L_{II}}^{eff} \\ \sigma_{L_{III}}^{eff} \end{pmatrix} = \begin{pmatrix} 1.00 & 0.04 & 0.07 & 0.07 \\ 0.00 & 0.87 & 0.00 & 0.00 \\ 0.00 & 0.01 & 0.91 & 0.00 \\ 0.00 & 0.07 & 0.02 & 0.93 \end{pmatrix} \cdot \begin{pmatrix} \sigma_K^{ini} \\ \sigma_{L_I}^{ini} \\ \sigma_{L_{II}}^{ini} \\ \sigma_{L_{III}}^{ini} \end{pmatrix} \tag{5.5}$$

Comparing the diagonal elements of these matrices, it is obvious that for the heavier elements the actual configuration cross sections σ_j^{eff} and the initial cross sections σ_j^{ini} differ less than in the case of lighter elements. In other words the

measured X-ray spectra of the heavy elements reflect more closely the initial state created by the projectile, than in the light elements.

The relative error of the diagonal elements is given by :

$$\sigma_R = \frac{\Gamma_L}{\Gamma_K + \Gamma_L} \cdot \sqrt{\sigma_R^2(\Gamma_K) + \sigma_R^2(\Gamma_L)} \tag{5.6}$$

where Γ_K and Γ_L are the natural widths of the K and L levels respectively, and $\sigma_R(\Gamma_K)$ and $\sigma_R(\Gamma_L)$ the estimated relative uncertainties of the K and L levels, respectively.

Using the semi-empirical values of natural widths given by [Kr79] and the estimated uncertainties, the relative error in the diagonal elements of the above matrix, is given in the following Table 5.2:

Target	Relative error σ_R (%)		
	(2,2)	(3,3)	(4,4)
Lanthanum	4.6	2.2	2.1
Tantalum	2.0	1.3	1.0
Uranium	2.6	1.0	0.6

Table 5.2: *Relative error in the determination of the (n,n) diagonal elements of the matrix equations (5.3-5.5)*

In all the cases the relative error, due to the uncertainty of the used values of the natural widths is less than 5%.

Another probably more significant uncertainty is the fact that the used level widths have been obtained for singly ionized atoms. And it is not kwown how much the level widths can change in the presence of spectator holes. Supposing that this uncertainty is in the order of 20% for both K and L level widths, in the case of an L spectator hole in lanthanum the relative error of the diagonal matrix elements is in the order of 5%. For the other targets is still smaller. This is one of the great advantages of the study of L ionization probabilities by measuring the K X-rays spectra and using heavy elements as targets. As the K level widths are much larger than than the L level widths, it can be seen from Eq. (5.6) that the relative error for the diagonal elements of the above matrices becomes small.

In order to have an estimation of the change of the level widths in the presence of an L spectator hole, we have calculated the K level width of lanthanum in the presence of an L spectator hole (see for the details Appendix B). In the presence of an L_I spectator hole the natural width of the K level stays unchanged, but in the case of L_{II} and L_{III} spectator hole it is reduced by 10% and 13%, respectively. As the uncertainty in the K level width is estimated to be 4% for La, the main difficulty for the determination of the level widths is the lack of predictions in the case of spectator holes.

* The total K fluorescence yield ω_j^{tot} for each K multiply ionized configuration, which corresponds to the probability for the emission of a K X-ray.

For a singly K ionized lanthanum, tantalum and uranium atom the total K fluorecense yield is 0.906, 0.956, and 0.976, respectively [Le78].

One of the most severe problems, for the proper interpretetion of the experiments is how much the total K fluorescence yield can change in the presence of an L spectator hole.

After detailed calculations we found that in the case of the lanthanum the total K fluorescence does not change more than 3% (see for the details Appendix B). Therefore we neglect the influence of spectator holes on the total K total fluorescence yield, also for the heavier elements.

* The partial K fluorescence yield $\omega_j^{partial}$ which gives the probability that the K X-ray belongs to a specific K transition.

Another question which has to be answered is how much the partial K fluorescence yield can change in the presence of an L spectator hole.

For a singly K ionized lanthanum atom the partial K fluorescence yields are given by [Le78]. We have calculated the partial K fluorecense yields in the presence of a spectator hole in the different L subshells, using the MCDF code [De75]. As can be seen in Fig. 5.5 the partial yields may change considerably in the presence of one L spectator hole [see Appendix B].

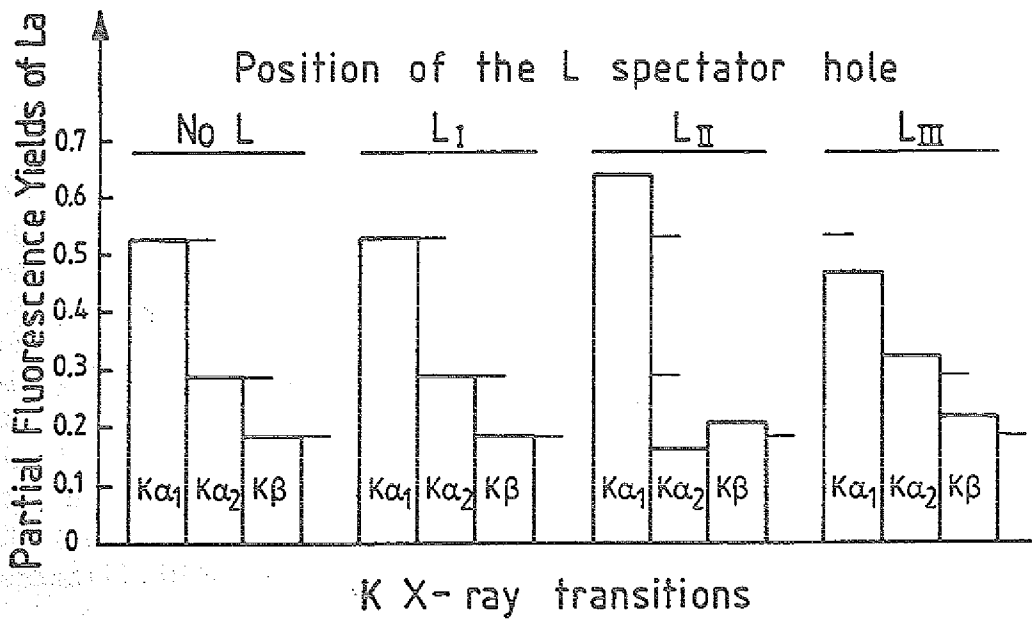

Figure 5.5: *Partial K fluorescence yields of lanthanum in the presence of one L spectator hole in the L subshells, in comparison with the partial fluorescence yields of the K diagram transitions (no spectator hole).*

It has been demonstrated that the partial yields can be reproduced with very good accuracy by a simple semiemperical formula [see Appendix B]. As a typical

example, the Kα_1 partial fluorescence yield, in the case of a spectator hole in the L_x subshell can be written as :

$$\omega_{K\alpha_1}(L_x) = \frac{\omega_{K\alpha_1}(1 - \frac{n_{L_{III}}}{4})}{\omega_{K\alpha_1}(1 - \frac{n_{L_{III}}}{4}) + \omega_{K\alpha_2}(1 - \frac{n_{L_{II}}}{2}) + \omega_{K\beta_1} + \omega_{K\beta_3} + \omega_{K\beta}} \tag{5.7}$$

where $\omega_{K\alpha_1}$, $\omega_{K\alpha_2}$, $\omega_{K\beta_1}$, $\omega_{K\beta_3}$, and $\omega_{K\beta}$ are the partial fluorescence yields for a singly K ionized atom, $n_{L_{III}}$ and $n_{L_{II}}$ are the number of spectator holes in the corresponding subshells (see Appendix B).

5.3 Ionization Probabilities and Cross Sections

The dominant ionization mechanism during heavy ion – atom colission is usually classified by the asymmetry parameter (Z_1/Z_2) and the adiabaticity parameter n of the colliding system (see page 15). The above parameters for the K and L shell target electrons of the four colliding systems have to be calculated. For doing so we need the projectiles' and atomic electrons' orbital velocities.

The electronic configuration of lanthanum, tantalum, and uranium target atoms is given as :

La (Z=57) : [Xe] $5d^1 6s^2$
Ta (Z=73) : [Xe] $4f^{14} 5d^3 6s^2$
U (Z=92) : [Xe] $4f^{14} 5d^{10} 6s^2 6p^6 5f^3 6d^1 7s^2$
where [Xe] : $1s^2 2s^2 2p^6 3s^2 3p^6 3d^{10} 4s^2 4p^6 4d^{10} 5s^2 5p^6$.

The binding energies of the electrons in the atomic shells of the above atoms [Le78] are listed in Tables 5.3. From the binding energies E_{bind} the kinetic energies of the atomic electrons E_{kin} can be obtained using the virial theorem [for example see Br83, p. 147] ; $E_{kin} = |E_{bind}|$.

The electron velocities u_2 have been calculated from E_{kin} by:

$$u_2 = \sqrt{1 - (1 + \frac{E_{kin}}{m\,c^2})}\; c \tag{5.8}$$

where mc^2 is the electron rest mass and c the velocity of light.
They are given in Tables 5.3 as well as the radii of the (sub)shells calculated using the multiconfiguration Dirac – Fock code of [De75].

The projectile velocity u_1 is given by :

$$u_1 = \sqrt{\frac{2E_{kin}}{M_1}} \tag{5.9}$$

where M_1 is the projectile mass. From this relation the projectile velocity u_1 can be calculated as:

$$u_1 = 46.3 \cdot 10^{-3} \sqrt{A_{kin}}\; c \tag{5.10}$$

Table 5.3a

Shell	E_{Bind} *in KeV*	Velocity *in c*	Radius *in fermi*
K	38.925	0.370	1328.
L_I	6.267	0.155	5609.
L_{II}	5.891	0.151	4763.
L_{III}	5.483	0.146	5080.
M_I	1.362	0.074	14976.
M_{II}	1.205	0.070	14499.
M_{III}	1.124	0.067	15134.
M_{IV}	0.852	0.059	13600.
M_V	0.835	0.059	13811.

Table 5.3b

Shell	E_{Bind} *in KeV*	Velocity *in c*	Radius *in fermi*
K	67.413	0.469	988.
L_I	11.680	0.210	4143.
L_{II}	11.136	0.205	3437.
L_{III}	9.881	0.194	3850.
M_I	2.705	0.102	10786.
M_{II}	2.466	0.098	10272.
M_{III}	2.191	0.092	11032.
M_{IV}	1.790	0.083	9683.
M_V	1.732	0.082	9919.

Table 5.3c

Shell	E_{Bind} *in KeV*	Velocity *in c*	Radius *in fermi*
K	115.610	0.579	723.
L_I	21.758	0.283	2991.
L_{II}	20.948	0.278	2425.
L_{III}	17.168	0.253	2965.
M_I	5.548	0.146	7781.
M_{II}	5.181	0.141	7318.
M_{III}	4.304	0.129	8284.
M_{IV}	3.728	0.120	7155.
M_V	3.552	0.117	7441.

Table 5.3: *Electrons binding energies, orbital velocities and mean shell radii, for the lanthanum atom (Table 5.3a), for tantalum (Table 5.3b) and uranium (Table 5.3c).*

where A_{kin} is the kinetic energy in MeV/nucleon. The results are listed in Table 5.4.

Projectile	E_{kin} *in MeV*	A_{kin} *in MeV/amu*	u_1 *in c*
^{14}N	405	29	0.25
^{14}N	350	25	0.23
^{20}Ne	500	25	0.23

Table 5.4: *Projectile's kinetic energy Ekin in MeV, kinetic energy Akin in MeV/amu, and its velocity in light velocity units.*

The values of the asymmetry and adiabaticity parameter are given in Table 5.5. The adiabaticity parameter n_K for the K shell is considerably smaller than unity and therefore the use of the separated – atom approach for this shell might be questioned (see Fig. 2.1). However, the systems are still near to the region of non – adiabaticity. Consequently, the united atom theory is expected to overestimate the molecular effects [Am91]. In addition, according to Eq. (2.30), the K X – ray satellite intensity due to the L spectator relative to the diagram line, is independent of the K – shell electron ionization probabilities, as $P_L(b)$ is slowly varying (see Fig. 2.3).

Colliding system	Z_1/Z_2	n_K	n_{L_I}	$n_{L_{II}}$	$n_{L_{III}}$
403 MeV N^{7+} → La	0.12	0.46	2.60	2.74	2.93
350 MeV N^{7+} → Ta	0.10	0.24	1.20	1.26	1.41
500 MeV Ne^{10+} → U	0.11	0.16	0.66	0.68	0.83

Table 5.5: *The asymmetry parameter Z_1/Z_2 and the adiabaticity parameter $n_i[n = (u_1/u_2)^2]$ for the three systems, for the K and L shell target electrons.*

The adiabaticity parameter for the L shell n_L decreases monotonically as the target charge increases (because the projectile velocities are almost constant but the target electron velocities increase with the Z_{targ}). The direct Coulomb interaction is expected to be the prominant ionization mechanism for the L shell target electrons. If there are any deviations from the separated atom approximation, they have to be more pronounced when decreasing the adiabaticity parameter n_L, as the interaction time between projectile and L shell electrons is increased. Consequently, a possible discrepancy between theory and experiment, due to the validity of the direct ionization assumption, is expected to show up in the 500 MeV Ne^{10+} → U system, but not in the case of 403 MeV N^{7+} → La.

5.3.1 One electron direct ionization probabilities

According to the discussion above the most proper choice is the use of the separated atom approximation. The impact parameter dependent ionization probabilities have been calculated in the framework of semi-classical separated atom perturbation theory (SCA, impact parameter method).

Two models predicting the ionization probabilities in the separated atom approximation are discussed, which differ essentially in the used potentials (wave functions). In the case of 403 MeV $N^{7+} \rightarrow$ La the tabulated values from Hansteen et al. [Ha75] are also taken into consideration.

Model I uses a variationally determined optimized potential [Aa78] in order to take into account the precence of the passive target electrons. This potential gives wave functions which have been found to be very similar to relativistic Hartree-Fock wave functions [Aa78]. The projectile follows a straight line path as trajectory. This approximation is justified as in all the considered systems the projectile's deflection is some tenths of the degree, for impact parameters above 100 fm. For the K shell the multipole transitions from l=0 to l=4 have been included, for L_I shell up to l=5, and for L_{II} and L_{III} up to l=6. The binding energies, have been calculated with the MCDF program of [De75] under the condition of one vacancy present in the K shell.

The complete set of single electron ionization probabilities $P_i(b)$, for the K, L, and M shell as function of the impact parameter b, as calculated by [Am91] according to Model I, are given in Appendix E (see also Fig. 5.6).

Model II uses screened relativistic hydrogenic electron wave functions and the projectile is assumed to move along a hyperbolic Coulomb-trajectory [Tr80]. The target recoil is taken into account but its contribution is significant only at zero impact parameter. For the K and L shell multipole transitions from l=0 to l=4 have been included. The used binding energies are those listed in Table 5.3. The ionization probabilities $P_i(b)$, as calculated using model II, for removing one arbitrary electron from K, L, or M (sub)shell are given in Appendix E (see also Fig. 5.6).

Colliding system	Model I		Model II	
	P_L^I	P_M^I	P_L^{II}	P_M^{II}
403 MeV $N^{7+} \rightarrow$ La	0.037	0.041	0.021	0.011
350 MeV $N^{7+} \rightarrow$ Ta	0.030	0.043	0.021	
500 MeV $Ne^{10+} \rightarrow$ U	0.037	0.070	0.032	

Table 5.6: *Mean L and M electron direct ionization probabilities P, for the three colliding systems according to Model I and Model II.*

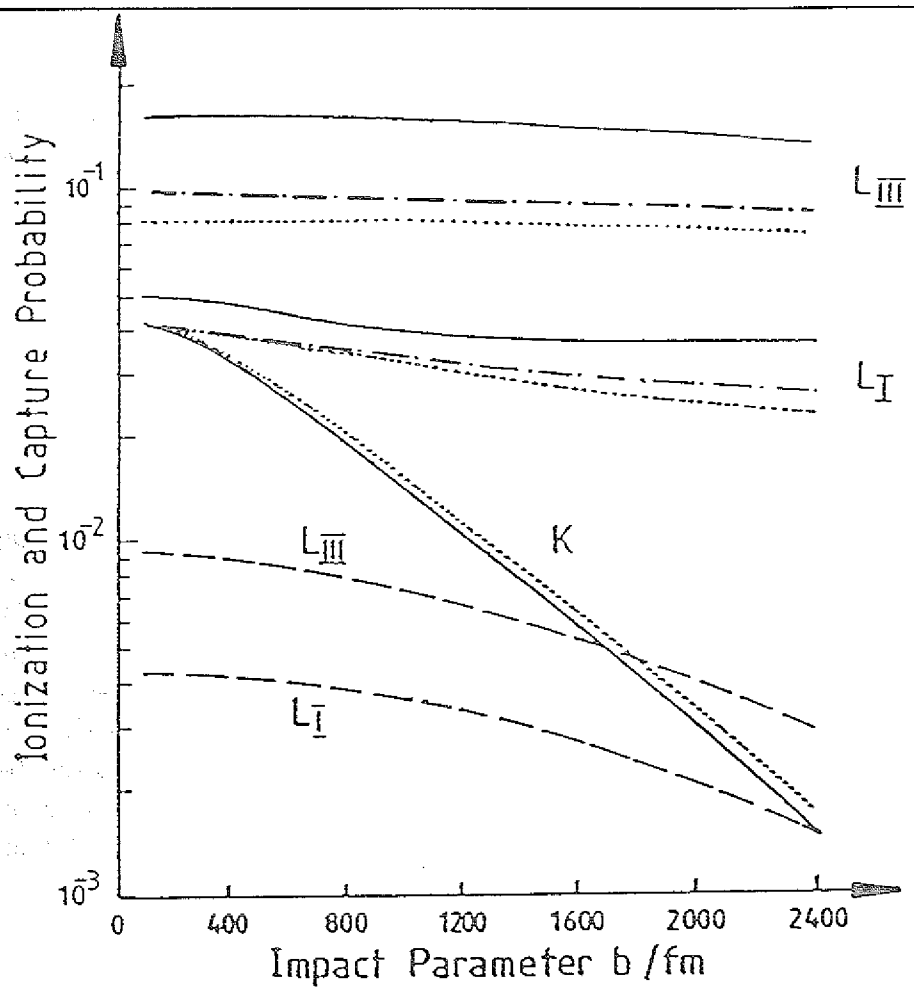

Figure 5.6: *Direct ionization probabilities for creation of a vacancy in the the K,* L_I *and* L_{III} *subshells for 403 MeV* $N^{7+} \rightarrow$ La, *as a function of the impact parameter b: full lines for Model I, dotted lines for Model II and chained lines for predictions from Hansteen et al. [Ha75]. In a good approximation the* L_{II} *probabilities are a factor 2 less than the* L_{III} *probabilities. There is a quite good agreement for the K shell ionization probabilities, but for ionization probabilities of the L shell electrons they disagree significantly. The dashed lines are the probabilities for capture of an L shell target electron by the projectile according to SPB [Ja84].*

In the case of 403 MeV $N^{7+} \rightarrow$ La, the tabulated L ionization probabilities from Hansteen et al. [Ha75] are compared with the predictions of the two models. As the these ionization probabilities have been calculated using a hydrogenic potential (wave functions) their values are close to the predictions of model II (see Fig. 5.6).

For comparison of Model I and Model II the mean values of the direct L and M electron ionization probabilities, for the three colliding systems are given in Table 5.6.

Coupled-channels corrections

In order to test the accuracy of a first-order separated-atom perturbation theory in the case of L subshell ionization, a close-coupling between the L subshells has been taken into account. Only the transition to the continuum has been treated in a perturbative way [Ja91]. Due to the small energy spacing between the subshells such a coupling can be important for L subshells.

In this approach, the transition amplitude a_{fi} entering in $P_i(b)$ is the solution of a system of coupled differential equations :

$$\dot{a}_{fn} = -\imath a_{fn} E_n - \imath \sum_k a_{fk} < \psi_n | V_P | \psi_k > -\imath < \psi_n | V_P | \psi_f > \exp(-\imath E_f t) \quad (5.11)$$

which has to be solved under the initial condition $a_{fn}(t = -\infty) = 0$. The indices n and k extend over all eight L sub-shell states because the magnetic quantum numbers $+m_n$ and $-m_n$ have to be considered explicitly. In these calculations, hydrogenic wavefunctions have been used with an effective charge, determined from the mean value of the inverse shell radius $< r^{-1} >$. This shell radius together with the binding energy has been calculated with the program of Desclaux under the condition of one vacancy present in the K shell. In order to account for the defficiency of the coupled-channel calculations with respect to the use of poorer wavefunctions and with a poorer numerical accuracy as compared with the SCA calculations, the coupled-channel calculations have been scaled by a correction factor. This correction factor is given by the ratio between the SCA results and the corresponding perturbative results which are obtained by solving the coupled differential equations with the bound-bound matrix elements set equal to zero (a method formally indentical to SCA).

The inclusion of the L subshell coupling modifies the subshell ionization probabilities $P_i(b)$, as obtained using the SCA, by a correction factor $C_i(b)$. The subshell ionization probabilities $P_i^c(b)$ using the coupled-channel theory is given by :

$$P_i^c(b) = C_i(b) \cdot P_i(b) \quad (5.12)$$

The correction factors $C_i(b)$ for the three L subshells, as calculated by [Ja91] as function of the impact parameter b are given in Appendix E. In the following Table 5.7 the mean L subshell coupling correction factor C_i for the three systems are given.

The largest contribution of the subshell coupling is in the case of 500 MeV $Ne^{+10} \rightarrow U$. This is mainly due to the fact that the projectile moves with a speed less than the L shell electrons of U (see Table 5.5) and therefore binding effects become pronounced. The molecular effects of the L subshells (deviations from the separated-atom approximation) are mostly accounted for by the subshell coupling [Ja91].

Colliding system	C_{L_I}	$C_{L_{II}}$	$C_{L_{III}}$
403 MeV N^{7+} → La	1.01	0.95	0.95
350 MeV N^{7+} → Ta	0.92	0.86	0.88
500 MeV Ne^{10+} → U	0.77	0.67	0.73

Table 5.7: *Mean L subshell coupling correction factors C_i for the L ionization probabilities [Ja91] calculated in first-order.*

The coupling of M subshells have not been taken into account. Due to the large velocity ratio between the velocities of projectile and M shell electrons the coupling strength is reduced and so the effect is expected to be smaller.

5.3.2 One electron capture ionization probabilities

During the passage of the bare projectile through the target, the projectile has the chance to capture electrons from the target atoms into its open shells.

The capture probabilities from the L subshells of the target to the K shell of the projectile as function of the impact parameter b have been calculated using the nonrelativistic strong potential Born approximation (SBP) [Ja91]. The absolute capture probabilities for L target electron as function of the impact parameter b as calculated by [Ja91], are given in Appendix E (see also Fig. 5.6).

The capture probabilities for the different projectile shells scale like n^{-3}, where n is the main quantum number of the shell. This means that the main capture occurs to the K shell of the projectile. The mean capture probabilities from L (target) → K(projectile) can be scaled by the factor 1.2 (as $\sum_{n=1}^{\infty} n^{-3} \rightarrow 1.2$) to estimate the mean capture probabilities of an electron from the L target shell to any shell of the projectile. The mean capture probabilities from the L shell of the target to the shells of the projectile are given in Table 5.8.

Colliding System	$P_L^{capture}$
403 MeV N^{7+} → La	0.0021
350 MeV N^{7+} → Ta	0.0018
500 MeV Ne^{10+} → U	0.0044

Table 5.8: *Mean capture probabilities from the L shell of the target to the shells of the projectile.*

Comparison with the mean direct ionization probabilities (see Table 5.6) shows that the capture probabilities are in most cases one order of magnitude

smaller.

5.3.3 Multiple ionization cross-sections

The ionization cross sections for multiple vacancy production have been computed on the basis of the independent particle model.

Using the ionization probability P_i for removing one arbitrary electron from subshell i, which consists of n_i electrons, and m_i being the number of produced vacancies in this subshell, the cross section σ_j^{ini} for this multiply ionized configuration j can be expressed as:

$$\sigma_j^{ini} = 2\pi \int_0^\infty b\,db \prod_i \binom{n_i}{m_i} \left(\frac{P_i(b)}{n_i}\right)^{m_i} \left(1 - \frac{P_i(b)}{n_i}\right)^{n_i - m_i} \tag{5.13}$$

where i runs over all the subshells, which are considered explicitly.

For all other (sub)shells which are taken into account implicitly, we use a binomial distribution to sum over all possible combinations:

$$\sum_{m_i=0}^{n_i} \binom{n_i}{m_i} \left(\frac{P_i(b)}{n_i}\right)^{m_i} \left(1 - \frac{P_i(b)}{n_i}\right)^{n_i - m_i} = 1 \tag{5.14}$$

This means that the cross section σ_j^{ini} for a defined configuration is 'inlusive' with respect to these subshells.

As can be seen from Figs. (2.3), (5.7) and the tables in Appendix E, the ionization probabilities P_K exhibits a steep decrease with increasing impact parameter b, whereas the ionization probabilities of L and M shells show a smooth behaviour. Therefore we have performed the integration for σ_j^{ini} to an upper bound of the impact parameter in which the K ionization probability has dropped at least by one order of magnitude.

The calculated total cross sections σ_K for the K electron ionization of the three systems, are listed in Table 5.9 for the Model I and II respectively. These cross sections are 'inclusive' with respect to the (sub)shells higher than M, which means that they are independent of what is happing in the outer shells.

For all the colliding systems the theoretical predictions for the total cross section σ_K of the two models are in good agreement.

In Table 5.10 we give the ratio $\sigma_{KL^1}/\sigma_{KL^0}$, where σ_{KL^1} denotes the simultaneous creation of one K and one L hole and σ_{KL^0} denotes the cross section with one K and no L hole using Model I and Model II, respectively. Here the predictions of the two models deviate considerably. Model II predicts cross sections for the simultaneous ejection of K and L electrons, which are between 16% and 45% lower than in Model I. The disagreement increases with increasing the adiabacity parameter (see Table 5.5).

Colliding System	σ_K *in barns*		$\frac{\sigma_K(II)-\sigma_K(I)}{\sigma_K(I)}$
	Model I	Model II	
403 MeV N^{+7} → La	1480	1550	4.7%
350 MeV N^{+7} → Ta	277	298	7.6%
500 MeV Ne^{+10} → U	111	117	5.4%

Table 5.9: *K shell electron direct ionization cross section, in the separated atom approximation a) using to Model I and b) using Model II, and their relative difference.*

Colliding system	$R=\sigma_{KL^1}/\sigma_{KL^0}$		$\frac{R(II)-R(I)}{R(I)}$
	Model I	Model II	
403 MeV N^{+7} → La	0.284	0.157	45 %
350 MeV N^{+7} → Ta	0.233	0.159	32 %
500 MeV Ne^{+10} → U	0.301	0.254	16 %

Table 5.10: *Ratio of the cross section for one K and one L hole simultaneously to the cross section for one K and no L hole a) using Model I and b) using Model II, and their relative difference.*

5.4 K X-ray spectra during the bombardement ...

In order to interprete the experimental spectra, we reconstructed the line-shape of the K X-ray satellite spectrum from the calculated X-rays energy positions and intensities.

The shape of a X-ray line with a natural width Γ is described by Lorentzian function :

$$I(E) = \frac{I_0}{1 + 4\left(\frac{E-E_0}{\Gamma}\right)^2} \tag{5.15}$$

where I_0 is the peak intensity and E_0 is the energy at the peak position.

The transition intensities are converted into the line parameters: peak intensity and line width, which we take as the natural width. The intensity A of the line, the peak intensity I_0 and the FWHM of the Lorentzian Γ are connected by :

$$A = \frac{\pi}{2} \cdot \Gamma \cdot I_0 \tag{5.16}$$

The total intensities A of the satellites, are taken relative to the diagram line. The position of each satellite line is fixed by its calculated energy shift.

The response function of the spectrometer, $D_{sp}(E)$, has been assumed to be Gaussian, or square. The line shapes of the measured K X-ray transitions are given by the folding of the two functions:

$$I(E) = \int I(E') \cdot D_{sp}(E - E') \cdot dE' \tag{5.17}$$

The folded line shapes of the satellite transitions, with their energy positions fixed relative to the diagram transition line, are superimposed and the resulting complex is compared to the experimental data by fitting the peak intensity and position of the diagram line.

For the construction of the theoretical spectra and comparison with the experiment all the configurations which involve at least one L shell spectator hole have to be included. The binominal probabilities for no, one, two or three holes in the L shells are given Table 5.11, using the L electron ionization probabilities of Model I.

Taking into account up to 3 L holes amounts more than 99.9% of all the possible number of created L shell holes. Consequently, it is sufficient for the L spectator hole satellite structure, to include satellites lines arising from one, two or three spectator holes in L shells.

In the following Table 5.12 are given the binominal probabilities for the corresponding number of holes in the M shell (up to three M spectator holes) using the M electron ionization probabilities of Model I.

Colliding system	P_{L^0}	P_{L^1}	P_{L^2}	P_{L^3}	$\sum_{i=0}^{3} P_{L^i}$
403 MeV N^{7+} → La	0.74	0.23	0.03	0.00	1.00
350 MeV N^{7+} → Ta	0.78	0.19	0.03	0.00	1.00
500 MeV Ne^{10+} → U	0.74	0.23	0.03	0.00	1.00

Table 5.11: *Binomial probabilities for 0 to 3 holes in L shell.*

Colliding system	P_{M^0}	P_{M^1}	P_{M^2}	P_{M^3}	$\sum_{i=0}^{3} P_{M^i}$
403 MeV N7+ → La	0.47	0.36	0.13	0.03	0.99
350 MeV N7+ → Ta	0.45	0.37	0.14	0.03	0.99
500 MeV Ne10+ → U	0.27	0.37	0.23	0.09	0.96

Table 5.12: *Binomial probabilities for 0 to 3 holes in M shell.*

Finally, in the developed model it was possible to use totally up to three spectator holes distributed in the L and M subshells (totally 160 satellite lines) whereas the satellites from with N,O ... spectator holes are treated as 'inclusive'. The decision whether to treat the M spectator holes as 'exclusive' or as 'inclusive' has to be taken individually for each particular colliding system according to the neccesity and feasibility.

5.4.1 ... of Lanthanum with 403 MeV nitrogen

The average energy shifts of the satellite lines due to one spectator hole in the L, M or N subshell with respect to the $K\alpha_1$, $K\alpha_2$, $K\beta_1$ and $K\beta_3$ diagram lines are given in Table 5.3a.

In the case of La the presence of one M_{IV} or one M_{II} spectator hole shifts the energy of the $K\alpha_1$ transition by −1.3 eV or 12.6 eV respectively, which are smaller than the natural widths of the $K\alpha_1$ line and energy resolution of our experiment (about 30 eV). Therefore it is not possible to resolve transitions which take place in the presence of a M spectator hole, but they are indicated by broadening and asymmetry of the 'diagram' line. The situation is different in the case of a L spectator hole. These energy shifts are 76.4 eV, 100.1 eV and 73.5 eV for one spectator hole in the L_I, L_{II} and L_{III} subshell, respectively, which is larger than the natural line width and energy resolution. Therefore the corresponding satellite lines should be separated from the diagram line and show up as a pronounced bump in this energy region. However the experiment exhibits a plateau – like shoulder that extends to about 120 eV (see Fig. 5.1).

The bump must be even more pronounced in the case of $K\alpha_2$ transition, because the energy shifts for one spectator hole in the L_I, L_{II} and L_{III} subshell are

71.8 eV, 77.7 eV and 71.6 eV, respectively. As can seen from Fig. 5.1 this is not the case.

As starting point for comparison between experiment and theoretical predictions the lanthanum $K\alpha_1$ spectrum has been studied.

In Fig. 5.7a the $K\alpha_1$ spectrum of La is shown and compared with the theoretical predictions for the energy position and the intensity distribution. The used K, L, M direct ionization probabilities are those which have been calculated by model I. The L subshell coupling and capture have been included but boths effects are in the order of 5% and in the opposite direction. Hence their contribution is negligible [1]. We have fitted from the low energy of the $K\alpha_1$ up to $+25$ eV in the high energy side of the diagram line.

The discrepancy between experimental data and the theoretical construction is obvious ($\chi^2 = 7.81$). The structure of the discrepancy suggests that probably the intensity is not properly distributed.

The simple picture as outlined is obscured by a significant physical effect: The

[1] The contribution to the L and M ionization probabilities due to electron shake– up and shake– off processes are expected to be of the order of 10^{-3}to10^{-4} per subshell [Ca73]. In comparison with the direct ionization probabilities this is at least two orders of magnitude smaller, and consequently the contribution of these two processes can be neglected here.

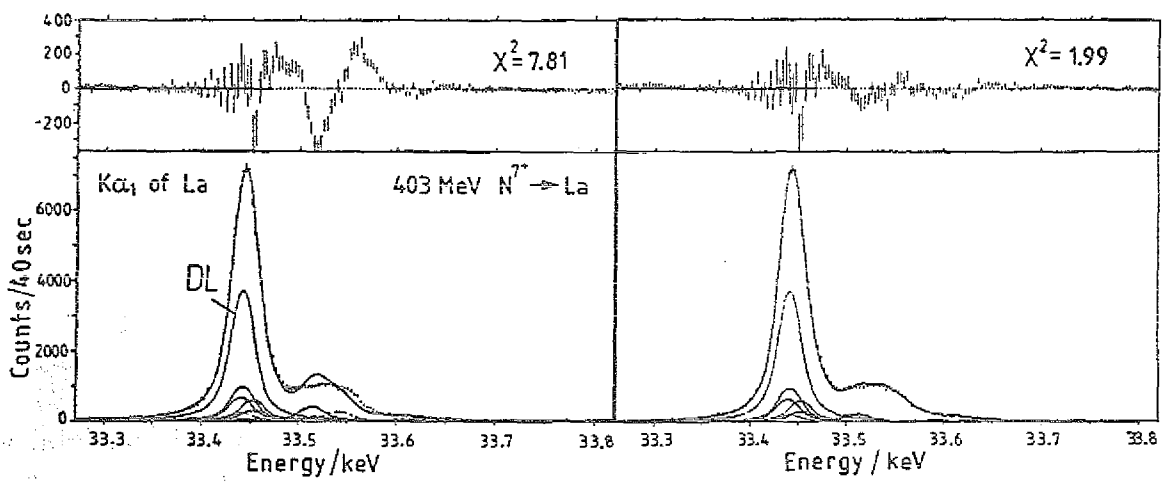

Figure 5.7: *Comparison of the measured (points) first order reflection of the $K\alpha_1$ lanthanum X-rays induced by 403 MeV N^{7+} with the theoretical line shape (full line). On the energy axis are plotted the diagram line (DL) and the strongest satellites. The residues are shown in the upper parts of the figures. a) SCA Coulomb ionization probabilities according to model I used with capture and L subshell coupling but without taking into account the multiplet structure caused by the corresponging L spectator hole. b) The angular momentum coupling between active and one L spectator hole is included*

Table 5.13a

Spectator	Transition		Energy shift *in eV*		Rate $\times 10^{15}\ sec^{-1}$	
	$J_i \rightarrow J_f$		$K\alpha_1$	$K\beta_1$	$K\alpha_1$	$K\beta_1$
	1/2	3/2	0.	0.0	10.23	2.01
L_I	0	1	108.1	217.3	8.69	1.99
L_I	1	1	21.0	130.6	2.30	0.38
L_I	1	2	78.1	134.2	8.64	1.73
L_{II}	0	1	116.2	213.2	11.04	2.08
L_{II}	1	1	109.3	206.5	1.65	0.34
L_{II}	1	2	92.4	204.9	9.56	1.73
L_{III}	1	0	58.8	177.0	3.43	0.35
L_{III}	1	1	—	208.0	—	0.89
L_{III}	1	2	101.0	190.9	8.19	0.80
L_{III}	2	1	—	176.2	—	0.09
L_{III}	2	2	69.1	159.1	5.39	0.56
L_{III}	2	3	—	176.3	—	1.46

Table 5.13b

Spectator	Transition		Energy shift *in eV*		Rate $\times 10^{15}\ sec^{-1}$	
	$J_i \rightarrow J_f$		$K\alpha_2$	$K\beta_3$	$K\alpha_2$	$K\beta_3$
	1/2	3/2	0.	0.0	5.56	0.92
L_I	0	1	125.0	216.3	7.35	1.04
L_I	1	0	70.7	131.1	1.88	0.32
L_I	1	1	37.8	129.6	3.19	0.60
L_{II}	0	1	—	220.5	—	0.96
L_{II}	1	0	75.3	187.6	3.73	0.32
L_{II}	1	1	—	213.8	—	0.64
L_{III}	1	1	101.7	196.5	1.02	0.13
L_{III}	1	2	84.8	195.4	4.26	0.86
L_{III}	2	1	69.8	164.7	2.82	0.49
L_{III}	2	2	52.9	163.6	2.57	0.43

Table 5.13: *Energy shifts of the $K\alpha$ and $K\beta$ satellites relative to the diagram lines and corresponding electric dipole transitions for lanthanum, splitted due to the angular momentum coupling between the 'active' and one L 'spectator' hole. J_i and J_f denotes the total angular momentum of the initial and the final state.*

correct description of particular initial and final atomic states requires a mixing of configurations with a particular angular momentum J. This leads to an energy splitting both for initial and final states, i.e. one single satellite splits into several lines.

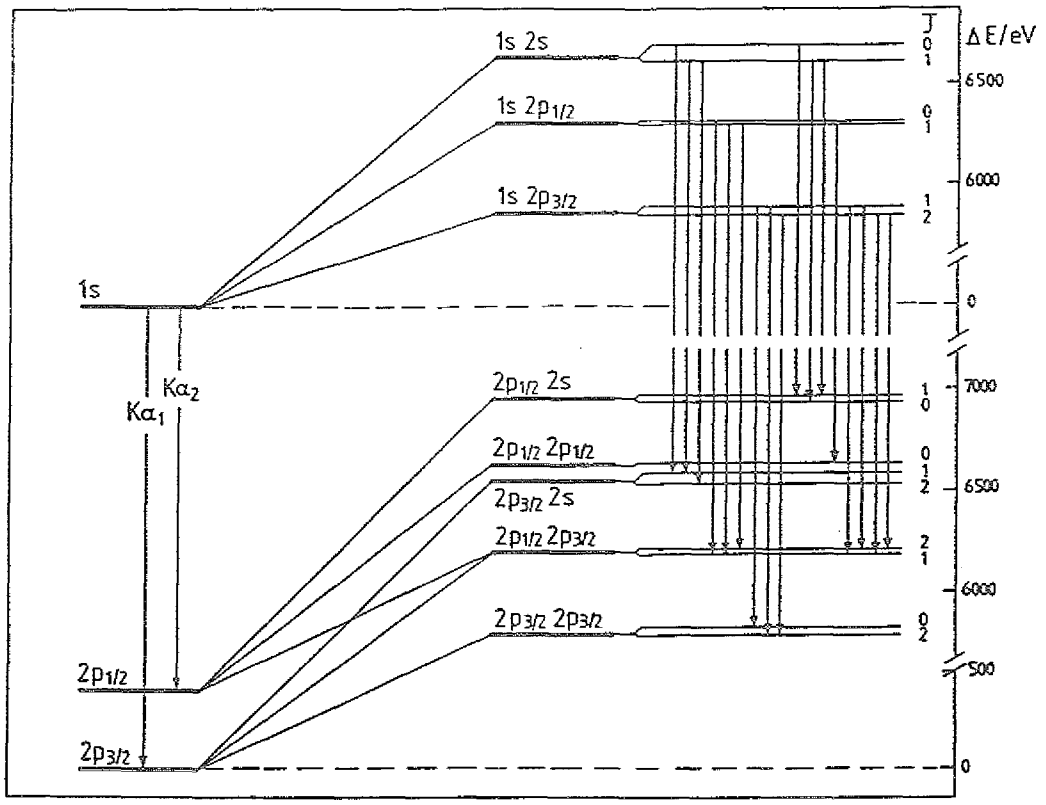

Figure 5.8: *Angular momentum coupling for the Kα transition in La. On the left side the undisturbed levels of 1s and 2p states are shown when no spectator hole is present. In the middle the shifted levels due to the presence of the L spectator hole are displayed. The levels are denoted by the corresponding two hole configurations. The effect of the angular momentum coupling of these two holes is indicated on the right side. The resulting total angular momentum J of the configurations is given as well as the 17 allowed dipole transitions between the initial and final states. The ordinate gives the energy shifts relative to the undisturbed 1 hole states (left side).*

The intensity and the energy shifts (with respect to the K diagram lines), due to this angular momentum coupling between the active (K in the initial state), and the L spectator hole have been calculated using the MCDF code of Desclaux [In91]. In Fig. 5.8 the energy shifts, the splitting of the levels, and the allowed electric dipole transitions are shown. The numerical results are listed in Table 5.13.

For configurations with one L spectator hole and any M holes the shifts can be obtained in a first approximation, by adding to the energy shifts of the L shell (Table 5.13) the average shift of the M spectator holes (Table 5.3a) [for more details see Po90]. The shifts for configurations with more than one L spectator holes can be obtained by summing the single spectator hole average shifts (Table 5.3a). This approximation is justified as the intensity of satellites with more than

one L spectator hole is low and separated from the region with one L spectator satellite.

The angular momentum coupling effect is included by coupling of a L spectator hole to the initial 1s hole and to the final np hole. For an initial hole configuration, the states with different angular momentum are supposed to be created statistically. In the case of the $K\alpha_1$ transition the three L satellite lines split into 9 components (Table 5.13a). The resulting energy shifts, due to a L spectator hole, extend from 23 eV to 119 eV. In Fig. 5.7b we compare the experimental data with this refined theoretical prediction. In this case 285 satellite lines have been superimposed in order to construct the theoretical spectra. There is a substantial improvement in the description of the data.

We further included the angular momentum coupling between the active and one M spectator hole. The results are listed in Table 5.14. For the $K\alpha_1$ satellites with one spectator hole in the M shell, the 5 lines with energy shifts of -1.3 to 12.6 eV split into 24, the shifts of which extend from -12.0 to 22.4 eV. The comparison of the theoretical $K\alpha_1$ spectrum, consisting of 305 satellites, and the measured spectrum is shown in Fig. 5.9a. Compared with the results of Fig. 5.7b, the description of the 'diagram' line is better in the case that the coupling of at least one M spectator has been included.

As we have mentioned, regarding the natural width of 18 eV, and more the total reflection width of 30 eV, the $K\alpha_1$ satellite transitions due to M spectator hole(s) are mostly embedded in the diagram line, leadind to an asymmetry and

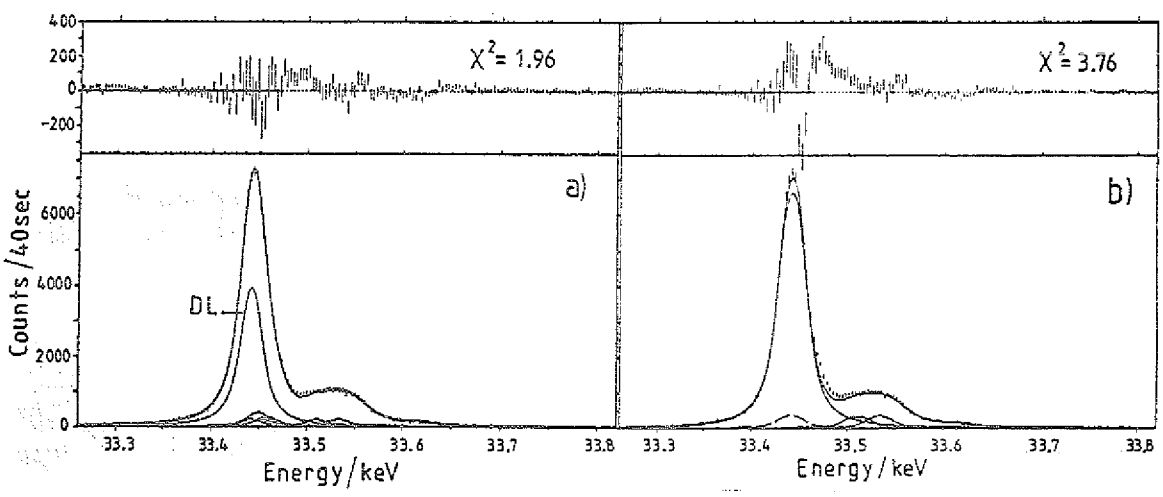

Figure 5.9: *Comparison of the measured (points) first order reflection of the* $K\alpha_1$ *lanthanum X-rays induced by 403 MeV* N^{7+} *with the theoretical line shape (full line). a) The angular momentum coupling between active and one M spectator hole is also included b) The energy shifts of satellite lines due to the presence of M spectator hole(s) are ignored.*

Spectator	$K\alpha_1$				$K\alpha_2$			
	J_i	J_f	ΔE *in eV*	Rate $\times 10^{15}\, sec^{-1}$	J_i	J_f	ΔE *in eV*	Rate $\times 10^{15}\, sec^{-1}$
	1/2	3/2	0.0		1/2	1/2	0.0	
M_I	0	1	18.3	10.91	0	1	20.4	5.57
M_I	1	1	1.9	1.88	1	0	6.2	1.81
M_I	1	2	6.9	9.19	1	1	4.0	3.58
M_{II}	1	2	14.4	11.03	0	1	23.8	5.44
M_{II}	1	1	13.1	1.83	1	0	22.5	3.62
M_{II}	0	1	12.0	9.16	1	1	-3.7	1.81
M_{III}	1	0	-8.6	1.83	1	1	11.4	4.57
M_{III}	1	1	22.4	4.61	1	2	13.0	0.88
M_{III}	1	0	5.3	4.54	2	1	5.3	2.67
M_{III}	2	1	16.3	0.53	2	2	6.9	2.73
M_{III}	2	2	-0.8	2.79				
M_{III}	2	3	16.4	7.73				
M_{IV}	1	0	-4.2	0.51	1	1	6.4	2.74
M_{IV}	1	1	1.4	2.61	1	2	-6.7	2.73
M_{IV}	1	2	-5.0	6.86	2	1	7.3	4.50
M_{IV}	2	1	-4.3	1.84	2	2	-5.8	0.87
M_{IV}	2	2	-3.2	4.46				
M_{IV}	2	3	2.3	4.43				
M_V	2	1	11.2	3.18	2	2	-2.6	4.30
M_V	2	2	3.8	4.14	2	3	-0.7	1.17
M_V	2	3	-2.5	3.06	3	2	-3.4	2.36
M_V	3	2	-3.3	0.81	3	3	-1.3	3.05
M_V	3	3	7.5	2.72				
M_V	3	4	16.4	7.10				

Table 5.14: *Energy shifts of the $K\alpha$ satellites relative to the diagram lines and corresponding electric dipole transitions, splitted due to the angular momentum coupling between the 'active' and one M 'spectator' hole. J_i and J_f denotes the total angular momentum of the initial and the final state.*

broadening, mainly on the high energy side. But compared to the La case, the influence of the M spectator hole(s) to the line shape is expected to be less pronounced for Ta, U (see Fig. 5.3a).

In Fig. 5.9b the comparison between the $K\alpha_1$ spectrum and the theoretical line shape is shown ignoring the M spectator holes. Firstly the 'diagram' line is not well described. Secondly, deviations on the high energy tail of the diagram line arise (χ^2=3.76), which are more significant than in the case where the M holes have been included (χ^2=1.99 ,Fig. 5.9b).

Finally, the effect of the L spectator hole angular momentum coupling in the case of the lanthanum $K\alpha_2$ transtition has been examined. When the angular momentum coupling has not been included a pronounced discrepancy between theory and experiment has been observed (χ^2=13.8), as can be seen in Fig. 5.10a. The comparison between theory and experiment is significantly improved (χ^2=4.35) when the angular momentum coupling is included Fig. 5.10b. The two small bumbs on the high energy side of the 'diagram' and 'L spectator' lines have to be attributed to the uncompleteness of the used model: only the coupling of one L spectator with the active $1s$ or $2p_{1/2}$ holes is taken into account. Further the accuracy of the M ionization probabilities is unknown (more details in the discussion of the $K\beta_{1,3}$ lanthanum doublet). The small deviation above 33.20 KeV, may be attributed to contributions of the $K\alpha_1$ low energy tail (see Fig. 5.1).

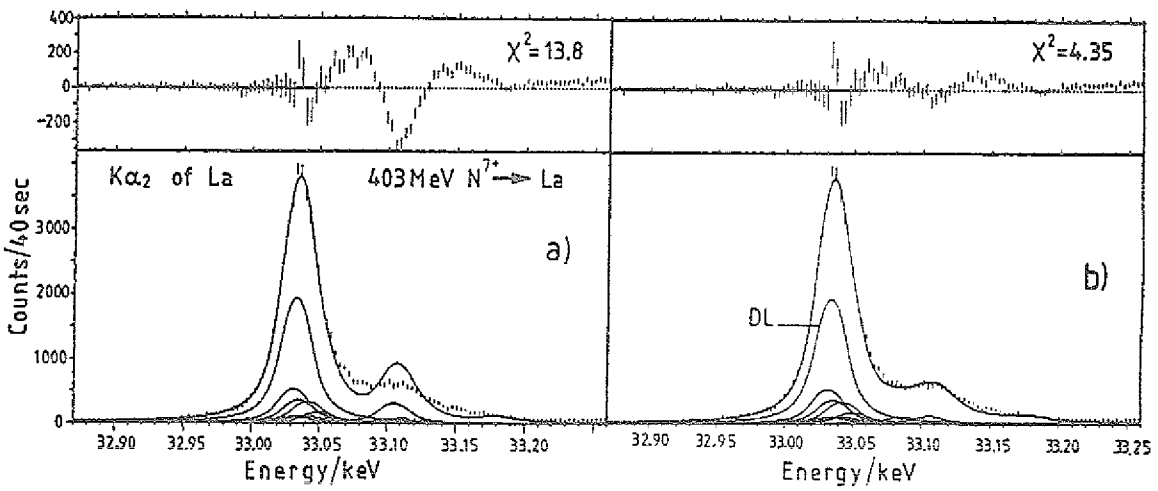

Figure 5.10: *Comparison of the measured (points) first order reflection of the $K\alpha_2$ lanthanum X-rays induced by 403 MeV N^{7+} with the theoretical line shape (full line). On the energy axis are plotted the diagram line (DL) and the strongest satellites. The residues are shown in the upper parts of the figures. a) SCA Coulomb ionization probabilities according to model I used with capture and L subshell coupling but without taking into account the multiplet structure caused by the corresponging L spectator hole. b) The angular momentum coupling between active and one L spectator hole is included*

Comparison of models I and II

The very clean conditions of the lanthanum experiment offer the possibility to test directly the theoretical models I and II. The $K\alpha_1$ spectrum mainly permits a test of the calculated L shell ionization probabilities, without significant dependence on the ionization probabilities of M and higher shells. Because the contributions

to the total ionization probabilities of subshell coupling and capture have been estimated to be small, we can compare the direct ionization probabilities. The predictions of the two models are given in Table 5.15, where are listed the σ_{KL^0} cross section (one K-hole, no L- hole, all other shells inclusive) which has been normalized to 100, the σ_{KL_I}, $\sigma_{KL_{II}}$ and $\sigma_{KL_{III}}$ cross sections, for configurations with one K hole and one hole in the L_I, L_{II} or L_{III} shell, respectively, and the σ_{KL^1}, σ_{KL^2} and σ_{KL^3} cross section for one K-hole and the corresponding number of L-hole(s), relative to the σ_{KL^0}.

Model	σ_{KL^0}	σ_{KL_I}	$\sigma_{KL_{II}}$	$\sigma_{KL_{III}}$	σ_{KL^1}	σ_{KL^2}	σ_{KL^3}
I	100	4.2	8.2	16.0	28.4	3.5	0.2
II	100	3.2	4.4	8.1	15.7	1.1	0.0

Table 5.15: *Cross sections relative to the σ_{KL^0} cross section, which has been normalized to 100, for the system 350 MeV $N^{7+} \rightarrow$ Ta.*

Models I and II differ essentially in the prediction of the cross sections in the case of one or more L spectator holes. For the largest contribution, which corresponds to one L spectator hole, the difference is about a factor of 2.

In Fig. 5.11 we compare the experimental observed $K\alpha_1$ complex with the predictions of the theoretical models. In Fig. 5.11a the K, L, M direct ionization probabilities have been used as they have been calculated with model I and in Fig.

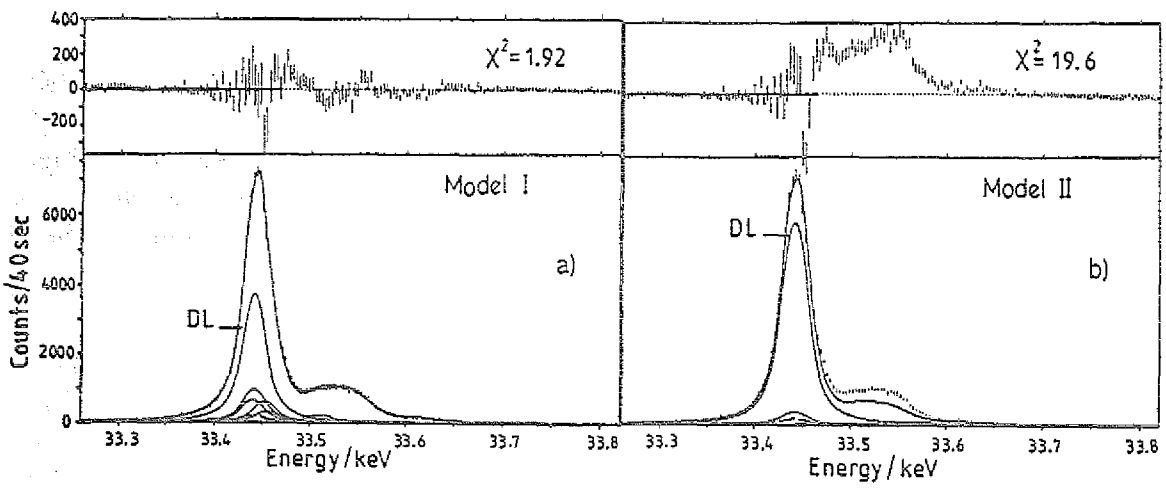

Figure 5.11: *Comparison of models I, II for the ionization probabilities in the framework of the SCA, including the multiplet structure in the case of L spectator hole. Capture and L subshell coupling are not taken into account. a) Model I b) Model II (see text).*

5.11b as we have calculated them with the help of model II. For the creation of the theoretical spectra we have taken into account the multiplet stucture.

The difference in the theoretical predictions I and II of the $K\alpha_1$ satellite structure is very clear. The use of the OPM potential [Aa78] and Hartree-Fock like wave functions describe the experimental data almost quantitatively (χ^2=1.9), whereas the use of a screened Coulomb potential and relativistic hydrogenic wave functions understimates significantly the ionization probabilities of the L subshells (χ^2=20.).

The $K\beta_{1,3}$ lanthanum doublet

Finally, the complex of the $K\beta_{1,3}$ lanthanum doublet is investigated, where the energy shifts of the satellite lines are larger than in case of $K\alpha$ (Table 5.3, Fig. 5.3b). For the $K\beta$ the satellite spectrum due to a L spectator extends on the high energy side of the diagram lines, from 150 to 210 eV. As the energy difference between $K\beta_1$ and $K\beta_3$ is 81 eV the corresponding satellite structure of the $K\beta_3$ partly overlaps with the $K\beta_1$. The energy shifts due to a M spectator hole extend from 20 to 35 eV. Therefore the $K\beta_{1,3}$ permits a check of the theoretical M ionization probabilities.

In Fig. 5.12 is shown the comparison of the measured spectrum and the theoretical line structure using the ionization probabilities according to model I. The ratio between the $K\beta_3$ and $K\beta_1$ lines has been taken as 0.518 [Sa74]. Also the $K\beta_5^{II}$ and $K\beta_5^{I}$ transitions ($K\rightarrow M_{IV},M_V$) have been included which are 273 and 293 eV, respectively, higher in energy than the $K\beta_1$ [Be67]. The total intensity of the $K\beta_5^{I,II}$ lines is 1.4% of the intensity of the $K\beta_1$ transition [Sc74].

In Fig. 5.12a the L spectator angular momentum coupling has not been included. For the construction of the theoretical line shape 320 satellite lines have been included. The shape of deviation between experiment and theory in the region of the L satellites lines underlines the importance of the angular momentum coupling.

In Fig. 5.12b the effect of the L spectator angular momentum coupling has been included (Table 5.13) and for the construction of the theoretical line shape a total of 654 satellite lines have been used. The χ^2 has been reduced from 3.8 to 2.3 and the deviations in the L satellite lines region have been diminished.

Regarding the complexicity of such a spectrum the agreement between experiment and theory is very good. In this case, as the presence of a M spectator hole creates a mean energy shift in the order of the experimental resolution, the coupling of the M spectator hole with the rest of active and spectator holes has to be taken into account. The drastical increase of the number of the involved transitions has prevented a solution of this problem up to now. Further the rearrengement of the M holes, due to Super Coster-Kronig transitions and to higher shells should be taken into account. Unfortunately there are no reliable values available for the transitions rates of such de-excitation channels. The small discrepancies arising

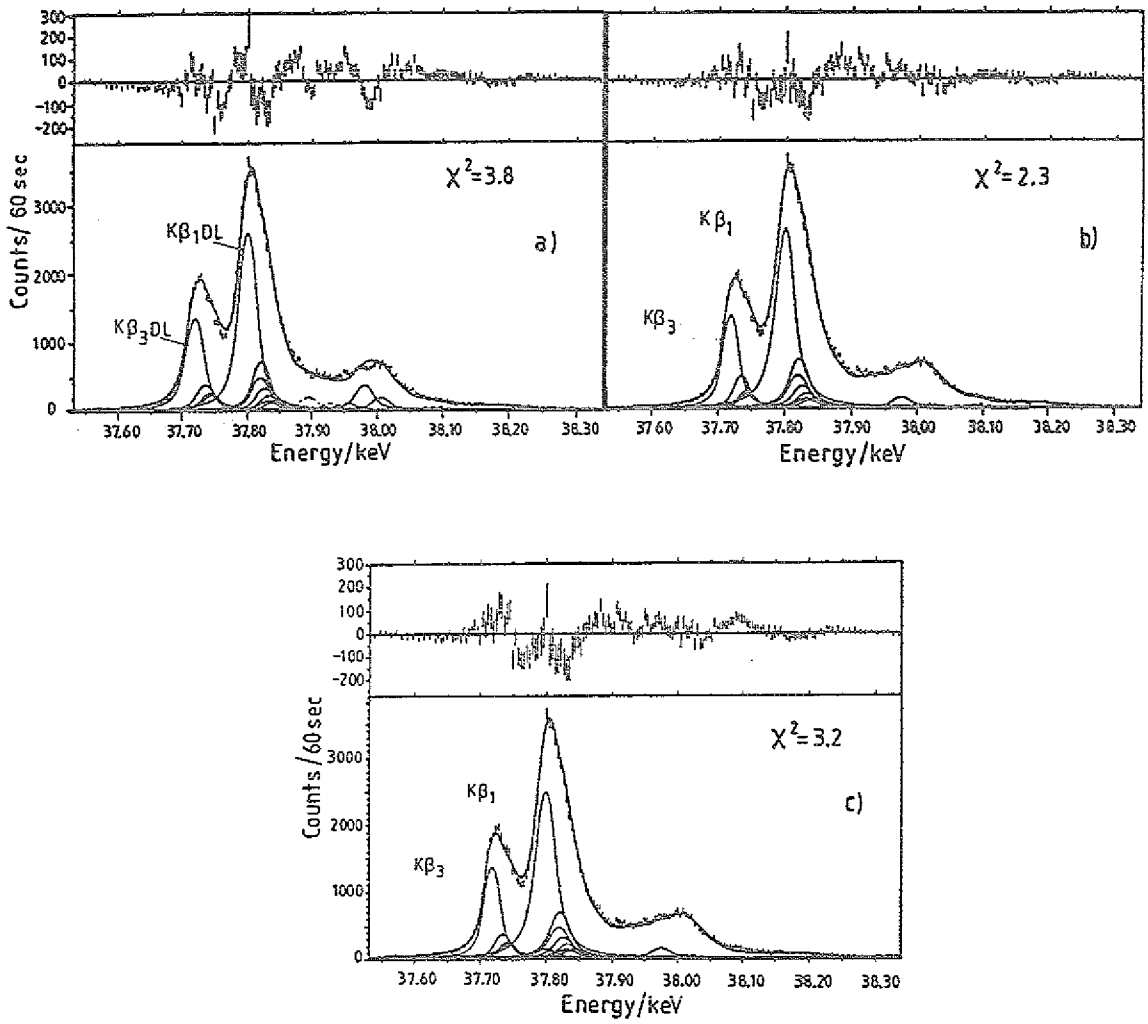

Figure 5.12: *Comparison of the measured (points) first order reflection of the* $K\beta_{1,3}$ *lanthanum X-ray doublet induced by 403 MeV* N^{7+} *ions with the theoretical line shape according to model I (full line) including capture, L subshell coupling. a) The multiplet structure in the case of L spectator hole has not been taken into account. b) The multiplet structure is also included. c) Not inclusion of the* $K\beta_5^{I,II}$ *transitions in the theoretical* $K\beta_{1,3}$ *lanthanum satellite complex spectrum gives the deviation in the region of 38.10 KeV.*

in the region of the diagram lines are attributed to these effects.

The sensitivity of our analysis is demonstrated in Fig. 5.12c. The $K\beta_{1,3}$ spectrum has been fitted as in the case of Fig. 5.12b, taking into account the L spectator angular momentum coupling, but the $K\beta_5^{II}$ and $K\beta_5^{I}$ transitions have not included. The $\chi^2 = 3.2$ is significantly increased. In the energy region (~ 280 eV) of these lines the intensity is clearly underestimated.

5.4.2 ...of Tantalum with 350 MeV nitrogen

The average energy shifts of the satellite lines, due to one spectator hole in L or M subshells with respect to the $K\alpha_1$, $K\alpha_2$, and $K\beta_{1,3}$ diagram lines for Ta are listed in Tables 5.3b. The angular momentum coupling of the L spectator hole to the initial 1s hole and to the final 2p hole has been calculated for the cases of the $K\alpha_{1,2}$ transitions. The intensity and the energy shifts, with respect to the corresponding $K\alpha$ diagram lines, have been calculated using the MCDF code. The results of the multiplet structure of the $K\alpha$ transitions in the case of L spectator holes are listed in Table 5.16.

Fit model discussion

In Fig. 5.13 the measured Ta $K\alpha_1$ spectrum, in second order reflection, has been fitted using the ionization probabilities as predicted by Model I, taking into account the angular momentum coupling. Several fit models have been tested and are discussed. In Fig. 5.13a,b we have fitted from the low energy side of the $K\alpha_1$ line up to +40 eV to the high energy side. As the satellite structure is not expected to extend to the low energy side of the diagram line the fit parameters can be adjusted in the region without interference with the satellite structure. In Fig. 5.13a the M holes have been ignored (fit model H0), but they have been included in Fig. 5.13b (fit model HM), using the M ionization probabilities as predicted by Model I. In the first case a χ^2 of 2.1 has been obtained and in the later χ^2 equal to 1.3. Comparing the two figures, in the case that the M spectator holes have been included, the fit is better in the high energy side of the diagram line, in the energy region from 0 to +50 eV. This shows that the detailed inclusion of the M spectator holes leads to a better description of the line structure in the region of the $K\alpha_1$ diagram line and it is clear that it is even more important in the case of $K\beta$s. But in both cases (see Fig. 5.13a,b) the description of the L satellite structure is similar and reproduced quite good. In Fig. 5.13c,d. are shown the results after fitting of the whole spectrum. In the fitting procedure of Fig. 5.13c the M satellite lines have not been included (fit model W0) and χ^2 equals to 1.7. When they are included (fit model WM) the χ^2 is reduced to 1.1 as shown in Fig. 5.13d.

Keeping the ionization probabilities ratios $P_{L_I}/P_{L_{II}}/P_{L_{III}}$ constant, as they are predicted by Model I, and scaling them by a common factor, we have fitted the $+2.K\alpha_1$ spectrum using the fit models HM, H0, WM and W0. The corresponding χ^2 values as function of the ionization probabilities, for the four used fitting procedures, are shown in Fig. 5.14a. In general the obtained χ^2 value for the set same of ionization probabilities is different from the one model to the other. But at least three models (HM, H0 and WM) predict their minimum χ^2 for ionization probabilities which do not differ more than 2%. The prediction of the fourth model (W0) deviates by 5%. A commom feature of the fitting procedures which fit over the whole spectrum (HM,H0 models) is that they tend to smear out and to

Table 5.16a

Spectator	Transition		Energy shift *in eV*		Rate $\times 10^{16}\ sec^{-1}$	
	$J_i \rightarrow$	J_f	Ta	U	Ta	U
	1/2	3/2	0.	0.	3.13	8.32
L_I	0	1	176.	307.	2.97	8.20
L_I	1	1	36.	64.	0.60	1.48
L_I	1	2	118.	181.	2.64	7.00
L_{II}	0	1	200.	375.	3.18	8.45
L_{II}	1	1	168.	254.	0.51	1.38
L_{II}	1	2	149.	237.	2.72	7.12
L_{III}	1	0	80.	108.	1.05	2.79
L_{III}	1	1	—	—	—	—
L_{III}	1	2	140.	192.	2.58	6.94
L_{III}	2	1	—	—	—	—
L_{III}	2	2	96.	132.	1.61	4.24

Table 5.16b

Spectator	Transition		Energy shift *in eV*		Rate $\times 10^{16}\ sec^{-1}$	
	$J_i \rightarrow$	J_f	Ta	U	Ta	U
	1/2	3/2	0.	0.	1.51	3.86
L_I	0	1	200.	330.	1.73	4.14
L_I	1	0	98.	131.	0.51	1.30
L_I	1	1	60.	88.	0.95	2.50
L_{II}	0	1	—	—	—	—
L_{II}	1	0	116.	171.	1.02	2.60
L_{II}	1	1	—	—	—	—
L_{III}	1	1	131.	163.	0.27	0.27
L_{III}	1	2	113.	146.	1.25	3.20
L_{III}	2	1	89.	103.	0.76	1.94
L_{III}	2	2	71.	86.	0.73	1.90

Table 5.16: *Energy shifts of the* $K\alpha_1$ *and* $K\alpha_2$ *satellites relative to the tantalum and uranium diagram lines and corresponding electric dipole transition rates, splitted due to the angular momentum coupling between the 'active' and one L 'spectator' hole.*J_i *and* J_f *denotes the total angular momentum of the initial and the final state.*

balance deviations, in order to find the minimum χ^2.

As next step the $-2.K\alpha_1$ spectrum has been fitted using the fit models HM and WM. The results are shown in Fig. 5.14b. The behavour is similar to the case of the $+2.K\alpha_1$ spectrum. The two models predict the minimum χ^2 for the same

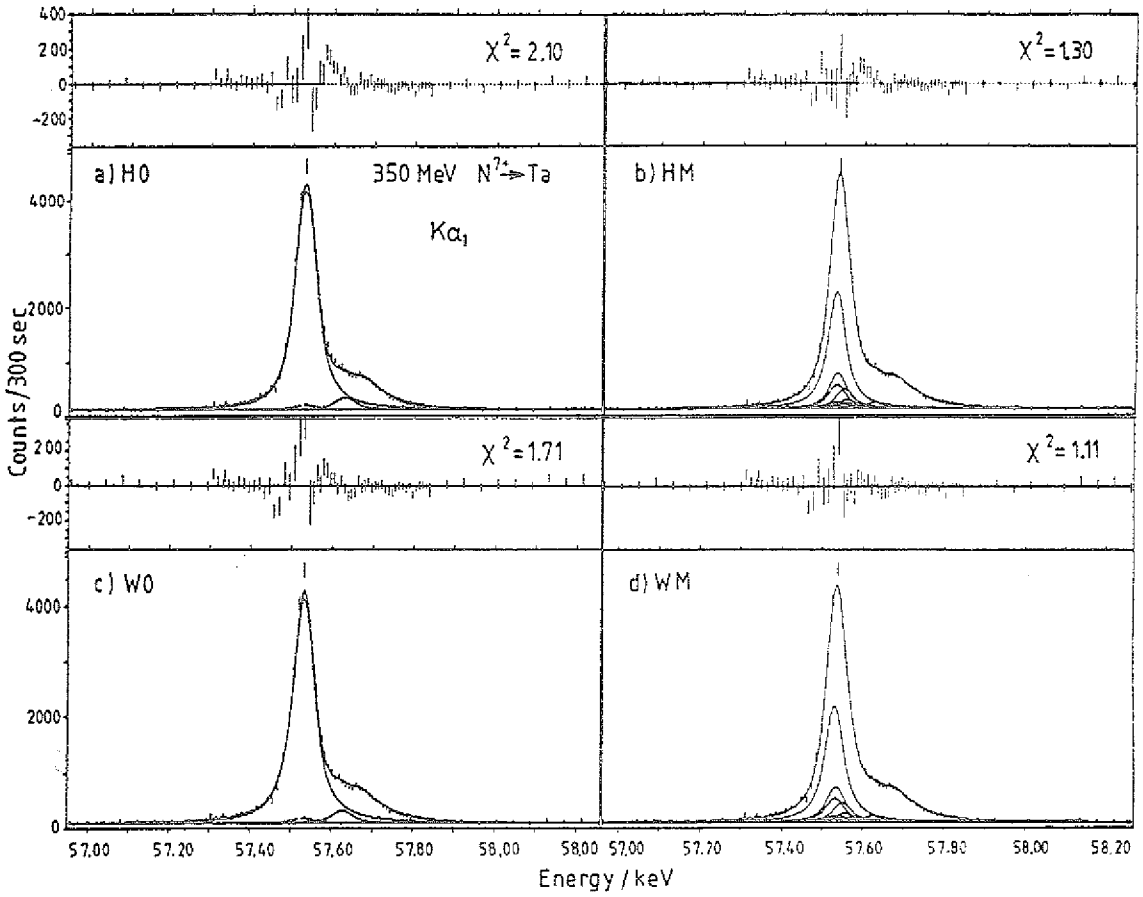

Figure 5.13: *Comparison of the measured (points) second order reflection of the* $K\alpha_1$ *tantalum X-rays induced by 350 MeV* N^{7+} *with the theoretical line shape (full line) determined from the fit models: a) H0 b) HM c) W0 and d) WM (see text).*

set of ionization probabilities P_L.

Comparing the results of Fig. 5.14a-b of the minimum χ^2 as function of the ionization probabilities for the $K\alpha_1$ spectra of Ta, at positive and negative Bragg angle, we see that the positions of the minimum χ^2 are obtained for ionization probabilities differing less than 5%. This shows that the experimental uncertainty is less than 5%.

Comparison of models I and II

The predictions of the Model I and Model II for the system 350 MeV $N^{7+} \rightarrow$ Ta are tested, by a comparison with the measured $K\alpha_1$ spectrum of Ta. The predictions of the two models are given in Table 5.17.

In order to avoid interference from the different M ionization probabilities predictions of the two models we use the H0 fit model. The results are shown in Fig.5.15a for Model I and in Fig.5.15b for Model II. The χ^2 is 2.1 and 6.6,

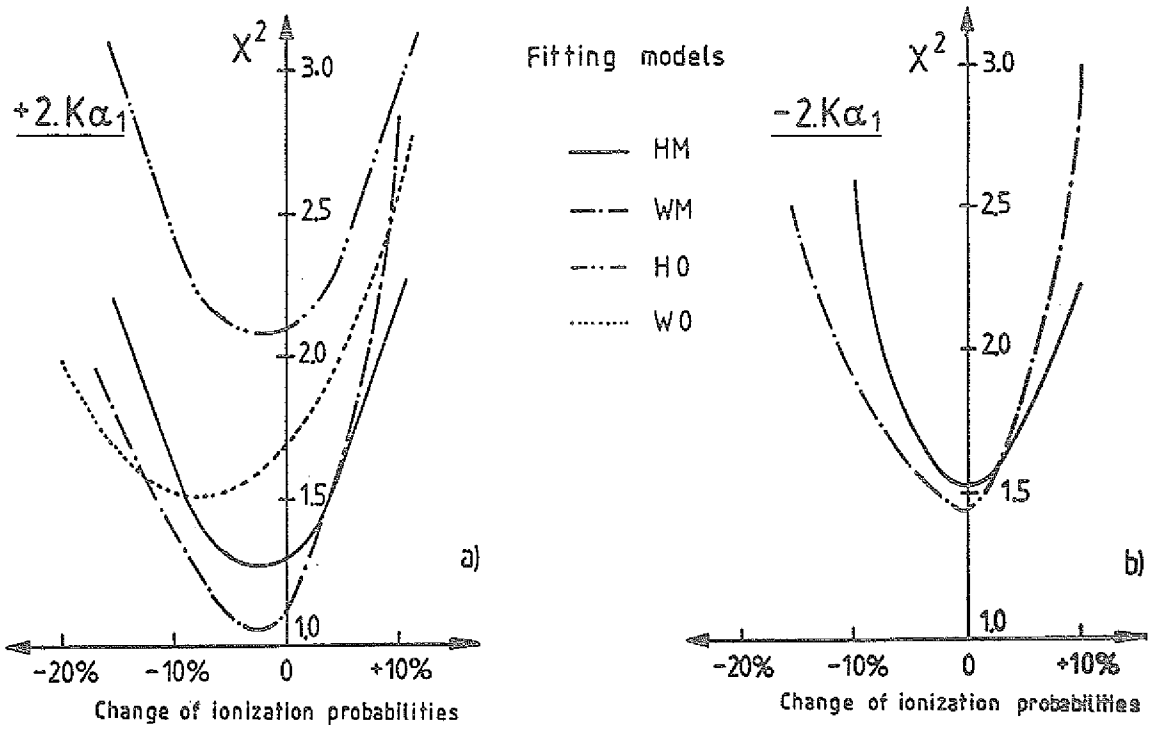

Figure 5.14: *The reduced χ^2, resulting from the comparison between experimental spectra and theoretical predictions, as function of the percent change of the* P_L *ionization probabilities, as they have been calculated from Model I a) for +2.*$K\alpha_1$ *measured spectrum and the H0, HM, W0 and WM fit models and b) for -2.*$K\alpha_1$ *measured spectrum and the H0, HM fit models*

Model	σ_{KL^0}	σ_{KL_I}	$\sigma_{KL_{II}}$	$\sigma_{KL_{III}}$	σ_{KL^1}	σ_{KL^2}	σ_{KL^3}
I	100	2.8	6.9	13.6	23.3	2.4	0.1
II	100	2.4	4.8	8.7	15.9	1.1	0.0

Table 5.17: *Cross sections relative to the* σ_{KL^0} *cross section, which has been normalized to 100, for the system 350 MeV* $N^{7+} \rightarrow$ *Ta.*

in Fig.5.15a for Model I and in Fig.5.15b for Model II. The χ^2 is 2.1 and 6.6, respectively. Model II clearly underestimates the ionization probabilities. The correction due to the L subshell coupling and capture have not been included, but as can be seen from Tables 5.7 and 5.8 they almost cancel.

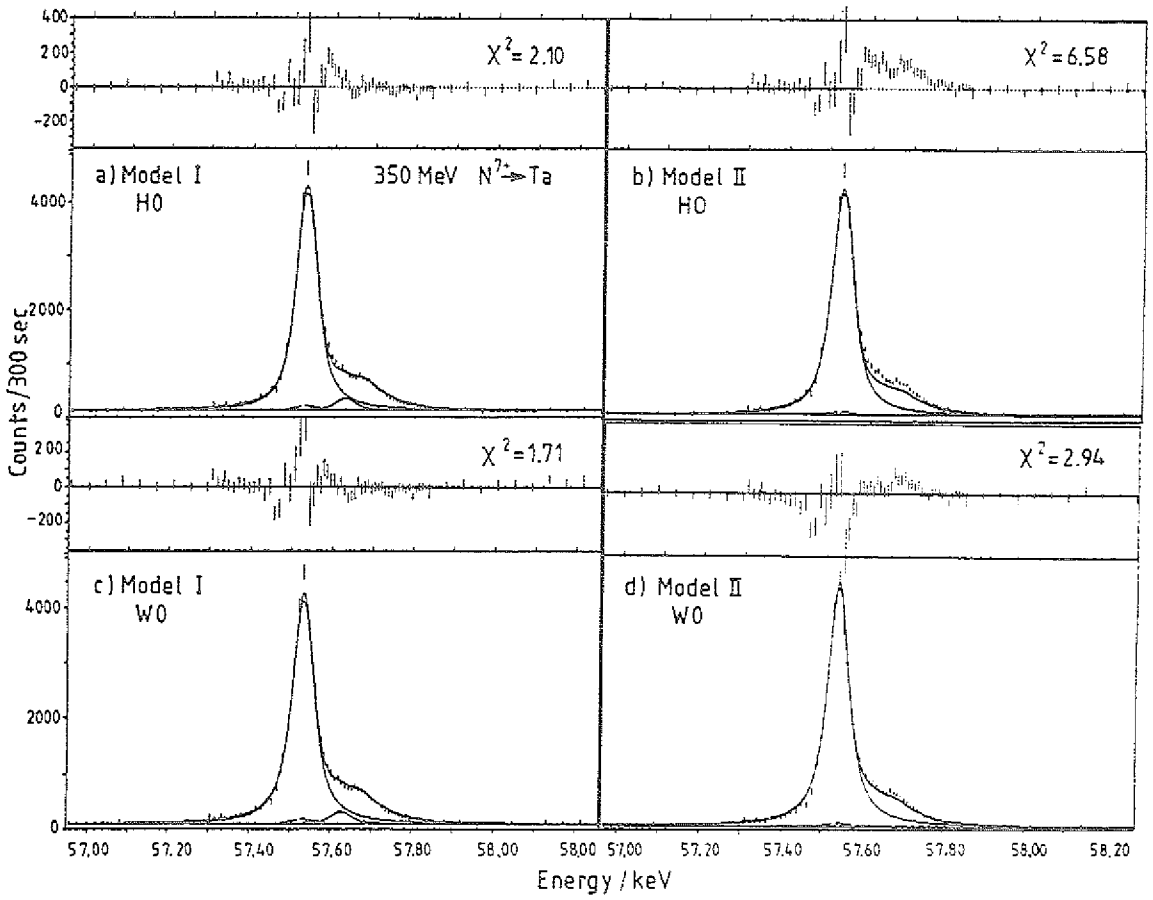

Figure 5.15: *Comparison of the models I, II for the ionization probabilities in the framework of the SCA, including the multiplet structure in the case of L spectator hole. Capture and L subshell coupling are not taken into account. In a), b) the fit model H0 has been used and in c), d) the W0.*

Model II, respectively. The χ^2 in the case of Model I is 1.7 and in the case of Model II 2.9. From Fig.5.15d it is obvious that the Model II underestimates the ionization probabilities, but this deviation is not so clear as in the case of Fig.5.15b.

In Fig. 5.16a is shown the comparison of the experiment with the predictions of Model I including the L subshell coupling (χ^2=1.84). In Fig. 5.16b the contribution from the capture of L target electrons has been added (χ^2=1.32). The agreement is good. The HM fit model has been used.

The comparison of the experimental -2.Kα_1 spectrum with the theoretical predictions including all the above discussed effects is shown in Fig. 5.17.

Finally, in Fig. 5.18 we display the comparison of +2.Kα_1 spectrum with the theoretical predictions without inclusion of the j-j coupling of the L spectator. The χ^2=2.48 is larger than in the case where the j-j coupling has been included (χ^2=1.32). It is noteworthy, that the effect of including the j-j coupling is not so

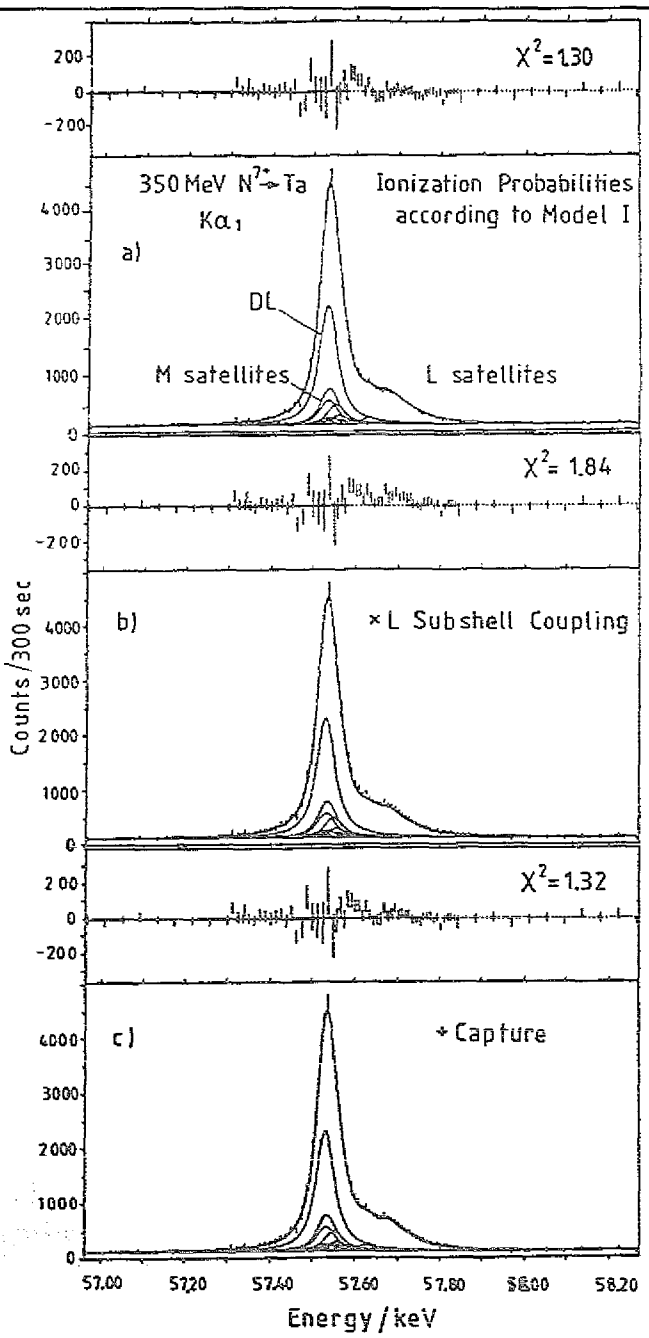

Figure 5.16: *Comparison of the second order reflection of the $K\alpha_1$ tantalum X-rays induced by 350 MeV $^{14}N^{7+}$ (measured points) with the theoretical line shape (full line). Also with full lines are given the diagram line (DL) as the largest component and some of the strongest satellites. a) Only the SCA Coulomb ionization mechanism has been included, with ionization probabilities as they are predicted by Model I. b) The L subshell coupling correction has been included c) The capture of target electrons by the projectile has been also taken into account.*

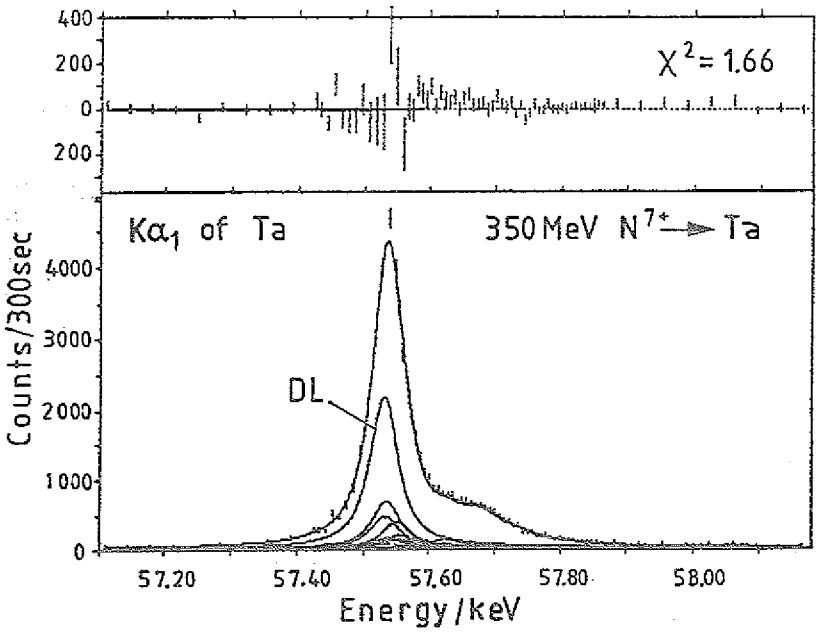

Figure 5.17: *-2.Kα_1 reflection of tantalum X-rays induced by 350 MeV nitrogen (measured points) with the theoretical line shape (full line). The SCA Coulomb ionization probabilities according to Model I, with the L subshell coupling correction to it, and the capture mechanism contribution have been included.*

Figure 5.18: *Comparison of the +2.Kα_1 spectrum with the complete theoretical predictions without inclusion of the j-j coupling of active and L spectator hole.*

pronounced here as in the lanthanum case. This is due to the total energy resolution, which is ~ 60 eV in the Ta case.

The $K\beta_{1,3}$ tantalum doublet

The tantalum $K\beta_{1,3}$ complex has been studied. The measured spectrum is compared with the theoretical line structure predicted by using the ionization probabilities according to model I, modified by the subshell coupling, and including the L capture probabilities. The ratio $K\beta_3/K\beta_1$ has been taken equal to 0.518 [Sa74] and it has been assumed that the lines have the same natural width. Also the $K\beta_5^{II}$ and $K\beta_5^{I}$ transitions have been included which are at energies of 403 and 460 eV higher than the $K\beta_1$ [Be67]. The total intensity of the $K\beta_5^{I,II}$ lines is 2.5% of the intensity of the $K\beta_1$ transition [Sc74].

The comparison between experiment and theory is shown is Fig. 5.19. The overall description of the spectrum is good (χ^2=1.65). The L satellite structure of the $K\beta_3$ complex lies under the diagram $K\beta_1$ transition. For possible additional contributions compare to the discussion of the La case. Moreover, in the present case the L spectator angular momentum coupling has not been included.

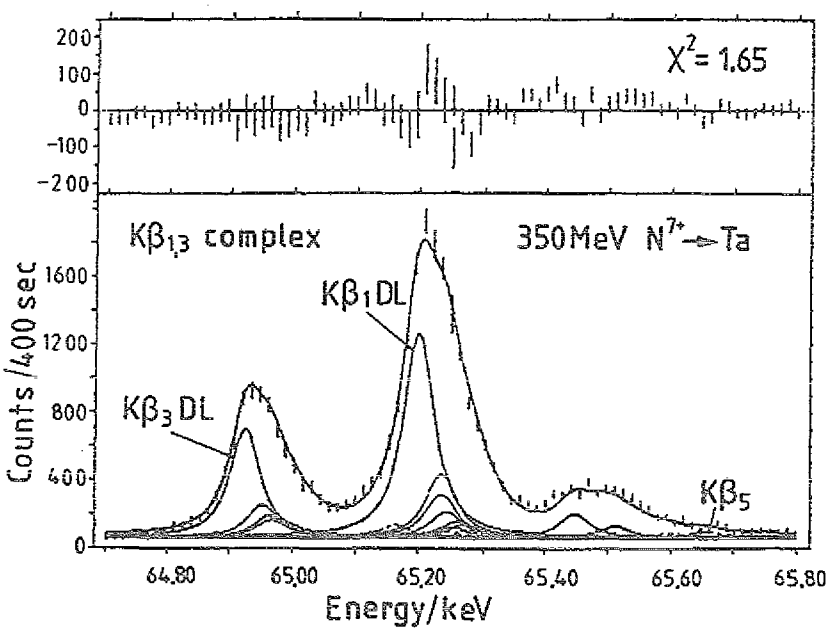

Figure 5.19: *The $K\beta_{1,3}$ complex of Ta measured in second order reflection is compared to the theoretical prediction. The diagram lines and some intense satellites are also shown indicating the overlap of the satellite structure of $K\beta_1$ and $K\beta_3$.*

5.4.3 ...of Uranium with 500 MeV neon

The study of the system 500 MeV $Ne^{10+} \rightarrow U$, except the comparison between model I and II, which for the present system differ by less than 15% (the prediction of the two models is given in Table 5.18), permits mainly the test of the importance of the subshell coupling as it is predicted to be in the order of 30% (see Table 5.8) and secondly of the target L electron capture probability, which is estimated to contribute to the creation of L hole by 10%–15% compared to the direct L ionization probability (see Table 5.9).

Model	σ_{KL^0}	σ_{KL_I}	$\sigma_{KL_{II}}$	$\sigma_{KL_{III}}$	σ_{KL^1}	σ_{KL^2}	σ_{KL^3}
I	100	4.1	8.8	17.2	30.1	4.0	0.3
II	100	3.4	7.8	14.2	25.4	2.8	0.2

Table 5.18: *Cross sections relative to the σ_{KL^0} cross section, which has been normalized to 100, for the system 500 MeV $Ne^{+10} \rightarrow U$.*

The measured second order $K\alpha_1$ spectrum of uranium has been fitted using the H0 fit model. The fit region was from low energy side of the transition, up to +85 eV at the high energy side.

The average energy shifts of the satellite lines, due to one spectator hole in the L or M subshells, with respect to the $K\alpha_1$, $K\alpha_2$, and $K\beta_{1,3}$ diagram lines for U are listed in Tables 5.3c. The M spectator holes have not considered individually as they are well hidden due to the total energy resolution of $\sim$ 145 eV. The effect of the angular momentum coupling (due to the angular momentum coupling of the L spectator hole to the initial 1s hole and to the final 2p hole) has been calculated in the case of the $K\alpha_{1,2}$ transitions. The intensities and the energy shifts with respect to the corresponding $K\alpha$ diagram lines have been calculated using the MCDF code. The results of the multiplet structure of the Ka transitions in the case of L spectator holes are listed in Table 5.16b.

In Fig. 5.20 a_1, b_2 the uranium $K\alpha_1$ spectrum is compared with the theoretical prediction of Model I and II, respectively. Model I clearly overestimates the experimental spectrum (χ^2=2.17), whereas Model II is in much better agreement (χ^2=1.03).

But as the projectile velocity is lower than the L electron orbital velocities it is expected that binding effects for these electrons are significant, and the use of the separated–atom approximation must be questioned. As the projectile moves relative slowly into the L shells, molecular effects may arise more probable than in the lighter systems. The results, when the subshell coupling has been included, are shown in Fig. 5.20 a_2, b_2 for Model I and II, respectively. For Model I the agreement is better than before (χ^2=1.36), but it underestimates the experimental data. This trend is more pronounced for Model II (χ^2=2.46).

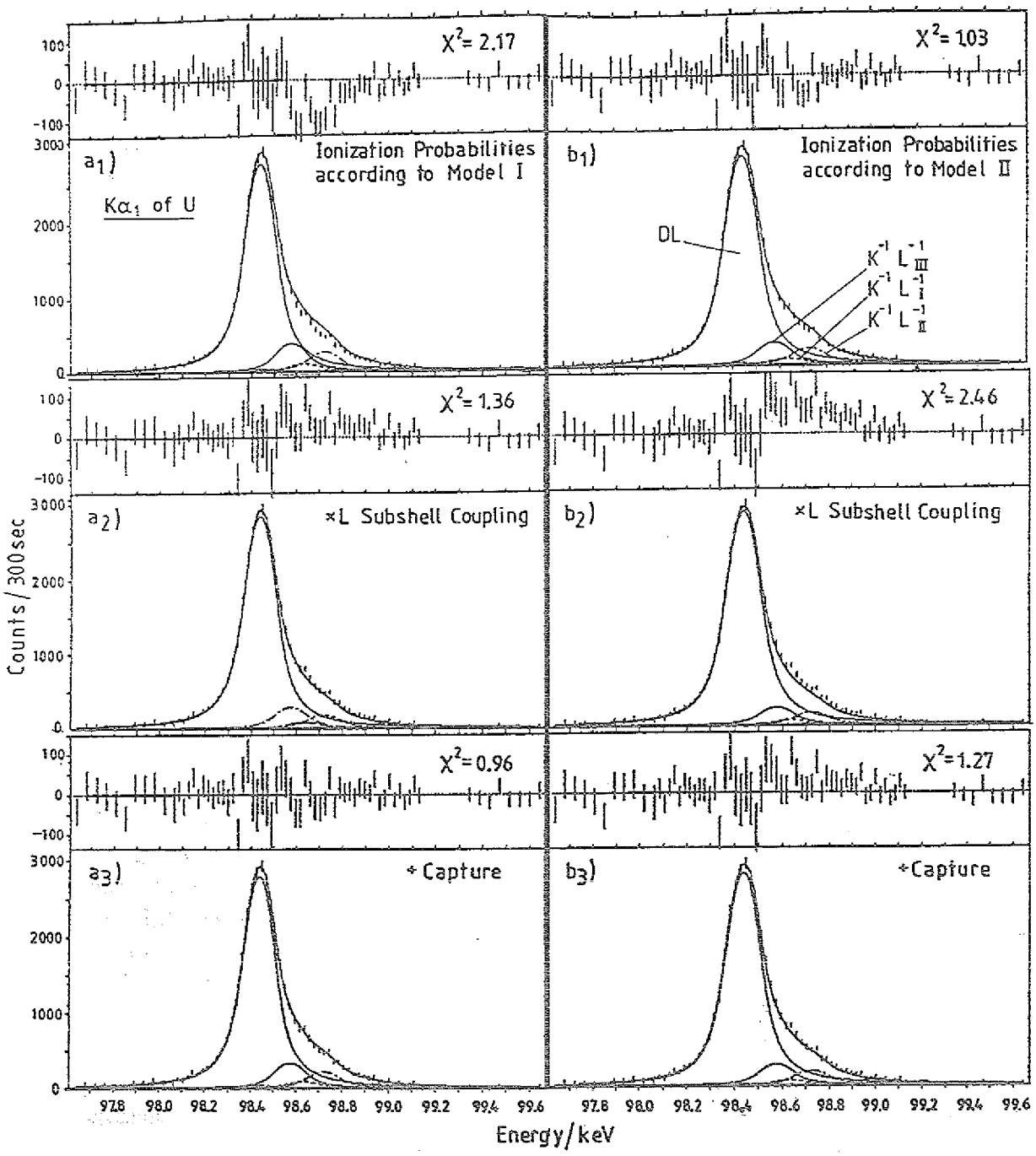

Figure 5.20: *Comparison of the second order reflection of the* $K\alpha_1$ *uranium X-rays induced by 500 MeV* $^{20}Ne^{10+}$ *(measured points) with the theoretical line shape (full line) based on a) Model I and b) Model II.* a_1, b_1) *Only the SCA Coulomb ionization mechanism has been included.* a_2, b_2) *The L subshell coupling has been included.* a_3, b_3) *The contribution of the capture mechanism has also been included.*

The reason for this discrepancy is the omission of the capture mechanism which acts to remove target electrons. When we add now the contribution due to the capture mechanism the agreement between experiment and the theoretical predictions based on Model I, is very good ($\chi^2 = 0.96$) (see Fig. 5.20 a_3). Using Model II for the direct ionization probabilities the underestimation of the experimental data remains (see Fig. 5.20 b_3), as in all the other systems which we have studied.

In Fig. 5.21 the uranium $K\alpha_1$ spectrum measured in the third order reflection has been fitted, in the same way as before, taking into account the theoretical predictions for the direct ionization probabilities according to the Model I, modified by the subshell coupling, and including the capture. The χ^2 has been found equal to 1.08, confirming the previous results.

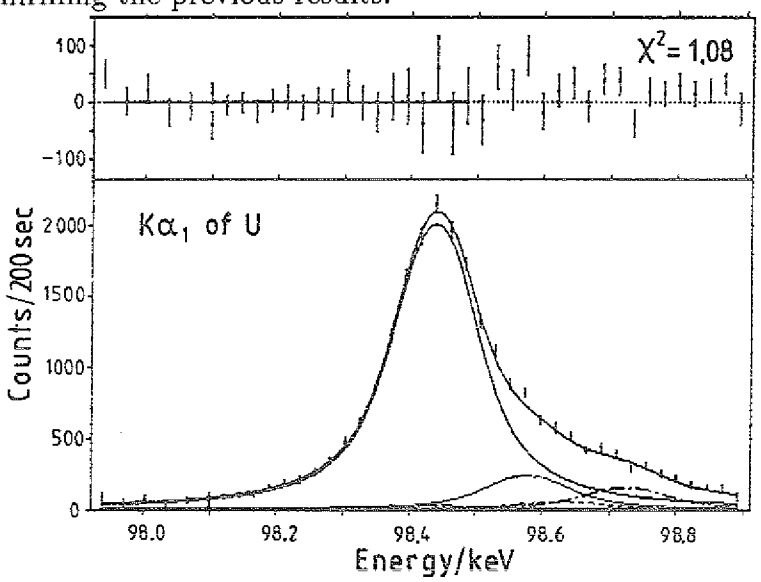

Figure 5.21: *Third order reflection of the $K\alpha_1$ uranium X-rays induced by 500 MeV neon (measured points) with the theoretical line shape (full line). The SCA Coulomb ionization mechanism with the L subshell coupling correction to it, and the capture mechanism have been included.*

The $K\beta_{1,3}$ uranium doublet

Finally the complex of the $K\beta_{1,3}$ uranium doublet has been investigated. The energy difference between the $K\beta_1$ and $K\beta_3$ lines is 883 eV, whereas the energy shifts due to one spectator hole in L or M shell vary from 35 to 495 eV (Table 3c). The intensity ratio of the $K\beta_3$, $K\beta_1$ diagram has been taken equal to 0.527 [Sa74] (Fig. 5.22). The general agreement between theory and experiment is rather good.

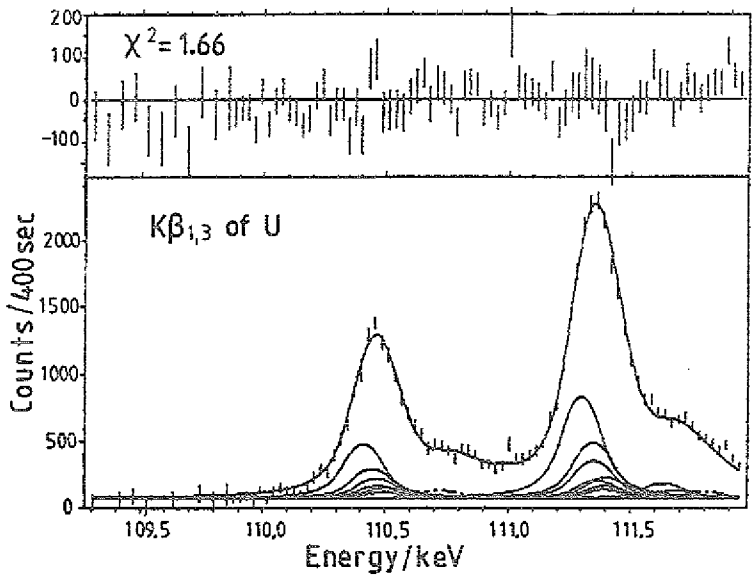

Figure 5.22: *The* $K\beta_{1,3}$ *complex of U measured in second order reflection is compared to the theoretical prediction. The diagram lines and some intense satellites are also shown indicating the nearly separated structure of the of the* $K\beta_1$ *and* $K\beta_3$ *satellites.*

6. Conclusions

The L – shell ionization probabilities for nearly central collisions have been studied.

The high resolution K X – ray spectra, produced during the bombardement of La, Ta and U with beams of 403 MeV N^{7+}, 350 MeV N^{7+} and 500 MeV Ne^{10+}, respectively, have been compared with the theoretical constructed K X – ray spectra, based on the calculations for the direct L electron ionization probabilities, obtained using the energy optimised effective atomic central potentials (OPM) and screened hydrogenic potentials.

For the analysis the rearrangement of the L – shell vacancies due to a possible filling prior to the decay of the K vacancy has been taken into account.

The multiplet splitting in the case of the one L spectator hole has been included. The effect of the hole – hole interaction between the active and the L spectator hole has been clearly demonstrated, predominantly in the case of lanthanum. It has been shown to be an important contribution to the understanding of the experimental spectra.

The K fluorescence yields in the presence of an L spectator hole has been calculated *abinitio* in the case of lanthanum. The changes of the fluorescence yields, mainly during the presence of L spectator hole, are significant and essential for the comparison between experimental and theoretical cross sections. An semi – emprical formula has been suggested, which can reproduce the *ab initio* results rather reliably.

With the inclusion of these contributions the initial configuration of the excited atom can be converted to the hole configuration at the moment when the K X – ray is emitted and observed.

Comparison between the experimental spectra and the theoretical predictions demonstrates that wave function effects are generally important for inner – shells of atoms during fast collision. As a result we could show that the use of the wave functions according to the OPM potential describes the L satellite structure in a very good way. The predictions of the SCA using hydrogenic wavefunctions strongly underestimate the experimental spectra.

In the system 403 MeV $N^{7+} \rightarrow$La, where the ratio of the projectile's velocity to the L – shell electron velocity was the largest and larger than the unity, the wave function effects were the most pronounced. In the system 350 MeV $N^{7+} \rightarrow$Ta the above conclusions have been confirmed. In the system 500 MeV $Ne^{10+} \rightarrow$U, where the projectile's velocity was lower than that of the L shell electrons of uranium, binding effects arise and the inclusion of the subshell coupling was necessary to describe the experimental data. In all cases the capture process has been included, but as it is generally a small contribution, it is not possible to extract safe

conclusions.

In 1979, impact parameter measurements were performed for collisions where the projectiles moves at a speed somewhat larger than the target electrons [Ho79]. The proton induced K-shell ionization of Ne and C in the collision energy range 0.1-10 MeV was measured. The experimental results were compared with calculations for the impact parameter distribution of K atomic ionization probabilities, using energy optimized effective atomic central potentials (OPM) and screened hydrogenic potentials [Aa81]. It was concluded that the wave functions effects are, in general, quite large and strongly impact parameter dependent for light systems. The OPM wave functions improves the agreement between theory and recent experiments, especially for the more rapid collisions.

The L-shell ionization probabilities in near central collisions of 6.7 MeV/amu He ions with mid-Z atoms, measuring the K X-ray spectra, have been studied [Ry92]. The theoretical predictions of SCA theory using the hydrogenic wavefunctions have been found to underestimate the measured cross sections. The observed deviation is higher as the ratio V_{proj}/V_L is increased.

A. Doppler effect

When the fast ion-projectile passes through the target atom, besides the energy transfer through the Coulomb interaction to inner-shell electrons and their excitation or ejection, the Coulomb interaction with the nucleus of the target atom leads to its recoil. The moving particle is deflected. The recoiling target atom will de-excitate, mainly by photon emission. The energy of the photon emitted by the moving atom is shifted in energy, due to the Doppler effect. The observed photon energy E is given by:

$$E = \frac{1 - (V_R/c)\,\cos(\theta)}{\sqrt{1 - (V_R/c)^2}}\,E_0 \tag{A.1}$$

where E_0 is the photon energy when the emitting atom is at rest, θ is the angle of detection with respect to the direction of the motion of the atom, V_R is the speed of the atom, and c the speed of light.
Taking the Taylor expansion of the above formula the Doppler shift equation is given by:

$$E - E_0 = E_0\,[\frac{V_R}{c}\cos\theta - \frac{1}{2}(\frac{V_R}{c})^2 + \ldots] \tag{A.2}$$

The first order depends both of the atom speed V_R and the angle θ. Thus the emitted photon can be either shifted to higher energies if the source approaches the detector or to lower energies in the case that the source recedes from the detector. The second-order Doppler shift is independent of the angle of the emission and is always a shift to lower energies.

In order to calculate the Doppler effect during the ion-atom collision the equations relating the initial and final states of the elastic scattering of the two particles are needed. The final velocities and trajectories can be found from the conservation of momentum and energy of the system. Supposing classical nonrelativistic elastic collisions the transfer of energy between a moving and a stationary charged particle depends only on the mass and the charge of the two point particles, and the moving particle's initial speed and direction.

The recoil velocity V_R of the target atom, as a function of its recoil angle a_R, in the laboratory system(Fig. A.1), is given by the expression:

$$V_R = 2\,V_0\,\frac{M_c}{M_2}\,\cos(a_R) \tag{A.3}$$

where V_0 is the incident velocity of the ion of mass M_1, M_2 is the target mass and $M_c = \frac{M_1 M_2}{(M_1+M_2)}$ is the reduced mass of the system.

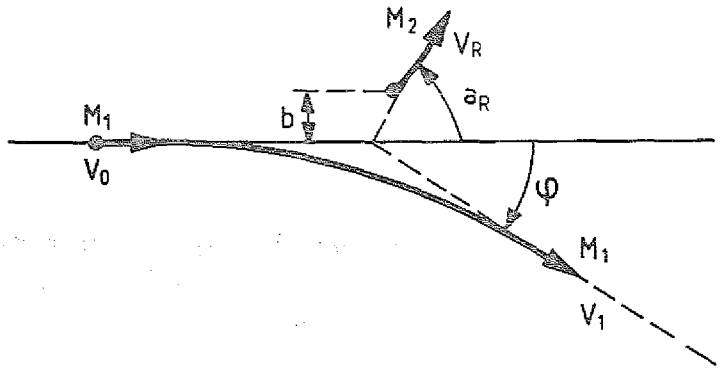

Figure A.1: *Scattering variables in a two – body collision in the laboratory system. The projectile has mass M_1 and an initial velocity V_0, and impinges on the target with an impact parameter b. The projectile's final angle of deflection is ϕ and its velocity is V_1. The target particle with mass M_2, recoils at an angle a_R with velocity V_R.*

The projectile's scattering angle ϕ_{cm} is related to the impact parameter b, in the center – of – mass system, through Rutherford's scattering law [see Br83, page 598],

$$\phi_{cm} = 2 \tan^{-1}(b_0/2b) \tag{A.4}$$

where b_0 is the minimum distance of approach, given by:

$$b_0 = \frac{2 Z_1 Z_2}{M_c V_0^2} \tag{A.5}$$

and Z_1 is the impinging charge on a target atom of charge Z_2 at an impact parameter b.
The laboratory recoil angle a_R is related with the Coulomb deflection angle ϕ_{cm} and the impact parameter b through the relations :

$$a_R = \frac{\pi - \phi_{cm}}{2} = \pi/2 - \tan^{-1}(b_0/2b) \tag{A.6}$$

A.1 Doppler broadening and shift of $K\alpha_1$ X – Ray of Lanthanum excited during the bombardment with 403 MeV Nitrogen

For the system 403 MeV $N^{7+} \rightarrow$ La the projectile charge, mass and velocity are $Z_1 = 7, M_1 = 14$ amu, and $V_{proj} = 0.25\,c$ and the target charge and mass are $Z_1 = 57$ and $M_1 = 139$ amu. The reduced mass of the system is $M_c = 12.72$ amu. From Eq. (A.5) the minimum distance of approach b_0 is 1.54 fm. The laboratory recoil angle a_R according to Eq. (A.6) is given by: $a_R = \pi/2 - tan^{-1}(0.77/b)$, where b in fm.
For a typical values of the impact parameter b equal to 500 fm (see Fig. 5.6, page

65), the recoil angle is $a_R = 89.91°$. The target atom recoils almost perpedicular to the direction of the incoming projectile.

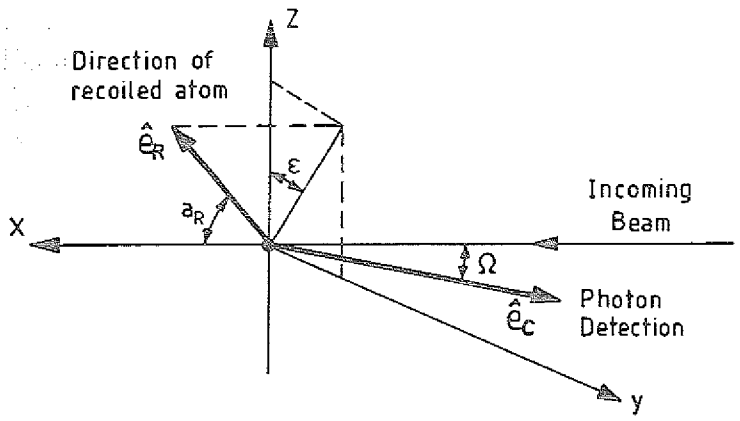

Figure A.2: *Schematical geometrical diagram for the evaluation of the Doppler effect.*

The geometry of the problem is shown in Fig. A.2. The direction of the recoiled target atom is defined from the recoil angle a_R and the azimuthal angle ϵ. The unitary recoil vector is given by:

$$\hat{e}_R = (\cos a_R)\,\hat{e}_x + (\sin a_R)\,(\sin \epsilon)\,\hat{e}_y + (\sin a_R)(\cos \epsilon)\hat{e}_z$$

and the unitary vector pointing from the atom to the crystal is given by:

$$\hat{e}_C = -(\cos \Omega)\,\hat{e}_x + (\sin \Omega)\hat{e}_y$$

where Ω is the angle between the beam and the target-crystal directions. The angle Ω during the experiment was $\simeq 70°$.

The angle θ between the recoil direction and the direction of observation is given by:

$$\cos(\theta) = \hat{e}_R \cdot \hat{e}_C = (\sin a_R)\,(\sin \Omega)\,(\sin \epsilon) - (\cos a_R)\,(\cos \Omega) \qquad \text{(A.7)}$$

For $a_R \simeq 90°$, in a first approximation Eq. (A.7) can be written :

$$\cos(\theta) \simeq (\sin \Omega)\,(\sin \epsilon)$$

and the energy shift ($E-E_0$) according to Eq. (A.2) will be:

$$E - E_0 \simeq E_0\,(V_R/c)\,(\sin \Omega)\,(\sin \epsilon) \qquad \text{(A.8)}$$

For $\epsilon = 0°$, $180°$ there is no Doppler shift, as the atom moves in direction perpedicular to the direction of observation, but for $\epsilon = 90°$, $270°$ the shift is maximum (the atom moves parallel to the observation direction.

The recoil velocity is equal to $V_R = 7.2 \cdot 10^{-5}\, c$, according to Eq. (A.3). The mean lifetime of a K hole in the atom of lanthanum is $4.7 \cdot 10^{-17}$ sec [Kr79b] and is very short compared to the recoil time of the atom ($\simeq 10^{-12}$sec). So, it is a quite reasonable to assume that the X-ray is emitted by the atom at the maximum recoil velocity V_R. Already the maximum recoil velocity is so small compared to the light velocity that only the first order term in the Doppler shift in Eq. (A.2) needs to be considered. Depending on the value of the azimuthal angle ϵ the energy shift ΔE is in the order of 10^{-4} of the photon energy at rest. This means that for transitions of about 30 KeV the energy shifts amount few eV.

To simulate the spectrum of the energy-shifted X-rays due to the Doppler effect, a Monte Carlo computer code has been developed. In general we have followed the procedure given in [Pe87, Do90].

For each projectile-target collision two parameters, are selected : the azimuthal angle ϵ and the impact parameter b.
The distribution of the azimuthal angle ϵ is directly generated from uniformly distributed random numbers.
The randomized impact parameter b_r is obtained from the integral equation:

$$\int_0^{b_r} P_K(b)\, b\, db = z_p \int_0^{\infty} P_K(b)\, b\, db \qquad \text{(A.9)}$$

where z_p is a random number uniformly distributed between 0 and 1. The ionization probabilities $P_K(b)$ for 403 MeV $N^{7+} \rightarrow$ La are those calculated from [Am91](see App. E). The product $P_K(b) \cdot b$ as function the impact parameter b is approximated by:

$$P_K(b) \cdot b = 0.743 \cdot 10^{-8} b^3 - 0.341 \cdot 10^{-4} b^2 + 0.041 \cdot b + 0.863 \qquad \text{(A.10)}$$

where the variable b takes values between 0 and 2400 fm. Using Eq. (A.10), the integral Eq. (A.9) is solved, and an impact parameter b is determined.

With the impact parameter b and the azimuthal angle ϵ defined, the laboratory recoil angle, the recoil velocity and the energy E of the emitted photon are calculated. Finally an event is stored in the energy channel corresponding to $E - E_0$.

Monoenergetic line profile

We consider a monoenergetic photon with an energy of E_0=33.44 KeV (the energy of the $K\alpha_1$ X-rays of lanthanum have the same value, but a Lorentzian profile), which is emitted during the bombardement of the lanthanum target with 405 MeV N^{7+}. The simulated spectrum of the emitted photons around the initial energy E_0 due to the Doppler effect is shown in Fig. A.3. An inspection of Eq. (A.8) shows that the energy is shifted to higher values for azimuthal angles $0° < \epsilon < 180°$, and is shifted to lower values for $180° < \epsilon < 360°$. But the center of the distribution stays constant within 1 meV.

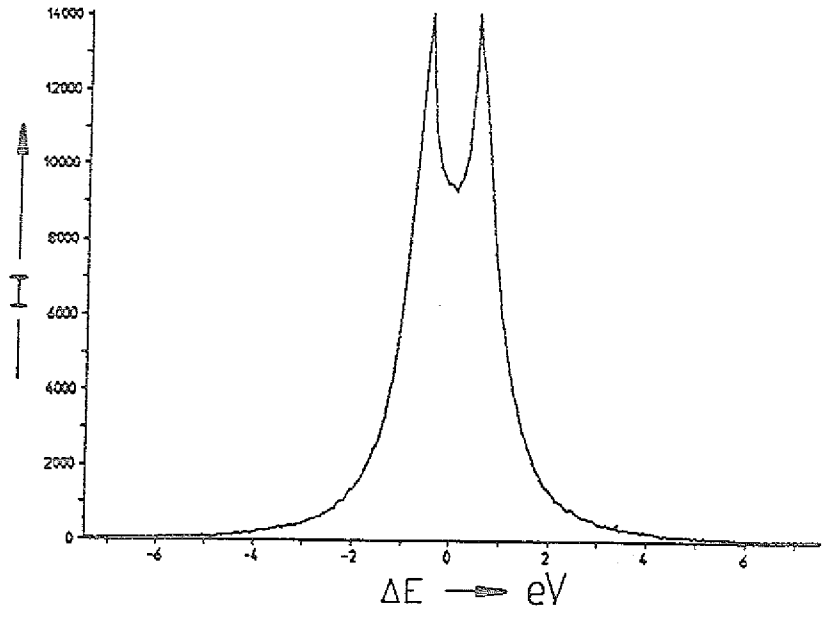

Figure A.3: *Energy spectrum of recoiling lanthanum atoms, emitting monoenergetic photons of energy 33.44 KeV, during the bombardement with 403 MeV $^{14}N^{7+}$. The Monte Carlo simulation calculated 500000 events.*

Next we give an interpretation the energy spectrum shape $I(E - E_0)$. Supposing that the number of the uniformly distributed events, in the azimuthal angle interval $(0° < \epsilon < 180°)$ is N_0 , the total number of recorded photons is given by :

$$\int_0^{\Delta E_{max}} I(E - E_0)\, d(E - E_0) = \epsilon_{eff} \frac{N_0}{\pi} \int_0^{\pi} d\epsilon \qquad \text{(A.11)}$$

where ϵ_{eff} is the overall efficiency of the spectrometer, which is supposed to be energy independent in the energy interval which we have measured.

Solving Eq. (A.11), with the help of Eq. (A.8), the spectral distribution $I(E - E_0)$ is given by:

$$I(E - E_0) = \frac{N_0}{\pi\, \epsilon_{eff}} \frac{1}{\sqrt{B^2 - (E - E_0)^2}} \qquad \text{(A.12)}$$

with $B = E_0\,(V_R/c)\,(\sin\Omega)$

For values of the impact parameter b equal to 200 fm and 500 fm the resulting $I(E - E_0)$ spectra are shown in Fig. A.4a,b, respectively.

X-ray line profile

In the case of emission of X-rays from recoiling atoms, the Doppler effect is taking into account, by folding the Lorentzian line profile of an X-ray with the obtained Doppler line profile calculated for a monoenergetic line.

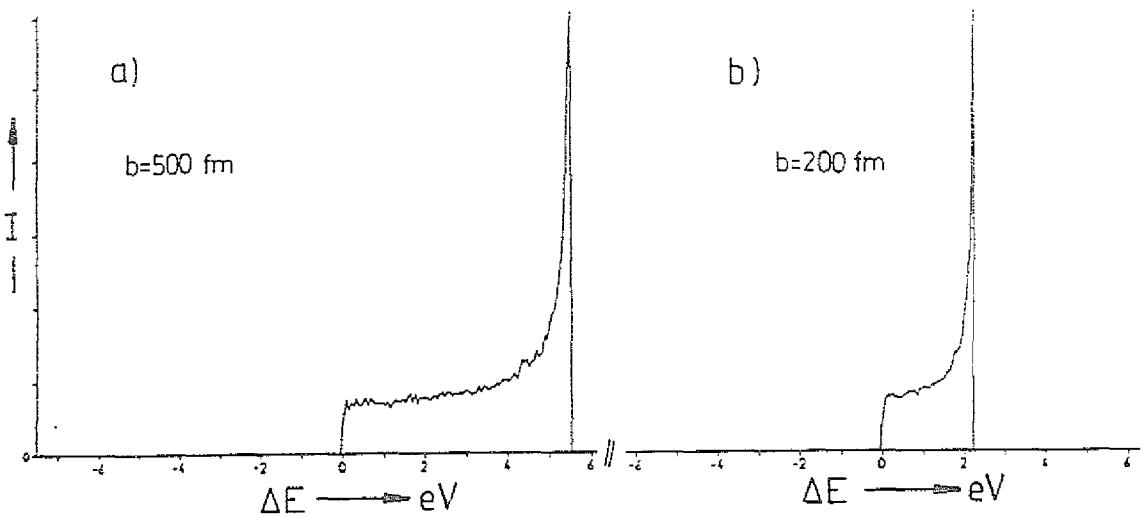

Figure A.4: *The Doppler spectra for* $0° < \epsilon < 180°$ *and for impact parameters a.) b=200fm and b.) b=500fm, for the present system.*

In the case that $K\alpha_1$ X-rays of La emitted during the bombardment with the 403 MeV N^{7+}, the measured line profile is given from the convolution of a Lorentzian distribution, of FWHM = 17.4 eV (corresponds to the lanthanum $K\alpha_1$ natural width [Kr79b]) with the monoenergetic line profile shown in Fig. A.3. The result of the folding is illustrated in Fig. A.5. The shape of the resultant line remains essentially unchanged.

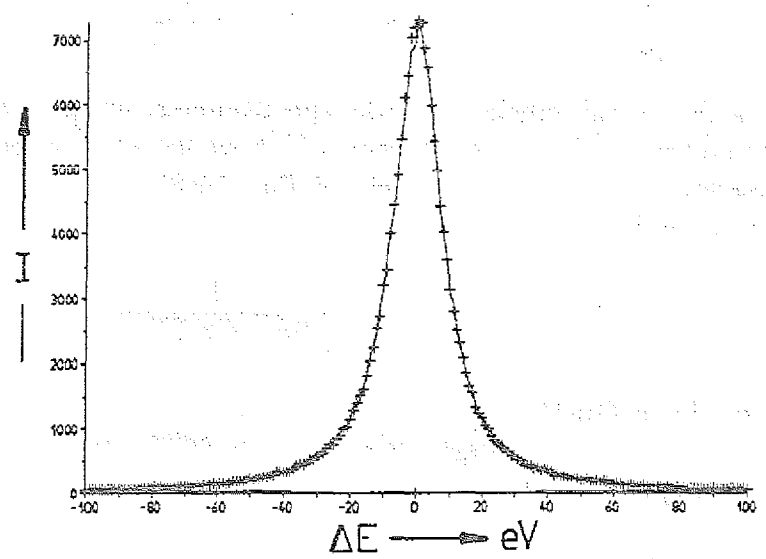

Figure A.5: $K\alpha_1$ *X-rays from lanthanum during the bombardement with 405 MeV* $^{14}N^{7+}$. *The Doppler effect has been included by folding the Lorentzian line profile of 17.4 eV width (marked with (+)), with the line profile of Fig. 3. The convolution is given by the continuous line.*

B. K level width and fluorescence yields of lanthanum, in the presence of an L spectator hole

The total K fluorescence yield $\omega_{K_{tot}}$ is defined as the probability that one K hole is filled through a radiative electron transition. The probability that the electron, which fills the K hole, originated from the $2p_{3/2}$ shell or from the $2p_{1/2}$ shell is called the $K\alpha_1$ fluorescence yield $\omega_{K\alpha_1}$ or the $K\alpha_2$ fluorescence yield $\omega_{K\alpha_2}$. The total K fluorescence yield can be expressed as the sum over all yields from the fluorescence channels, which fill the K hole :

$$\omega_{K_{tot}} = \omega_{K\alpha_1} + \omega_{K\alpha_2} + \omega_{K\beta_1} + \omega_{K\beta_3} + \omega_{K\beta} \qquad \text{(B.1)}$$

where $\omega_{K\beta_1}$,$\omega_{K\beta_3}$ and $\omega_{K\beta}$ are the fluorescence yields for the $K\beta_1$, $K\beta_3$ and all the K radiative transitions from higher than M shell, respectively. For singly ionized atoms these yields have been explicitly determined. As an example, for the singly ionized lanthanum atom the total K fluorescence yield is 0.906 [Le78]. This means that a K hole is filled mainly through a radiative transition. The partial K fluorescence yields are given by [Le78]:

$$\omega_{K\alpha_1}/\omega_{K\alpha_2}/\omega_{K\beta_1}/\omega_{K\beta_3}/\omega_{K\beta}/\omega_{K_{tot}} = 52.2/28.4/10.2/5.3/3.8/100 \qquad \text{(B.2)}$$

The situation is more complicated when the K transition takes place in the presence of additional vacancies. In this case, three problems have to be solved:

- i) What is the influence on the natural width Γ_K of K hole state when an additional L hole is present?
- ii) How much changes the total K fluorescence yield when an L spectator hole is present?
- iii) How much change the partial K fluorescence yields in the case of an L spectator hole?

In the following we will encounter these problems.

B.1 K transition rates in the presence of an L spectator hole

A double vacancy configuration may consist of many states with different total angular momentum, due to the angular momentum coupling between the holes. As

an example, we have calculated for lanthanum the allowed electric dipole transition probabilities for the $K\alpha_{1,2}$ and $K\beta_{1,3}$ transitions in the presence of one L spectator hole using the MCDF code of Desclaux [In91]. The results are listed in the Tables 5.13 of page 73.

The mean transition probability for a certain hole configuration is calculated as the average value of the transition probabilities of different total angular momentum states, supposing that the transitions take place statistically from these states. For the $K\alpha_{1,2}$, $K\beta_{1,3}$ and K_β of lanthanum, with or without L spectator hole, we give the result in Table B.1. As an example let us consider the average $K\alpha_1$ transition rate in the case of a L_I (2s) spectator hole. The total angular momentum J of the initial hole configuration 1s2s can be 0 or 1; consequently the mean transition rate $S_{K\alpha_1}$ will be :

$$S_{K\alpha_1} = [\frac{1}{4} \cdot 8.69 + \frac{3}{4} \cdot (2.30 + 8.64)] \cdot 10^{15}\, sec^{-1} = 11.23 \cdot 10^{15}\, sec^{-1}$$

Transition Rates	Position of L spectator hole			
in $10^{15}\, sec^{-1}$	No L	L_I	L_{II}	L_{III}
$S_{K\alpha_1}$	10.23	10.38	11.17	7.73
$S_{K\alpha_2}$	5.56	5.64	2.80	5.35
$S_{K\beta_1}$	1.90	1.93	1.92	1.93
$S_{K\beta_3}$	0.98	0.99	0.99	0.99
$S_{K\beta}$	0.69	0.69	0.69	0.69
S_{Rad}	19.36	19.63	17.57	16.69

Table B.1: *K radiative transition rates of lanthanum with or without the presence one L spectator hole.*

In order to calculate radiative and nonradiative transitions rates in multionized atoms F.P.Larkins [La71] has proposed an approximate scaling procedure starting from the transition rates of singly ionized. The radiative transition rate is proportional to the product of oscillator strength and the square of the transition energy. According to this procedure the oscillator strength is reduced by n/n_0. If the energy differences are known, one can take into account their effect on the radiative transition rate. If there are n electrons in a shell that can contain n_0 electrons the Auger transition rate for that shell is reduced from its full-shell value by n/n_0 if the transition involves one electron and by $n(n-1)/n_0(n_0-1)$ if it involves two electrons from the partially filled shell.

If we use Larkin's scaling procedure to estimate the K radiative transition rates, for La with one L spectator hole, the results are very similar to values listed in Table B.1.

Transition Rates	Ba (Z=56)				Nd (Z=60)			
	Position of L spectator hole				Position of L spectator hole			
$\times 10^{15}\, sec^{-1}$	No L	L_I	L_{II}	L_{III}	No L	L_I	L_{II}	L_{III}
$S_{K\to L_I,L_I}$	0.16	0.00	D	D	0.18	0.00	D	D
$S_{K\to L_I,L_{II}}$	0.20	0.10	D	D	0.23	0.12	D	D
$S_{K\to L_I,L_{III}}$	0.23	0.11	D	D	0.24	0.12	D	D
$S_{K\to L_I,X}$	0.19	0.09	D	D	0.21	0.11	D	D
$S_{K\to L_{II},L_{II}}$	0.02	D	0.00	D	0.02	D	0.00	D
$S_{K\to L_{II},L_{III}}$	0.49	D	0.24	D	11.95	D	0.25	D
$S_{K\to L_{II},X}$	0.16	D	0.08	D	0.18	D	0.09	D
$S_{K\to L_{III},L_{III}}$	0.24	D	D	0.12	0.24	D	D	0.12
$S_{K\to L_{III},X}$	0.27	D	D	0.20	0.29	D	D	0.22
$S_{K\to XY}$	0.06	D	D	D	0.65	D	D	D
S_{Auger}	2.02	1.55	1.68	1.84	2.16	1.63	1.85	1.96

Table B.2: *K Auger transition rates for Ba and Nd. D denotes the same value as the diagram value (no L). X and Y denote final states in shells higher than the L.*

For the nonradiative K transitions rates, with one L spectator hole Larkins' scaling procedure has been used. There exist no data for La, but the Auger transition rates for singly K ionized Ba and Nd atoms could be extracted from the tables of [Ch79]. They are listed in Table B.2. The Auger transition rates for La are obtained as linear interpolation between the Ba and the Nd values.

B.2 K level width

The values for the total K radiative, S_{Rad}, and Auger, S_{Auger}, transition rates from Tables B.1,2 are summarized in Table B.3. Also the total K transition rates are listed.

As can be seen the probability for filling the K-hole is reduced in the presence of a L_{II} or a L_{III} spectator hole, which means a prolonged life time for this K hole state.

The natural width Γ_K has been calculated from the total K transition rate S_{tot}, as $\Gamma_K = S_{tot}\hbar$. For the natural width of the K level in singly K ionized La we obtain 14.1 eV (see Table B.3). The semi-empirical value given by [Kr79b] has the same value with an estimated uncertainty of 4%. In the precence of a L_I spectator hole the natural width of the K level stays unchanged (14.0 eV) whereas in the case of L_{II} and L_{III} spectator hole it is reduced to 12.7 and 12.2 eV respectively. Consequently the K level width reduction can be as large as 13% due to a L_{III} spectator hole.

Spectator hole	K Transition Rates $\times 10^{15} sec^{-1}$			$\omega_{K_{tot}}$	Γ_K in eV
	S_{Rad}	S_{Auger}	S_{tot}		
No L	19.36	2.06	21.42	0.904	14.1
L_I	19.63	1.57	21.20	0.926	14.0
L_{II}	17.57	1.71	19.28	0.911	12.7
L_{III}	16.69	1.87	18.56	0.899	12.2

Table B.3: *K transition rates, total K fluorescence yield, and K level width of lanthanum (1 eV=1.519 $\cdot 10^{15}$ h/sec).*

B.3 Total K fluorescence yield

The total K fluorecence yield $\omega_{K_{tot}}$ is given from:

$$\omega_{K_{tot}} = \frac{S_{Rad}}{S_{Rad} + S_{Auger}} \tag{B.3}$$

where S_{Rad} and S_{Auger} are the radiative and Auger transition rates to fill the K hole.

Thus, the total K fluorescence yield for a single K ionized atom equals to 0.904 in very good agreement with the published value [Le78]. For La the total K fluorescence yield in the presence of a L spectator hole does not change more than 3% (see Table B.3). The influence of higher shell spectator hole on the fluorescence yield is expected to be even smaller. This conclusion is obviously valid also for heavier atomic systems than La.

B.4 Partial K fluorescence yields

The partial fluorescence yield ω_{Ki} is given from:

$$\omega_{Ki} = \frac{S_{Ki}}{S_{Rad}} \tag{B.4}$$

For the singly K ionized atom, the partial fluorescence yields of the diagram lines as listed in Table B.4, are in good agreement with the yields given by Eq. (B.2). In the presence of one L spectator hole significant changes show up. They are larger in the $K\alpha$ than in $K\beta$ transitions, as the L shell electrons participate directly in $K\alpha$ transitions.

As an example, let us discuss, the fluorescence yield of the $K\alpha_1$ transition. This yield is constant in the case of a L_I spectator hole; it is increased by 21% in case of a L_{II} hole with respect to the diagram line, and it is reduced by 12% in case of a L_{III} spectator hole. To give a qualitive argument in the case of a $2p_{3/2}$ spectator hole, we should keep in mind that the $K\alpha_1$ fluorescence yield is

Fluorescence yield	Position of L spectator hole			
	No L	L_I	L_{II}	L_{III}
$\omega_{K\alpha_1}$	52.8	52.9	63.6	46.3
$\omega_{K\alpha_2}$	28.7	28.7	15.9	32.1
$\omega_{K\beta_1}$	9.8	9.8	10.9	11.6
$\omega_{K\beta_3}$	5.1	5.0	5.6	5.9
$\omega_{K\beta}$	3.6	3.5	3.9	4.1
$\sum_i \omega_{Ki}$	100.	100.	100.	100.

Table B.4: *Partial fluorescence yields, normalized to 100.*

expected to be reduced, as the number of electrons available for the transition to the K shell has been reduced from 4 to 3. A spectator hole in the $2p_{1/2}$ subshell influences the $K\alpha_1$ fluorescence yield in a more indirect way. A $2p_{1/2}$ spectator hole will reduce the yield of the $K\alpha_2$ transition, as the number of electrons available for the transition to the K shell is reduced from 2 to 1. The reduction of the $K\alpha_2$ channel has as consequense an enchancement of the other radiative channels as the total K fluorescence yield has been found constant. Therefore spectator holes in subshells which are not involved directly in a transition, will influence the fluorescence yield of this transition. The change of the partial fluorescence yields are negligible in the case of a 2s spectator hole, as radiative dipole transitions from 2s are almost forbitten. The 2s electrons can fill radiatively a K hole only through a M1 transition but its rate is about 4 orders of magnitude smaller than the $K\alpha_1$ rate [Sc74].

These results show that the partial fluorescence yields may change considerably in the precence of one L spectator hole in different subshells. A L_{II} spectator hole can decrease the ratio $\omega_{K\alpha_2}/\omega_{K\alpha_1}$ from 0.54 to 0.25, a factor more than 2. This is important for a comparison of $K\alpha_1$ and $K\alpha_2$ transitions in the presence of a spectator hole. The L_{II} spectator hole increaces the $K\alpha_1$ transition rate by 20% relative to the $K\alpha_1$ diagram transition rate. These changes have to be taken into account for a correct interpetetion of the X-ray satellite spectra.

With the same arguments, the changes of the yields for other transitions can be explained. It is noteworthy that a spectator hole in the L_{II} or L_{III} shell has an influence on the K_β yields.

In order to estimate the partial fluorescence yields we have developed a semi–empirical formula. As an example the $K\alpha_1$ partial fluorescence yield, in the case of a spectator hole in the L_x subshell can be written as :

$$\omega_{K\alpha_1}(L_x) = \frac{\omega_{K\alpha_1}(1-\frac{n_{L_{III}}}{4})}{\omega_{K\alpha_1}(1-\frac{n_{L_{III}}}{4})+\omega_{K\alpha_2}(1-\frac{n_{L_{II}}}{2})+\omega_{K\beta_1}+\omega_{K\beta_3}+\omega_{K\beta}} \qquad \text{(B.5)}$$

where $\omega_{K\alpha_1}$, $\omega_{K\alpha_2}$, $\omega_{K\beta_1}$, $\omega_{K\beta_3}$ and $\omega_{K\beta}$ are the partial fluorescence yields for a singly K ionized atom, $n_{L_{III}}$ and $n_{L_{II}}$ are the number of spectator holes in the corresponding subshells. For the case of a $K\alpha_2$ transition the nominator must read $\omega_{K\alpha_2}(1-n_{L_{II}}/2)$ and in the case of a $K\beta_1$ transition it should be $\omega_{K\beta_1}$. Using the values for the partial fluorescence yields of a singly K ionized lanthanum atom from Table B.4, the partial fluorescence yields for $K\alpha_{1,2}$ and $K\beta_{1,3}$ transitions in the presence of one L spectator hole have been calculated with the help of Eq. (B.5). The results are listed in Table B.5.

Fluorescence	Position of L spectator hole			
yield	No L	L_I	L_{II}	L_{III}
$\omega_{K\alpha_1}$	52.8	52.8	61.6	45.6
$\omega_{K\alpha_2}$	28.7	28.7	16.8	33.1
$\omega_{K\beta_1}$	9.8	9.8	11.4	11.3
$\omega_{K\beta_3}$	5.1	5.1	6.0	5.9
$\omega_{K\beta}$	3.6	3.6	4.2	4.1
$\sum_i \omega_{Ki}$	100.	100.	100.	100.

Table B.5: *Partial fluorescence yields of lanthanum in the presence of a L spectator hole according to the Eq. (B.4) The starting point was the singly ionized atom partial fluorescence yields from Table B.4.*

Comparing the results from Tables B.4 and B.5 we find a very good agreement. The deviations are less than 4%.

The mean fluorescence yield $\overline{\omega_{K\alpha_1}}$ of a $K\alpha_1$ transition, with one spectator hole in any L sub-shell, is given by:

$$\overline{\omega_{K\alpha_1}} = \sum_{L_x} P_{L_x} \times \omega_{K\alpha_1}(L_x) \qquad \text{(B.6)}$$

where the sum runs over all the L sub-shells, P_{L_x} is the probability that the spectator hole will be in the sub-shell L_x and $\omega_{K\alpha_1}(L_x)$ is the $K\alpha_1$ fluorescence yield in the presence of spectator hole in subshell L_x.

Using Eq.(B.6) and the partial fluorescence yields from Table B.4 the mean fluorescence yields of $K\alpha_1$, $K\alpha_2$ and their ratio have been calculated, for five different ratio distributions (Table B.6). The first line contains the diagram transitions (no spectator), the second assumes a statistical hole distribution and the others are possible to be created during ion- atom collisions.

In the presence of a L spectator hole the partial $K\alpha_1$ and $K\alpha_2$ fluorescence yields and their ratio change drastically compared to values for diagram transitions. The changes increase with the deviation of the ratio $P_{L_{II}}/P_{L_{III}}$ from the statistical

$P_{L_I} : P_{L_{II}} : P_{L_{III}}$	$\overline{\omega_{K\alpha_1}}$	$\overline{\omega_{K\alpha_2}}$	$\overline{\omega_{K\alpha_2}}/\overline{\omega_{K\alpha_1}}$
0 : 0 : 0	52.8	28.7	0.54
1 : 1 : 2	52.3	27.2	0.52
1 : 2 : 4	52.2	27.0	0.52
1 : 1 : 1	54.3	25.6	0.47
1 : 1 : 4	50.3	28.8	0.57

Table B.6: *Mean partial fluorescence yields of* $K\alpha_1$ *and* $K\alpha_2$ *transitions and their ratio, for different spectator distribution probabilities* $P_{L_I} : P_{L_{II}} : P_{L_{III}}$

value 1/2. This underlines the importance of a careful investigation of the partial fluorescence yields for the interpretation of the K X-ray satellite spectra, but also the necessity of theoretical knowledge of the ionization probabilities.

A further investigation has to be done for the cases with more than one L spectator or in the presence of M spectator holes. We suggest an extension of Eq. B.4 which reads for example in the $K\alpha_1$ transition :

$$\omega_{K\alpha_1}(L_x) = \frac{\omega_{K\alpha_1}(1-\frac{n_{L_{III}}}{4})}{\omega_{K\alpha_1}(1-\frac{n_{L_{III}}}{4})+\omega_{K\alpha_2}(1-\frac{n_{L_{II}}}{2})+\omega_{K\beta_1}(1-\frac{n_{M_{III}}}{4})+\omega_{K\beta_3}(1-\frac{n_{M_{II}}}{2})+\omega_{K\beta}} \quad \text{(B.7)}$$

in order to include spectator holes in the M subshells.

C. Target properties

C.1 Effective projectile penetration depth

The effective target depth from which the emitted photons are not self-absorbed is determined by the quantity $1/\mu$, where μ is the linear attenuation coefficient. The values of μ in the case of lanthanum, tantalum and uranium targets and for photon energies equal to the $K\alpha_1$ energies of the corresponding targets (33.4 KeV for lanthanum, 57.5 KeV for tantalum and 98.4 KeV for uramium), are 49.46, 66.29 and 37.50 cm^{-1} [Ve73], respectively.

An inspection of Fig. C.1 shows that a projectile can penetrate into the target by an effective penetration depth X_{eff}, until the projection to the photon observation direction equals to $1/\mu$. The two quantities are connected through :

$$X_{eff} = \frac{1}{\mu} \frac{\sin\omega}{\sin(180° - \theta - \omega)} \tag{C.1}$$

where θ is the angle between the incoming beam and the photon detection direction and ω the angle between the photon detection direction and the target surface. During the experiment these angles were $\theta \simeq 70°$ and $\omega < 2°$.

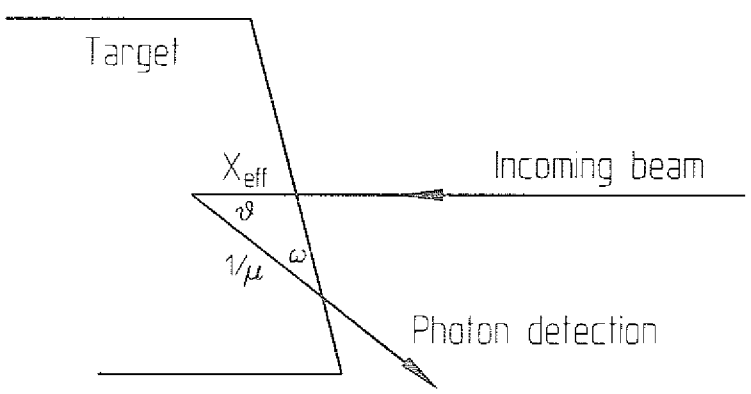

Figure C.1: *Geometry of X-ray emission from the target, induced from the incoming ion beam*

.

The values of the effective penetration depth X_{eff} for $\omega_{max} = 2°$ for the La, Ta and U targets are 7.4, 5.5 and 9.8 μm respectively.

The effective depth in all the cases is not more than 10 μm.

C.2 Mean energy loss of the projectile

In Table C.1 the mean energy loss and the mean range of the projectiles passing through the targets have been calculated from [Zi80,An80]. The mean range corresponds to the thickness at which roughly the particles are absorbed. The targets are assumed to be amorphous with the natural abundance of isotopes.

Colliding system	Mean energy loss *in MeV/μm*	Total energy loss *in MeV*	Mean range *in mm*
403 MeV N^{7+} → La	0.17	1.3	0.81
350 MeV N^{7+} → Ta	0.80	4.4	0.25
500 MeV Ne^{10+} → Ta	1.66	7.3	0.20
500 MeV Ne^{10+} → U	1.71	16.7	0.18

Table C.1: *Mean and total energy loss and the mean range of the projectiles passing through the targets.*

Also the total energy loss is given in Table C.1. It can be seen that in all the cases the decrease of the initial projectile kinetic energy is less than 3%.

Consequently the projectile's energy can be considered constant within the effective projectile penetration depth.

D. Background contributions

D.1 δ – electrons

Fast moving electrons in the target can excite inner shell electrons and consequently enchance the intensity under the diagram line, as the probability for multionization due to the electron impact is low, like for protons.

Consider a projectile with a charge Z_1 and velocity β (relative to the speed of light c) passing through a material of density p which consists of atoms with atomic and mass number Z_2 and A_2, respectively. Due to the Coulomb interaction between the projectile and the atomic electrons, electrons are ejected with an energy E that can have a value up to a maximum energy E_{max}. If these so – called δ – electrons have energies higher than the K – shell binding energies of the target atoms, they can remove a K – shell electron, and consequently is probable that a K X – ray follows. Assuming that the initial electron is free and at rest, the maximum energy E_{max} is transferred in a head – on collision, and in first approximation using two – body relativistic kinematics, is given by:

$$E_{max} = 2\,m\,c^2\,\frac{\beta^2}{(1-\beta^2)} \tag{D.1}$$

where $m\,c^2$ is the rest energy of the electron.

The probability for an electron to be ejected with a certain energy E is given approximately by [Sa77, p.4]:

$$P(E) = K\,Z_1^2\,\frac{Z_2}{A_2}\,\frac{p}{b^2}\,\frac{X}{E^2} = \frac{W}{E^2} \tag{D.2}$$

where K = 0.154 MeV gr^{-1} cm^{-2}, and X is the thickness of the target.
Integration of Eq. (C.5) gives an expression for the number of δ – electrons having an energy E in the energy interval between E_1 and E_2 :

$$N(E_2 > E > E_1) = \int_{E_1}^{E_2} P(E)\,dE = W\,(1/E_1 - 1/E_2) \tag{D.3}$$

where $W = K\,Z_1^2\,(Z_2/A_2)\,(p/b_2)\,X$.

In our case the projectiles of the incoming beam are $^{14}N^{6+}$ and $^{20}Ne^{8+}$, with energies of 29. and 25. MeV/nucleon, respectively. Their velocities are 0.243 c and 0.226 c respectively. With these initial velocities the maximum energy E_{max} transferred to δ – electrons is 64.0 KeV and 55.0 KeV respectively.

For the combinations of projectiles and targets which we studied only in the case of 403 MeV $N^{6+} \rightarrow$ La the ejected δ-electrons can remove a K shell electron from neighbouring atoms. The maximum energy of the ejected δ-electrons is E_{max}= 64.0 KeV and the binding energy for the K electrons of lanthanum is $E_{K,bind}$ =38.9 KeV.
The number of δ-electrons ejected per projectile within the energy interval between $E_1 = E_{K,bind}$ and $E_2 = E_{max}$, with Z_1=7, Z_2=57, A_2 = 139, p=6.166 gr·cm^{-3}, b=0.243 is given by:

$$N = 0.31 \cdot X \cdot electrons/\mu m$$

For X = 7.4 μm (see Table C.2) the number of the ejected δ- electrons, in this energy interval, is N = 2.3 .

The cross section, for lanthanum K-shell ionization during the impact of 2 MeV electrons is 19 barns [Lo90]. In the present case the δ-electrons have energies just above the threshold. In order to have an estimation of the cross-section for K-shell ionization near to threshold and especially in the region $1 < U_K < 2.5$ we used the following empirical equation as given by [Sh81]:

$$\sigma_K = 7.92 \cdot 10^{-20} \frac{\ln(U_K)}{U_K\, E^2_{K,bind}}\, cm^2 \cdot KeV^2 \qquad \text{(D.4)}$$

where $U_K = E^{elec}_{imp}/E_{K,bind}$ is the ratio of the electron impact energy to the target electron binding energy (or ionization energy).
In our case the mean electron impact energy is $\overline{E^{elec}_{imp}}$ = 48.4 KeV [$\overline{E^{elec}_{imp}} = (2 \cdot E_1 \cdot E_2)/(E_1 + E_2)$ as the electron distribution $\propto 1/E$ according to Eq. (C.3)]. With the K binding energy $E_{K,bind}$ = 38.9 KeV, the ratio U_K is equal to 1.24 and from Eq. (C.4) we obtain the cross section for K-shell electron ionization to be σ_K = 9.2 barns.
Taking into account that 2.3 δ-electrons per incoming projectile are released, the total cross- section for ejection of a K shell electron by δ-electrons per projectile is 21. barns.
The direct Coulomb cross section for the lanthanum K shell electrons, without the simultaneous ejection of L electron has been estimated to be $\simeq$ 1100 barns, in the case of 403 MeV $N^{7+} \rightarrow$ La. Consequently the maximum contribution of the ejected δ-electrons in the creation of singly ionized K states is in the order of 2%.

Another mechanism which can contribute to the diagram line is due to the electrons following the projectile. These electrons if they have energies higher than the K-shell binding energies of the target atom can ionize the K shell and a K X-ray may follow. The energies of the electron following projectiles which have kinetic energies of 29. and 25. MeV/nucleon, are 15.8 KeV and 13.6 KeV, respectively. These energies are lower than the K binding energy of lanthanum, which is the lightest of the elements which we studied.

D.2 Nuclear Coulomb excitation

Another mechanism which can lead to the enhancement of the intensity of the diagram line is the nuclear Coulomb excitation, followed by internal conversion of the γ-rays. When heavy nuclei are bombarded with charged paricles with an energy below the Coulomb barrier the short range nuclear forces cannot operate. The collision may, however, give rise to nuclear excitations through the electromagnetic field of the impinging charged particles [Ad66]. The emission of a γ-ray is usually the most common mode of nuclear de-excitation, but it might accompanied by internal conversion. In this process, the nuclear excitation energy is directly transferred to an atomic electron rather than emitted as photon. A K-shell electron can be ejected and during the refilling of the K vacancy from electrons of the higher shells, a K X-ray will be emitted.

Detailed study of the Coulomb excitation process for Ta as target has been done, since it is known to have a large nuclear quadrupole moment, and the Coulomb excitation process has been observed [Ad66].

The energy $E_{barrier}$ of the Coulomb barrier is given by :

$$E_{barrier} = \frac{Z_1 \cdot Z_2 \cdot e^2}{R} = 1.44 \frac{Z_1 \cdot Z_2}{R} MeV \qquad \text{(D.5)}$$

where R is the effective radius of interaction which can be written as $R = R_1 + R_2$, R_1 and R_2 are the radii of the projectile and target nuclei. In the case of 350 MeV $N^{7+} \rightarrow$ Ta, the root-mean-square of the charge distribution of the ^{14}N is 2.56 fm and for ^{181}Ta is 5.48 fm [Ja74] and the Coulomb barrier is $E_{barrier} = 91.5$ MeV. Consequently the projectile's energy is well above the Coulomb barrier and during a head-on collision the projectile will pass through the nucleus and nuclear reactions will take place.

But as long as the projectile orbits can be described in the classical approximation, particles passing outside the nucleus are scattered into angles less than a critical angle θ_c [Ad56,Ad66], which depends on the ratio $x = E/E_{barrier}$ between the projectile energy E and the Coulomb barrier $E_{barrier}$ and is given by :

$$\theta_c = 2 \sin^{-1}\left(\frac{1}{2x-1}\right) \qquad \text{(D.6)}$$

For the 350 MeV $^{14}N^{7+} \rightarrow ^{181}$ Ta, we find x$\simeq$3.8 and $\theta_c \simeq 17°$. Thus, when the scattering angle is less than θ_c, the projectile has not passed the nucleus and the Coulomb excitation of the target nucleus becomes possible.

The differential cross section $d\sigma_\theta(E2)$ for Coulomb excitation of a given level of nuclei, in the case of quadrupole excitation, is given by [Ad66] :

$$d\sigma_\theta(E2) = C_{E2} \cdot (E - \Delta E') \cdot B(E2) \cdot df_{E2}(\theta, n_i, \xi)/dQ \; barns \qquad \text{(D.7)}$$

where :
θ is the deflection angle in the center-of- mass system,

E is the energy of the incident projectile in MeV,
ΔE is the level excitation energy in MeV,
$C_{E2} = 4.819 \cdot (1 + A_1/A_2)^{-2} \cdot A_1/Z_2^2\, barns$,
$\Delta E' = (1 + A_1/A_2) \cdot \Delta E$,
B(E2) the nuclear quadrupole moment in $e^2 \cdot barns^2$,
$df_{E2}(\theta, n_i, \xi)/dQ$ is the classical differential Coulomb excitation function for E2 excitation, with:
$\mathrm{dQ} = 2\,\pi \sin(\theta)$,
$n_i = \frac{Z_1 \cdot Z_2}{2} \sqrt{\frac{A_1}{10.008 \cdot E}}$,
$\xi = 2\frac{\sqrt{z}}{\nu} \cdot [(1-z)^{-1/2} - 1]$
$\nu = \frac{4}{Z_1 \cdot Z_2} \sqrt{\frac{10.008 \cdot \Delta E'}{A_1}}$
$z = \Delta E'/E$.

For the present system we have Z_1=7, A_1=14, E=350 MeV and Z_2 = 73, A_2 = 181. Applying the above Eqs. for the first excitation level of the ^{181}Ta nucleus, which is equal to 0.136 MeV we get : $C_{E2} = 1.09 \cdot 10^{-2} b$. The nuclear quadropole moment is $B(E2) = 2.1 e^2 \cdot barns^2$ [Nuclear Data Sheets 43, 289(1984)]. The classical differential Coulomb excitation function for E2 excitation for angles from zero until θ_c has been found by integration of $df_{E2}(\theta, n_i, \xi)$ in this interval :

$$df_{E2}(\theta_c > \theta > 0°, n_i, \xi) = \int_0^{\theta_c} [df_{E2}(\theta, n_i, \xi)/dQ].dQ$$

using the values from Table II.8, of [Ad66]. The result for $df_{E2}(\theta_c > \theta > 0, n_i, \xi)$ after numerical integation has been found 0.071.
The cross-section for Coulomb excitation of the ^{181}Ta nucleus to the energy level .136 MeV is $\sigma(E2) = 0.57$ barns, considering scattering angles between 0°and 17°. This cross section is less than 0.3% of the cross section for direct Coulomb ionization of K- shell electron (without simultaneous L electron ionization). The γ-ray conversion coefficient for electrons ejected from the K-shell is a(K)=1.382. In the same way the cross-section for excitation to the level .302 MeV has been found 0.14 barn.

Consequently the contribution of the nuclear Coulomb excitation to the intensity of the diagram lines is negligible.

E. Tables

E.1 403 MeV N^{7+} → La

Impact parameter in *fermi*	Ionization probabilities per subshell ($\times 10^{-4}$)								
	K	L_I	L_{II}	L_{III}	M_I	M_{II}	M_{III}	M_{IV}	M_V
100	411	496	854	1624	532	834	1642	1755	2604
200	389	490	853	1622	530	833	1641	1755	2605
300	358	481	849	1618	527	831	1639	1755	2605
400	323	470	845	1613	524	829	1636	1756	2606
500	287	457	840	1607	520	826	1633	1756	2607
600	252	444	834	1599	515	823	1628	1757	2608
700	220	431	827	1591	510	819	1623	1758	2609
800	191	419	819	1581	505	815	1617	1758	2610
900	165	409	810	1571	501	810	1611	1759	2612
1000	142	399	801	1559	496	805	1603	1760	2614
1100	122	391	791	1546	492	799	1595	1762	2616
1200	105	384	781	1533	488	793	1587	1763	2618
1300	90	378	770	1518	484	787	1577	1764	2620
1400	77	373	758	1503	481	780	1567	1766	2622
1500	66	369	747	1487	478	773	1556	1767	2625
1600	56	366	734	1470	476	766	1545	1769	2628
1700	47	363	722	1452	473	758	1533	1771	2631
1800	40	361	709	1433	471	750	1521	1772	2633
1900	34	360	696	1413	469	742	1508	1774	2636
2000	29	358	683	1393	467	733	1494	1776	2640
2100	24	357	669	1371	464	725	1480	1778	2643
2200	21	356	656	1350	462	716	1465	1780	2646
2300	18	355	642	1327	460	707	1451	1782	2649
2400	15	354	628	1304	457	698	1435	1784	2653

Table E.1: *Impact parameter dependent direct ionization probabilities for removing one arbitrary electron from K, L and M shells as calculated by [Am91].*

Impact parameter in *fermi*	Ionization probabilities per subshell ($\times 10^{-4}$)								
	K	L_I	L_{II}	L_{III}	M_I	M_{II}	M_{III}	M_{IV}	M_V
100	414	404	458	824	238	226	416	424	630
200	390	400	456	820	236	226	416	424	630
300	360	392	454	820	236	224	416	424	630
400	326	382	454	820	234	224	416	424	630
500	290	372	452	816	230	224	416	424	630
600	256	362	448	816	228	224	416	424	630
700	224	350	446	816	226	222	416	424	630
800	196	340	444	812	222	222	416	428	630
900	170	328	440	808	220	222	412	428	630
1000	148	318	436	808	216	220	412	428	630
1100	128	308	432	804	212	220	412	428	630
1200	110	300	428	800	210	218	408	428	630
1300	95	290	424	796	206	218	408	428	630
1400	82	282	420	788	204	216	408	428	630
1500	71	276	414	784	200	214	404	428	636
1600	61	268	410	780	197	214	404	428	636
1700	52	262	404	772	194	212	400	428	636
1800	45	256	398	764	191	210	398	432	636
1900	38	250	392	756	189	208	395	432	636
2000	32	246	386	748	186	206	393	432	636
2100	28	242	380	740	183	204	390	432	636
2200	24	236	374	732	180	202	387	432	636
2300	20	232	368	720	177	200	384	432	636
2400	17	228	360	712	175	198	381	432	636

Table E.2: *Impact parameter dependent direct ionization probabilities for removing one arbitrary electron from K, L and M shells as calculated using the SCA version of [Tr80].*

Impact parameter in *fermi*	Subshell coupling correction factor			Capture probabilities per subshell $\times 10^{-4}$		
	L_I	L_{II}	L_{III}	L_I	L_{II}	L_{III}
100	1.014	.947	.954	42.8	46.9	93.8
200	1.014	.947	.954	42.5	46.4	92.7
300	1.014	.947	.954	42.1	45.7	91.3
400	1.014	.947	.954	41.6	44.9	89.8
500	1.014	.947	.954	41.0	44.0	87.9
600	1.014	.947	.954	40.2	42.9	85.8
700	1.014	.947	.954	39.4	41.7	83.4
800	1.014	.947	.954	38.4	40.2	80.4
900	1.014	.947	.954	37.2	38.6	77.3
1000	1.014	.947	.954	36.0	37.0	74.1
1100	1.014	.947	.954	34.6	35.3	70.6
1200	1.014	.947	.954	33.2	33.6	67.1
1300	1.014	.947	.954	31.8	31.7	63.4
1400	1.014	.947	.954	30.3	29.9	59.8
1500	1.014	.947	.954	28.7	28.1	56.1
1600	1.014	.947	.954	27.1	26.3	52.6
1700	1.014	.947	.954	25.5	24.6	49.2
1800	1.014	.947	.954	23.9	23.0	46.0
1900	1.014	.947	.954	22.3	21.4	42.9
2000	1.014	.947	.954	20.7	20.0	39.9
2100	1.014	.947	.954	19.0	18.6	37.2
2200	1.014	.947	.954	17.5	17.3	34.5
2300	1.014	.947	.954	16.1	16.0	32.1
2400	1.014	.947	.954	14.7	14.8	29.7

Table E.3: *Impact parameter dependent subshell correction factors for the L-subshells [Ja91] and capture probabilities of an L shell target electron by the K shell of the projectile according to the SPB [Ja91].*

E.2 350 MeV N^{7+} → Ta

Impact parameter in *fermi*	Direct ionization probabilities per subshell ($\times 10^{-4}$)								
	K	L_I	L_{II}	L_{III}	M_I	M_{II}	M_{III}	M_{IV}	M_V
0	210	331	730	1386	520	776	1626	1962	2899
100	199	327	729	1385	518	776	1625	1962	2899
200	172	318	725	1381	515	773	1622	1962	2899
300	142	306	719	1374	510	770	1618	1961	2899
400	114	292	710	1365	503	765	1612	1961	2899
500	89	279	699	1354	496	759	1604	1961	2899
600	69	269	687	1341	490	752	1595	1960	2898
700	53	261	673	1325	483	745	1584	1959	2898
800	41	256	658	1308	478	736	1572	1959	2898
900	31	253	642	1289	474	726	1559	1958	2898
1000	23	252	624	1268	470	716	1544	1957	2897
1100	18	253	607	1245	467	706	1528	1956	2897
1200	13	256	588	1221	465	695	1511	1956	2897
1300	10	260	569	1196	463	683	1493	1955	2897
1400	8	264	550	1169	461	672	1474	1954	2897
1500	6	269	530	1141	459	660	1454	1953	2897
1600	4	273	510	1111	457	648	1433	1952	2897
1700	3	278	491	1082	455	636	1411	1951	2897
1800	2	282	471	1051	453	624	1389	1950	2896

Table E.4: *Impact parameter dependent direct ionization probabilities for removing one arbitrary electron from K, L and M shells as calculated by [Am91].*

Impact parameter in *fermi*	Ionization probabilities per subshell ($\times 10^{-4}$)			
	K	L_I	L_{II}	L_{III}
100	204	300	520	902
200	178	291	517	900
300	148	279	512	895
400	120	265	506	890
500	95	252	497	882
600	74	241	489	875
700	56	230	479	865
800	44	222	469	856
900	34	216	459	843
1000	29	211	446	832
1100	18	207	432	820
1200	15	205	421	805
1300	12	204	409	790
1400	9	203	396	774
1500	6	204	383	759
1600	5	204	370	741
1700	5	204	357	720
1800	2	204	344	705

Table E.5: *Impact parameter dependent direct ionization probabilities for removing one arbitrary electron from K and L shells as calculated using the SCA version of [Tr80].*

Impact parameter in *fermi*	Subshell coupling correction factor			Capture probabilities per subshell ($\times 10^{-4}$)		
	L_I	L_{II}	L_{III}	L_I	L_{II}	L_{III}
100.	.924	.857	.887	6.0	46.8	93.7
200.	.923	.858	.886	5.9	46.2	92.5
300.	.919	.855	.882	5.8	45.4	90.9
400.	.917	.854	.881	5.8	44.4	88.8
500.	.914	.856	.882	5.7	43.2	86.5
600.	.912	.858	.883	5.6	41.9	83.7
700.	.909	.860	.884	5.3	40.1	80.1
800.	.906	.862	.885	5.0	38.1	76.3
900.	.901	.863	.886	4.7	36.1	72.2
1000.	.896	.864	.886	4.3	34.0	68.0
1100.	.890	.864	.885	4.0	31.8	63.6
1200.	.883	.864	.885	3.6	29.5	59.1
1300.	.877	.864	.884	3.2	27.9	55.7
1400.	.871	.864	.884	2.8	26.3	52.7
1500.	.865	.863	.883	2.4	24.6	49.2
1600.	.859	.862	.883	2.0	22.6	45.2
1700.	.853	.862	.882	1.6	20.4	40.8
1800.	.846	.861	.880	1.1	18.0	36.0

Table E.6: *Impact parameter dependent subshell correction factors for the L–subshells [Ja91] and capture probabilities of an L shell target electron by the K shell of the projectile according to the SPB [Ja91].*

E.3 500 MeV Ne^{10+} → U

Impact parameter in *fermi*	Direct ionization probabilities per subshell ($\times 10^{-4}$)								
	K	L_I	L_{II}	L_{III}	M_I	M_{II}	M_{III}	M_{IV}	M_V
100	201.	472	927	1718	944	1052	2295	3418	5057
200	147.	440	910	1710	930	1035	2282	3416	5055
300	97.	413	889	1697	915	1017	2267	3413	5053
400	62.	391	866	1680	901	999	2251	3409	5050
500	39.	375	840	1658	887	981	2232	3405	5046
600	24.	365	809	1631	873	964	2212	3400	5041
700	15.	358	773	1598	860	946	2190	3395	5036
800	9.	355	736	1561	846	928	2165	3388	5030
900	6.	356	697	1521	832	910	2140	3381	5023
1000	4.	360	658	1478	820	892	2112	3374	5016
1100	2.	364	617	1430	807	872	2077	3365	5008
1200	1.	369	576	1380	795	852	2039	3356	4999
1300	0.8	373	538	1327	782	832	2000	3346	4989
1400	0.5	378	502	1273	769	812	1962	3336	4979
1500	0.3	377	466	1218	757	793	1923	3324	4968
1600	0.2	375	432	1162	744	775	1884	3312	4957
1700	0.1	372	398	1106	731	758	1844	3300	4944

Table E.7: *Impact parameter dependent direct ionization probabilities for removing one arbitrary electron from K, L and M shells as calculated by [Am91].*

Impact parameter in *fermi*	Ionization probabilities per subshell ($\times 10^{-4}$)			
	K	L_I	L_{II}	L_{III}
0	224	448	568	915
100	212	409	839	1450
200	150	379	826	1440
300	100	348	806	1430
400	64	321	781	1410
500	41	300	753	1390
600	26	287	722	1370
700	16	280	689	1340
800	10	278	655	1310
900	7	280	621	1270
1000	4	285	586	1240
1100	3	293	550	1200
1200	2	297	518	1160
1300	1	303	480	1110
1400	0.6	306	453	1070
1500	0.4	308	430	1020
1600	0.3	310	394	980
1700	0.2	308	367	936

Table E.8: *Impact parameter dependent direct ionization probabilities for removing one arbitrary electron from K and L shells as calculated using the SCA version of [Tr80].*

Impact parameter in *fermi*	Subshell coupling correction factor			Capture probabilities per subshell ($\times 10^{-4}$)		
	L_I	L_{II}	L_{III}	L_I	L_{II}	L_{III}
100.	.786	.667	.729	7.5	106.67	213.33
200.	.778	.666	.727	7.4	104.60	209.20
300.	.767	.671	.725	7.3	102.00	204.00
400.	.756	.676	.728	7.3	98.67	197.33
500.	.748	.681	.729	7.2	95.00	190.00
600.	.746	.683	.729	7.1	90.67	181.33
700.	.721	.685	.730	6.9	86.00	172.00
800.	.714	.687	.730	6.7	80.33	160.67
900.	.705	.689	.731	6.5	74.33	148.67
1000.	.696	.689	.730	6.3	67.33	134.67
1100.	.689	.689	.729	6.2	60.67	121.33
1200.	.681	.689	.728	6.1	53.33	106.67
1300.	.676	.688	.725	6.2	49.67	99.33
1400.	.670	.687	.722	6.5	44.33	88.67
1500.	.666	.686	.720	6.8	39.33	78.67
1600.	.664	.686	.720	6.9	34.33	68.67
1700.	.658	.686	.719	7.2	29.67	59.33

Table E.9: *Impact parameter dependent subshell correction factors for the L-subshells [Ja91] and capture probabilities of an L shell target electron by the K shell of the projectile according to the SPB [Ja91].*

F. References

Aa78 Aashamar K., Luke T.M. and Talman J.D., 1978 *At. Data Nucl. Data Tables* **15**, 305

Aa81 Aashamar K. and Amundsen P. A. 1981 *J.Phys. B: At. Mol. Phys.* **14**, 483

Aa88 Aashamar K. and Amundsen P. A., 1988 *J.Phys. B: At. Mol. Phys.* **21**, 2709

Ag79 Agarwal B.K. 1979 *X-ray spectroscopy, edited by MacAdam D.L., (Springer-Verlag Berlin,Heildelberg,New York 1979)*

Al56 Alder K., Bohr A., Huus T., Mottelson B., and Winther A. 1956 *Reviews of Modern Physics*, Vol. 28, No. 4, 432

Al66 Alder K. and Winther A. 1966 *Coulomb Excitation Academic Press, New York and London 1966*

Am88 Amundsen P. A., and Jakubassa-Amundsen D.H 1988 *J.Phys. B: At. Mol. Opt. Phys.* 21, L99

Am91 Amundsen P. A. Private communication.

An80 Andersen H.H, 1980, *Bibliography and Index of Experimental Range and Stopping Power Data, Volume 2 of The Stopping and Ranges of Ions in Matter, Edited by Ziegler J. F. Pergamon Press, New York / Toronto / Oxford / Sydney / Frankfurt / Paris*

An82 Anderdsen J.U., Laegsgaard E., and Lund M., 1982, *Nucl. Instrum. and Methods***192**, 79

An91a Anagnostopoulos D.F., Borchert G.L., Gotta D. and Rashid K. 1991 *Z.Phys.D - Atoms, Molecules and Clusters* **18**, 139

An91b Anagnostopoulos D.F., Borchert G.L., Gotta D. and Rashid K., 1991, *Nuclear and Atomic Physics with Accelerators of the Nineties, edited by Sujkowski Z., Proc. 1990 Mikolajki Summer School on Nucl. Phys., (A.Higler 1991)*

Ba59 Bang J. and Hansteen J.M., 1959,*Kgl. Dan. Vid. Selsk. Mat.-Fys. Medd.***31**, no. 13

Ba73 Basbas G., Brandt W., and Laubert R., 1973,*Phys. Rev. A*7, 983

Be67 Bearden J.A., 1967, *Rev. Mod. Phys.***39**, 78

Be80 Betz H.D., 1980,*Methods of Experimental Physics Atomic Physics, Accelerators, Volume 17, edited by Richard P., Academic Press, New York, 1980*

Be84 Becker R.L., Ford A.L., and Reading J.F., 1984,*Nucl. Instrum. and Methods* **B4**, 271

Be87 Beusher H., Böge H.G., Borsch H., 1987,*Jül-Spez-403*,bf 99

Be88 Beusher H., Böge H.G., Bräutigam W., Brings R. 1988, *Jül-Spez-442*, 105

Bo48 Bohr N., 1948, *Kgl. Dan. Vid. Selsk. Mat.-Fys. Medd.***18**, no. 8

Bo86 Borchert G.L., Bojowald J., Ercan A., Labus H., Rose Th., and Schult O.W.B., 1986, *Nucl. Instrum. Methods* **A245**, 393

Br83 Bransden B.H and Joachain C. J., 1983, *Physics of Atoms and Molecules, Longman Group Limited 1983*

Ca81 Carlson T.A and Nestor C.W., 1981, *Phys. Rev. A***8**, 2887

Ca90 Carlen M., Dousse J.-Cl., Gasser M., Kern J., Rheme Ch., Rymuza P., Sujkowski Z. and Trautmann D., 1990,*Europhys. Lett.* **13**, 231

Ch79 Chen M.H., Crasemann B. and Mark H., 1979, *Atomic Data and Nuclear Data Tables* **24**, 13

Ch81 Chen M.H., Crasemann B. ,Aoyagi M., Huang K-N. and Mark H.,1981, *Atomic Data and Nuclear Data Tables***26**, 561

Ch85 Chen M.H., 1985, *Atomic Inner-Shell Physics, edited by Crasemann B., Plenum, New York and London, 1985*

De75 Desclaux J.P. 1975, *Comp. Phys. Commun.***9**, 31

De86 Dexheimer K., Ullrich J., Stiebing K.E.,Schadt W.,Kelbch S., Kelbch C., Schuch R., Zehender S., and Scmidt- Böcking H., 1986, *J.Phys. B: At. Mol. Phys.***19**, 3083

Dr28 Druyvesteyn M.J., 1928, *Z.Phys.***43**, 707

Do90 Dousse J.Cl. 1990, Private communication

Ei81 Eichler J.K.M. 1981, *Phys. Rev. A***23**, 498

Fa65 Fano U. and Lichten W., 1965, *Phys. Rev. Lett***14**, 627

Ga73 Garcia J. D., Fortner R. J., Kavanagh T.M., 1973, *Rev. Mod. Phys.***45**, 111

Gr70 Grant I.P. 1970, *Adv. Phys.* **19**, 747

Gu82 Gundersen R., Hansteen J.M. and Kocbach L. 1982, *Nucl. Instrum. Methods* **192**, 63

Ha72 Hansteen J.M., Mosebek O.P., 1972, *Phys. Rev. Lett.***29**, 1361

Ha75 Hansteen J.M., Johnsen O.M. and Kocbach L. 1975, *At. Data Nucl. Data Tables***15**, 305

In91 Indelicato P., 1991, We thank P.Indelicato for providing us the new version of the Desclaux MCDF code.

Ja74 Jaker C.W., Vries H., and Vries C., 1974, *At. Data Nucl. Data Tables***14**, 486

Ja84 Jakubassa-Amundsen D.H., 1984, *Z. Phys. A***316**, 161

Ja91 Jakubassa-Amundsen D.H., 1991, private communication

Ko75 Kowalczyk S.P., Ley L., Martin R.L., McFeely F.R., and Shirley D.A, 1975,*Faraday Discuss. Chem. Soc.***60**, 7

Kr79a Krause M.O., 1979, *J. Phys. Chem. Ref. Data***8**, 307

Kr79b Krause M.O., Oliver J.H., 1979, *J. Phys. Chem. Ref. Data***8**, 329

La71 Larkins F.P., 1971, *J. Phys. B.***4**, 229

La78 LaVilla R.E., 1978, *Phys. Rev. A.* **17**, 1018

Le78 Lederer C.M.,Shirley V.S,Browne E.,Dairiki J.M., Doebler E., Shihab-Elbin A.A,Jardine L.J.,Tuli J.K and Buyrn A.B, 1978, it Tables of Isotopes, Seventh Edition, (Wiley, New York)

Li67 Lichten W., 1967, *Phys. Rev.***164**, 131

Lo90 Long X., Liu M., and Peng X. 1990, *Atomic Data and Nuclear Data Tables***45**, 353

Ma68 Marion J.B., Young F.C., 1968, *Nuclear Reaction Analysis, Amsterdam, North Holland*

Ma75 Madison D.H and Merzbacher E., 1975, *Atomic Inner Shell Processes, edited by Crasemann B., Academic Press, New York, 1975*

Me58 Merzbacher E. and Lewis H.N.,1958, *Handbuch der Physik vol.34, p.166 edited by Flügge S. (Springer-Verlag, Berlin)*

Mc72 McGuire J.E., 1972, *Phys. Rev. A*.**5**, 1043

Mc73 McGowan F.K., and Milner W.T., 1973, it Charged-Particle Reaction List, 1948-1971, Volume 2, edited by Katharine Way Academic Press, New York and London 1973

Mc77 McGuire J.H. and Weaver L., 1977, *Phys. Rev. A*.**16**, 41

Mo78 Mokler P.H and Folkmann F., 1978, *Structure and Collisions of Ions and Atoms, edited by Sellin I.A., (Springer-Verlag Berlin,Heildelberg,New York 1978)*

Pa88 Review of Particle Properties, 1988, *Physics Letters*B**204**

Pa25 Pauli W., 1925, *Z.Phys.***31**, 778

Pe87 Perny B., Dousse J.-Cl., Gasser M., Kern J., Rheme Ch., Rymuza P., and Sujkowski Z., 1987, *Phys. Rev. A*.**36**, 2120

Po89a Polasik M., 1989, *Phys. Rev. A*.**39**, 616

Po89b Polasik M., 1989, *Phys. Rev. A.* **39**, 5092

Po89c Polasik M., 1989, *Phys. Rev. A.* **40**, 4361

Po90 Polasik M., 1990, *Phys. Rev. A.* **41**, 3689

Sa74 Salem S.I, Panossian S.L. and Krause R.A. 1974, *At. Data Nucl. Data Tables*14, 91

Sa76 Salem S.I, and Lee P.L., 1976, *At. Data Nucl. Data Tables*18, 233

Sa77 Sauli F., 1977, *Principles of Operation of Multiwire proportional and Drift Chambers, CERN 77-09*

Sa89 Salziger R.,Borchert G.L.,Gotta D., Schult O.W.B, Jakubassa- Amundsen D.H., Amundsen P.A., Rashid K., 1989, *J.Phys. B: At. Mol. Phys.* **22**, 821

Sa90 Sarkadi L. and Mukoyama T., 1990, *J.Phys. B: At. Mol. Phys.* **23**, 3849

Sc74 Scofield J.H., 1974, *Atomic Data and Nuclear Data Tables*14, 121

Sc88 Schadt W., Schmidt-Böcking H., Nolte G., Roller Z., Skultlartz A., Wassermann A., and Zschornack G., 1988, *Z. Phys. D*8, 271

Sh81 Shima K., Nakagawa T., Umetani K., and Mikumo T., 1981, *Phys. Rev. A.* **24**, 72

Tr80 Trautmann D. and Rossel F., 1980, *Nucl. Instrum. Methods* **169**, 259

Tr89 Trautmann D. and Baur G., 1989, *Nucl. Instrum. Methods B* **40/41**, 345

Ve73 Veigele Wm. J., 1973, *Atomic Data Tables* **5**, 51-111 (1973)

We25 Wentzel G., 1925, *Z.Phys.* **31**, 445

Zi80 Ziegler J. F., 1980, *Handbook of Stopping Cross-Sections for Energetic ions in all Elements Volume 5 of the Stopping and Ranges of Ions in Matter, Edited by Ziegler J. F. Pergamon Press, New York / Toronto / Oxford / Sydney / Frankfurt / Paris*

Acknowledgments

First of all I wish to thank Prof. Schult for the possibility to work at the Institut für Kernphysik of the Forschungszentrum Jülich and his continuous support during my stay at Jülich.

I am deeply indepted to Prof. Borchert, who has guided my steps into the world of X – rays, for his invaluable support and constant encouragement in carrying out this work.

My sincere thanks to Dr. Gotta with whom I enjoyed a close and pleasant collaboration which provided a constant source of stimulation to me.

I am very grateful to Prof. Rashid for many enlightening discussions and helpful comments, to Dr. P.A.Amundsen, Dr. D.H.Jakubassa – Amundsen for providing their results of the ionization and capture probabilities, to Prof. D.Trautmann for supplying us with his code for the calculation of ionization cross sections, and Prof. P. Indelicato for making available the new version of the Desclaux MCDF code.

The technical assistance of K. – P.Wieder is highly acknowledged.

I thank all the colleagues in IKP in particular J.Jannakos, S.Selbach, M.Elble and last but not least H.Gorke.

Finally, I would like to thank my home university, the university of Ioannina and in particular the members of scientific committee responsible for me, namely Prof. C.Papageorgopoulos, Prof. P.Asimakopoulos, and Prof. I.Vergados for their constant encouragement and support.

FORSCHUNGSZENTRUM JÜLICH GmbH

KFA

Jül-2667
August 1992
ISSN 0366-0885